Springer Theses
Recognizing Outstanding Ph.D. Research

Hidetoshi Sano

Shock-Cloud Interaction in RX J1713.7−3946

Evidence for Cosmic-Ray Acceleration in the Young VHE γ-ray Supernova Remnant

Springer

Springer Theses

Recognizing Outstanding Ph.D. Research

Aims and Scope

The series "Springer Theses" brings together a selection of the very best Ph.D. theses from around the world and across the physical sciences. Nominated and endorsed by two recognized specialists, each published volume has been selected for its scientific excellence and the high impact of its contents for the pertinent field of research. For greater accessibility to non-specialists, the published versions include an extended introduction, as well as a foreword by the student's supervisor explaining the special relevance of the work for the field. As a whole, the series will provide a valuable resource both for newcomers to the research fields described, and for other scientists seeking detailed background information on special questions. Finally, it provides an accredited documentation of the valuable contributions made by today's younger generation of scientists.

Theses are accepted into the series by invited nomination only and must fulfill all of the following criteria

- They must be written in good English.
- The topic should fall within the confines of Chemistry, Physics, Earth Sciences, Engineering and related interdisciplinary fields such as Materials, Nanoscience, Chemical Engineering, Complex Systems and Biophysics.
- The work reported in the thesis must represent a significant scientific advance.
- If the thesis includes previously published material, permission to reproduce this must be gained from the respective copyright holder.
- They must have been examined and passed during the 12 months prior to nomination.
- Each thesis should include a foreword by the supervisor outlining the significance of its content.
- The theses should have a clearly defined structure including an introduction accessible to scientists not expert in that particular field.

More information about this series at http://www.springer.com/series/8790

Hidetoshi Sano

Shock-Cloud Interaction in RX J1713.7−3946

Evidence for Cosmic-Ray Acceleration in the Young VHE γ-ray Supernova Remnant

Doctoral Thesis accepted by
Nagoya University, Nagoya, Japan

Springer

Author
Dr. Hidetoshi Sano
Department of Physics
Nagoya University
Nagoya
Japan

Supervisor
Prof. Yasuo Fukui
Department of Physics
Nagoya University
Nagoya
Japan

ISSN 2190-5053 ISSN 2190-5061 (electronic)
Springer Theses
ISBN 978-4-431-55635-0 ISBN 978-4-431-55636-7 (eBook)
DOI 10.1007/978-4-431-55636-7

Library of Congress Control Number: 2016954605

Printed on acid-free paper

This Springer imprint is published by Springer Nature
The registered company is Springer Japan KK
The registered company address is: Chiyoda First Bldg. East, 3-8-1 Nishi-Kanda, Chiyoda-ku, Tokyo 101-0065, Japan

Supervisor's Foreword

The origin of cosmic rays has been a long-standing issue in astrophysics since their discovery by Victor Hess in 1912. In the following years, cosmic rays have stimulated the development of various fields of physics, in particular, particle physics and astrophysics. The origin of cosmic rays is therefore a subject of broad and keen interest in the physics community. In the early days of cosmic ray research it was suggested that the supernova remnants (SNRs) produced by stellar explosions are the primary source of the cosmic-ray acceleration in the Galaxy, whereas it remains to be firmly established that the SNRs are in fact the site of cosmic-ray acceleration.

In 2009 Dr. Hidetoshi Sano joined in the newly developing research at Nagoya University into the interstellar medium interacting with the SNRs. In the graduate program he developed his skill in studying the interstellar medium based on mm/sub-mm observations, aiming to reveal the physical properties of the interstellar medium interacting with the SNRs. His first paper, published in 2010, was on the comparison between X-rays and the molecular gas in the young TeV gamma-ray SNR RX J1713.7−3946. In the paper he presented evidence for the dense gas clumps interacting with the SNR shocks to produce enhanced non-thermal X-rays, where the molecular cloud was observed with the 4-m mm/sub-mm telescope NANTEN2. This paper was followed by two more papers that presented a detailed and comprehensive comparison between X-rays and interstellar gas, where the X-ray data obtained by the *Suzaku* satellite were analyzed under the co-supervision of Prof. Takaaki Tanaka of Kyoto University and myself. In these papers Dr. Sano discovered the detailed correlation between non-thermal X-ray properties and the dense neutral gas and interpreted the results in terms of the shock-cloud interaction developed by Inoue, Yamazaki, Inutsuka, and Fukui (2012). These three papers by Dr. Sano revealed the physical relationship between non-thermal X-rays and a highly inhomogeneous interstellar medium.

In 2010 Dr. Sano also joined in the research of gamma rays in the SNR under my supervision and played a major role in correlating the CO and HI gas and TeV gamma rays. This study presented the first full correspondence of the interstellar protons with TeV gamma rays, a necessary condition if the gamma rays are

dominated by the hadronic process. This obviously marked an important step in establishing the hadronic process and thereby the SNR origin of cosmic ray protons. It is now well appreciated by the physics community that the highly inhomogeneous interstellar medium plays a vital role in producing high-energy radiation including X-rays and gamma rays.

It is therefore a great pleasure to know Dr. Hidetoshi Sano as a Springer Thesis Prize winner.

Nagoya, Japan
August 2016

Prof. Yasuo Fukui

Parts of this thesis have been published in the following journal articles:

Sano, H., Sato, J., Horachi, H. et al.
The Astrophysical Journal, Volume 724, pp. 59–68, 2010

Sano, H., Tanaka, T., Torii, K. et al.
The Astrophysical Journal, Volume 778, pp. 59–77, 2013

Fukui, Y., Sano, H., Sato, J. et al.
The Astrophysical Journal, Volume 746, pp. 82–99, 2012

Sano, H., Fukuda, T., Yoshiike, S. et al.,
The Astrophysical Journal, Volume 799, pp. 175–174, 2015

Acknowledgements

First of all, I would like to express my deepest gratitude to Prof. Yasuo Fukui, my supervisor, for guiding and leading me throughout the five years at Nagoya University. I am grateful for his great encouragement in various aspects during my research. I have learned a lot of things, especially what is necessary in order to become a good scientist and professor. I am truly a lucky person that I was able to study under his supervision.

I would like to express my thankfulness to Prof. Kengo Tachihara, who gave me enormous help for the research and activities in the laboratory. I am also grateful to Profs. Hiroaki Yamamoto and Takeshi Okuda, who taught me some basic knowledge for operating and contracting of the radio telescope. My grateful thanks are due to Prof. Akiko Kawamura who gave me huge help and long-term support. I also thank Dr. Takahiro Hayakawa, who supported the maintenance and management of many computers for analyzing and helping me in a scientific outreach. I am grateful to Dr. Kazufumi Torii, who taught me how to analyze CO data and significantly contributed to the data analysis. I express gratitude to Dr. Toshihisa Kuwahara, who taught me how to develop the observational device to be installed in NANTEN2. I would like to acknowledge Profs. Hideo Ogawa, Akira Mizuno, Toshikazu Onishi, Norikazu Mizuno, and developers of the NANTEN2 telescope.

I am deeply thankful to Profs. Takaaki Tanaka and Hironori Matsumoto, who taught me how to analyze X-ray data from A to Z and who provided in-depth discussion. My sincere gratitude goes to Profs. Gavin Rowell and Felix Aharonian, who taught me the method for using γ-ray data; their help was invaluable. My heartfelt gratitude goes to Profs. Tsuyoshi Inoue, Shu-ichiro Inutsuka, and Ryo Yamazaki, who provided tremendous support for the observational results with the numerical simulations and extensive discussions. I would like to thank Profs. Jürgen Stutzki, Frank Bertoldi, Leo Bronfman, Bon-Chul Koo, Arnold Benz, and Michael Burtons for their contribution when I submitted my first refereed paper.

I would like to express my gratitude to all the graduate and undergraduate students in our laboratory for their kind help and camaraderie: Natyuta Moribe,

Ryuji Okamoto, Rei Enokiya, Satoshi Yoshiike, Tatsuya Fukuda, Keisuke Hasegawa, Sho Soga, Shigeki Shimizu, Taichi Nakashima, Masashi Wada, Momo Hattori, Yusuke Hattori, Tsukasa Usui, Keiko Yokoyama, Makio Ito, Yuta Takeuchi, and Sayaka Mochizuki.

I acknowledge financial support from the Japan Society for the Promotion of Science.

Finally, I thank all my friends and family, especially my wife, for helping and encouraging me in various aspects throughout my research and life.

Contents

Chapter 1
Introduction

1.1 Background

Cosmic rays are charged and highly energetic particles mainly comprising protons, with $\sim$10 % helium and 1 % electrons and ionized nuclei. Understanding the origin and acceleration mechanism of cosmic rays has been one of the most important challenges in astrophysics over the past century because cosmic rays are one of the primary components in the local interstellar space (see Table 1.1). Cosmic rays affect heating and ionization of the interstellar medium (ISM). However, the sites of galactic cosmic ray acceleration ($E < 3 \times 10^{15}$ eV; the so called *knee*) are still not clear.

Supernova remnants (SNRs) are the most likely candidates for acceleration below the *knee* energy because they are about the only energy sources that can satisfactorily explain the cosmic ray production rate observed in the Galaxy (see Sects. 1.2 and 1.3). The theory of diffusive shock acceleration (DSA, see Sect. 1.3.2 for details) in SNRs can explain efficient particle acceleration and the observed cosmic ray spectrum. Unfortunately, the sites of production/acceleration of cosmic rays cannot be directly observed owing to interstellar magnetic fields, as the gyroradii of cosmic rays are much smaller than the distances between the sources and observers on Earth.

The most important breakthrough in understanding cosmic ray origins was the discovery of non-thermal X-ray radiation from the young SNR SN1006 by the *ASCA* X-ray observatory (Koyama et al. 1995). These observations revealed that synchrotron X-rays are produced by electrons with energies in the tera electron-volt (10^{12} eV; hereafter TeV) domain. Detection of such synchrotron X-rays from other SNRs soon followed (e.g., Koyama et al. 1997; Slane et al. 2001; Tian et al. 2010), and it was confirmed that cosmic ray electrons are accelerated in these SNRs. A further observational breakthrough was the imaging of very high energy (VHE; Energies $E >$ 100 GeV) γ-rays from young SNRs (e.g., Aharonian et al. 2004, 2007) obtained by atmospheric Cherenkov telescopes (H.E.S.S., CANGAROO, MAGIC, etc.). It is suggested that VHE γ-rays are produced by TeV electrons and/or protons through interactions with photon fields (i.e., inverse Compton scattering with cosmic ray

H. Sano, *Shock-Cloud Interaction in RX J1713.7–3946*,
Springer Theses, DOI 10.1007/978-4-431-55636-7_1

Table 1.1 Energy densities in the local interstellar space

Interstellar component	Energy density (eV cm^{-3})	Note
Cosmic Microwave Background (CMB)	0.265	(1)
Far-infrared radiation from dust	0.31	(2)
Starlight ($h\nu < 13.6$ eV)	0.54	(2)
Thermal kinematic energy $(3/2)nkT$	0.49	(3)
Turbulent kinematic energy $(1/2)\rho v^2$	0.22	(4)
Magnetic energy $B^2/8\pi$	0.89	(5)
Cosmic rays	1.39	(6)

Notes. (1): For $T_{\rm CMB} = 2.725\,{\rm K}$ (Fixsen 2009), (2): Chap. 12 in Draine (2011), (3): For $nT = 3800\,{\rm cm}^{-3}$ (also see Draine 2011), (4): For $n_{\rm H} = 30\,{\rm cm}^{-3}$, $v = 1\,{\rm km\,s}^{-1}$, (5): For median $B_{\rm tot} \sim 6\,\mu{\rm G}$ (Heiles and Crutcher 2005), (6): Chap. 13 in Draine (2011)

electrons, referred to hereafter as the leptonic origin scenario, see Sect. 1.4.2) and/or interstellar protons (π^0-decay resulting from cosmic ray proton collisions, referred to hereafter as the hadronic origin scenario, see Sect. 1.4.3). Thanks to synchrotron X-ray and γ-ray observations, we are now able to study the physical properties of cosmic ray acceleration. However, there are still outstanding questions concerning cosmic ray acceleration in SNRs:

Q.1 How are cosmic rays efficiently accelerated in young (age $\sim$ 2000 year) SNRs?
Q.2 Which is the dominant origin process in VHE γ-ray SNRs, hadronic or leptonic?
Q.3 What is the relationship between cosmic ray acceleration and the material surrounding SNRs?

Regarding the first question, observational results show that the power law index of synchrotron X-ray spectra (the so-called "photon index" Γ) differs by region within an SNR (e.g., Cassam-Chenaï et al. 2004; Tanaka et al. 2008; Bamba et al. 2012). In other words, the variation of Γ indicates that the acceleration efficiency of cosmic ray electrons varies, but the reason for this is not precisely known. Regarding the second question, observations have allowed us to observe broad band spectra from X-rays to γ-rays, enabling comparative study between observational results and theoretical models. Although these studies have presented successful results and have improved our understanding of cosmic ray properties, it is very difficult to distinguish the hadronic and leptonic γ-rays from the spectrum study alone in most cases. Furthermore, if the SNR is interacting with inhomogeneous ISM gas, its hadronic γ-ray emissions will be indistinguishable from leptonic emissions (Inoue et al. 2012). Although the actual ISM environment is not uniform, most theoretical models assume uniformity. Therefore, the sources of cosmic ray protons have still not been firmly identified.

Regarding the third question, some γ-ray SNRs are associated with dense ISM gas (see Sect. 1.5). SNR shock waves ($\sim$3,000–10,000 $\rm km\,s^{-1}$) must affect the ISM gas through physical interaction, but the detailed mechanisms of this are not well understood. According to the diffusive shock acceleration (DSA) model, such shock

waves also produce cosmic ray particles; therefore, clarifying the shock wave–ISM interaction mechanisms will provide a better understanding of the cosmic ray acceleration mechanism.

In this thesis, I show the observational answers to questions Q.1, Q.2, and Q.3. This chapter I review galactic cosmic rays and their acceleration mechanisms. Additionally, I summarize previous studies of the interactions between SNRs and the ISM. In particular, I focus on the young and VHE γ-ray-bright SNR RX J1713.7−3946. Chapter 2 presents a relationship between non-thermal X-ray radiation and the ISM (Q.1 and Q.3). Chapter 3 shows evidence for the acceleration of cosmic ray protons in SNR RX J1713.7−3946 (Q.2). Chapter 4 describes the mechanism of efficient cosmic ray acceleration. In Chap. 4, I summarize our results and outline future research prospects.

1.2 Cosmic Rays

Ever since the first detection of cosmic rays in 1912 by Victor F. Hess, who discovered that the ionization rate of the atmosphere increased as he ascended in a balloon, the mechanism for how cosmic rays are accelerated in the universe has been in question. The radiation discovered by Hess, first called "Hohenstrahlung" and then "cosmic rays," represented the first detection of ionizing radiation from extraterrestrial sources. By the 1930s, this radiation was believed to be high energy γ-rays and/or positively charged particles. As described above, we now know that cosmic rays are charged particles mainly comprising protons with ∼10 % helium and 1 % electrons and ionized nuclei. The energy spectra of cosmic rays are now known to extend beyond 10^{20} eV and are described with a power-law function as

$$dN(E) \propto E^{-p} dE \tag{1.1}$$

where N is the number of particles with kinetic energy E. The spectral index p lies in the range of about 2.2–3.0. Figure 1.1 shows the energy spectrum of cosmic rays surrounding the earth (Beatty and Westerhoff 2009). Two turn-overs can be clearly seen in the energy spectra: one at $E \sim 3 \times 10^{15}$ eV (the so-called *knee*) and the other at $E \sim 3 \times 10^{18}$ eV (the so-called *ankle*). The spectral index is ∼2.7 in the energy range between 10^{10} and the *knee* and becomes ∼3 in the energy range between the *knee* and *ankle*. The spectral index above the *knee* has not yet been determined. In this thesis, galactic cosmic rays are defined as high energy particles below the *knee* energy and their origin is assumed to be from Galactic sources. The gyroradius $r_{\rm gyro}$ of a relativistic particle is given by

$$r_{\rm gyro} \sim \frac{1}{Z} \left(\frac{E}{10^{15}\ {\rm eV}} \right) \left(\frac{B}{1\ \mu{\rm G}} \right)^{-1} {\rm pc}, \tag{1.2}$$

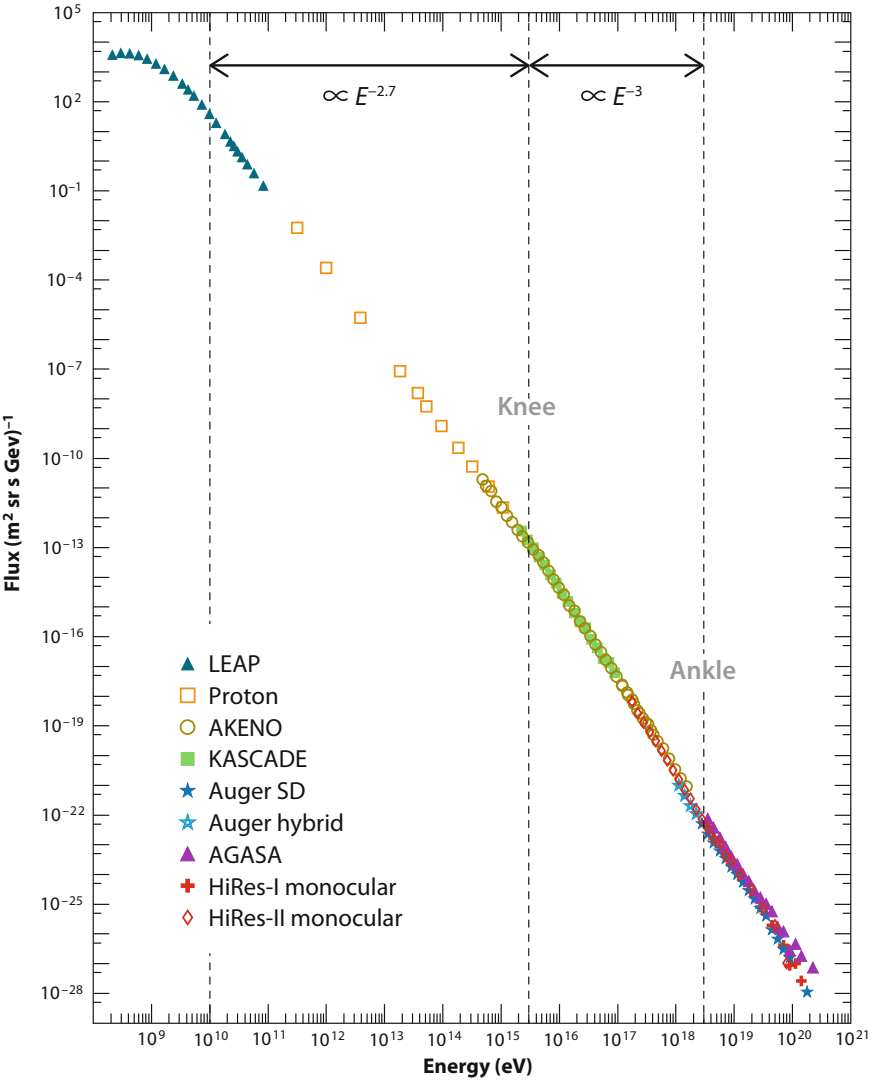

Fig. 1.1 The energy spectrum of cosmic rays (Beatty and Westerhoff 2009)

where Z is the nuclear atomic number, E is kinetic energy, and B is the magnetic field strength. If we adopt $E = 10^{15}$ eV, $Z = 1$, and $B = 3\,\mu$G (typical values for the interstellar magnetic field), a cosmic ray proton has $r_{\rm gyro} \sim 0.3$ pc. Therefore, the interstellar magnetic field can confine cosmic rays ($E < 3 \times 10^{15}$ eV) within the Galaxy, whose radius and scale height are roughly 15 kpc and 300 pc, respectively. Particles at energies around the *ankle* are generally thought to be accelerated in extra-galactic sources (e.g., active galactic nuclei, gamma-ray bursts, and radio galaxies;

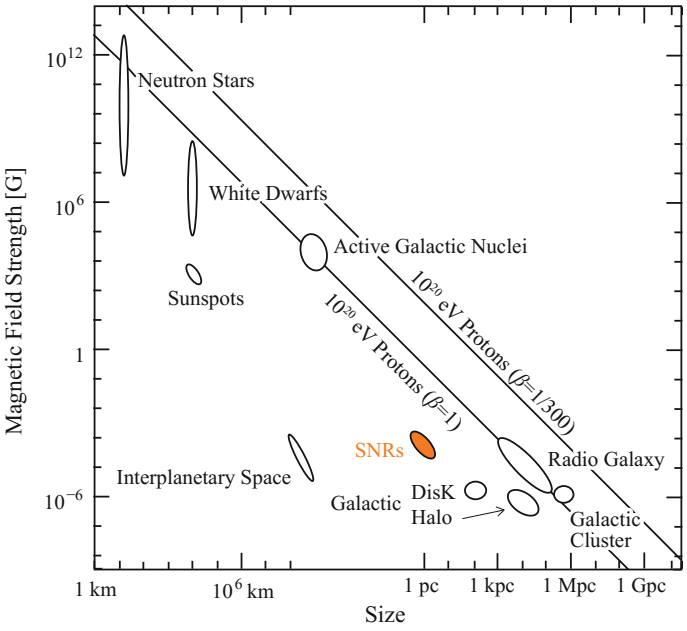

Fig. 1.2 Hillas diagram (Hillas 1984)

see Fig. 1.2). Incidentally, a cosmic ray proton with an energy of around 10^{20} eV can interact with the cosmic microwave background (CMB) and lose energy from the resulting pion production; as a result, no particles are expected to be observed above $\sim 10^{20}$ eV. This effect is the so-called Greisen Zatsepin Kuzmin (GZK) cut-off.

1.3 Cosmic Ray Acceleration in Supernova Remnants

1.3.1 Kinetic Energy Budget

SNRs are the most promising sources of galactic cosmic ray acceleration (e.g., Ginzburg and Syrovatskii 1964) because the collision-less shock waves they produce are very powerful as galactic sources satisfying the kinetic energies needed to explain the injection rate of cosmic rays. The required injection rate of cosmic rays ($L_{\rm CR}$) is estimated to be

$$L_{\rm CR} = \frac{V\,\varepsilon_{\rm CR}}{\tau_{\rm esc}} \sim 10^{41}\ {\rm erg\ s^{-1}}, \tag{1.3}$$

where $V = \pi R^2 h \sim 4 \times 10^{66}\,{\rm cm^{-3}}$ is the volume of the Galactic disk, which has a radius R of $\sim$15 kpc and thickness h of $\sim$200 pc, $\varepsilon_{\rm CR} = 1.39\,{\rm eV\,cm^{-3}}$

$= 2.2 \times 10^{-12}\,\mathrm{erg\,cm^{-3}}$ is the energy density of cosmic rays (see Table 1.1), and $\tau_{\mathrm{esc}} \sim 3 \times 10^6$ year is the escape time scale (e.g., Gabici 2013). The total power of supernova explosions, P_{SNR}, is given by

$$P_{\mathrm{SNR}} = \frac{E_{\mathrm{SN}}}{f_{\mathrm{SN}}} \sim 10^{42}\ \mathrm{erg\ s^{-1}}, \tag{1.4}$$

where $E_{\mathrm{SN}} = 10^{51}$ erg is the typical supernova explosion energy and $f_{\mathrm{SN}} \sim 30$ year is the supernova rate in the Galaxy (∼3 events / century). Therefore, if galactic cosmic rays are accelerated in SNRs, ∼10 % of each supernova's energy is transferred to cosmic rays.

1.3.2 *Diffusive Shock Acceleration*

As described above, galactic cosmic rays are accelerated by shock waves in SNRs wherein collisionless shock waves are caused by supersonic plasma flows. Here, we define an upstream fluid flowing toward the shock front with velocity v_1, density ρ_1, pressure P_1, and temperature T_1, and a downstream fluid beyond the shock front with velocity v_2, density ρ_2, pressure P_2, and temperature T_2 (see Fig. 1.3). These fluids satisfy the following conditions (the so-called Rankine–Hugnoiot equation):

$$\rho_1 v_1 = \rho_2 v_2 \tag{1.5}$$

$$P_1 + \rho_1 v_1^2 = P_2 + \rho_2 v_2^2 \tag{1.6}$$

$$\rho_1 v_1 \left(\frac{v_1^2}{2} + \frac{P_1}{\rho_1} + u_1 \right) = \rho_2 v_2 \left(\frac{v_2^2}{2} + \frac{P_2}{\rho_2} + u_2 \right), \tag{1.7}$$

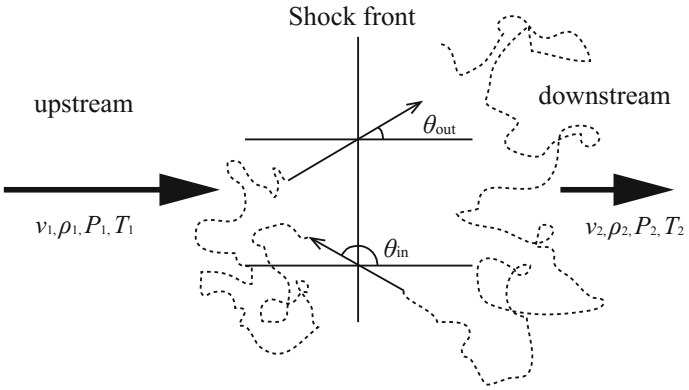

Fig. 1.3 Schematic view of the diffusive shock acceleration. The *dashed lines* indicate the locus of cosmic rays

where u_1 and u_2 are the internal energies of the upstream and downstream fluids, respectively. Here, c_s is the velocity of sound, $c_s = \sqrt{\gamma P/\rho}$, where γ is the ratio of the heat capacity at constant pressure C_P to that at constant volume C_V. Then, writing $P + \rho v^2 = P(1 + \gamma M^2)$ with the Mach number $M = v/c_s$, the downstream/upstream ratios of density, pressure, and temperature are written as

$$\frac{\rho_2}{\rho_1} \left(= \frac{v_1}{v_2}\right) = \frac{(\gamma+1)M_1^2}{(\gamma-1)M_1^2+2} \equiv r \tag{1.8}$$

$$\frac{P_2}{P_1} = \frac{2\gamma M_1^2 - (\gamma-1)}{\gamma+1} \tag{1.9}$$

$$\frac{T_2}{T_1} = \frac{[2\gamma M_1^2 - (\gamma-1)][(\gamma-1)\gamma M_1^2 + 2]}{(\gamma+1)^2 M^2}. \tag{1.10}$$

where r is the so-called compression ratio. For the strong shock $M \gg 1$, r is given as

$$r = \frac{\gamma+1}{\gamma-1}. \tag{1.11}$$

For a monoatomic gas, $\gamma = 5/3$ and we obtain a constant value of $r = 4$, whereas the density increases to $\rho_2 = 4\rho_1$ and the velocity decreases to $v_2 = v_1/4$ after the passage of the shock front. We next consider the case of cosmic rays traveling through a shock wave from downstream to upstream at an angle $\theta_{\rm in}$ and from upstream to downstream at an angle $\theta_{\rm out}$ to the normal direction of the shock front (i.e., one round trip). The energy gain per one round trip ΔE is given by

$$\Delta E = \frac{v_1 - v_2}{c} (\cos\theta_{\rm in} - \cos\theta_{\rm out}) E. \tag{1.12}$$

where c is the speed of light and $\theta_{\rm in}$ and $\theta_{\rm out}$ are constrained as $\pi/2 < \theta_{\rm in} < \pi$ and $0 < \theta_{\rm out} < \pi/2$, respectively. Since the cosmic rays are considered to have homogeneous distribution at a given angle, we can estimate the average $\cos\theta_{\rm in}$ and $\cos\theta_{\rm out}$ for cosmic rays crossing the shock front:

$$\langle \cos\theta_{\rm in} \rangle = \frac{\int_{\pi/2}^{\pi} \cos^2\theta_{\rm in} \sin\theta_{\rm in} d\theta}{\int_{\pi/2}^{\pi} \cos\theta_{\rm in} \sin\theta_{\rm in} d\theta} = -\frac{2}{3} \tag{1.13}$$

$$\langle \cos\theta_{\rm out} \rangle = \frac{\int_{0}^{\pi/2} \cos^2\theta_{\rm out} \sin\theta_{\rm out} d\theta}{\int_{0}^{\pi/2} \cos\theta_{\rm out} \sin\theta_{\rm out} d\theta} = \frac{2}{3}. \tag{1.14}$$

The averaged energy gain on a round trip is then calculated to be

$$\langle \Delta E \rangle = \frac{4(v_1 - v_2)}{3c} E. \tag{1.15}$$

This equation indicates that the cosmic ray particles gain energy through a round trip over a shock front. After n round trips, the averaged energy gain E_n is given by

$$E_n = E_0\left(1 + \frac{4(v_1 - v_2)}{3c}\right)^n \sim E_0 \exp\left(\frac{4(v_1 - v_2)}{3c}n\right). \tag{1.16}$$

where E_0 is the initial energy. Thus, the kinetic energy continues to increase as long as the cosmic ray particles stay in the vicinity of the shock front. However, a particle will escape from the shock front with a certain probability per round trip. We determine the escape probability $P_{\rm escape}$ as follows. In the downstream fluid, the averaged velocity crossing the shock front is $c/4$ if we assume $v_1 \sim c$. The total flux of particles crossing the shock is then $N_p c/4$, where N_p is the number density of particles and the number of cosmic rays escaping owing to the convective motion is Nv_2. Hence, the probability of particle escape is derived as $Nv_2/(Nc/4) = 4v_2/c$ over a round trip. Therefore, the escape probability $P_{\rm escape}$ from the shock waves after n round trips is

$$P_{\rm escape} = \frac{4v_2}{c} \times \left(1 - \frac{4v_2}{c}\right)^n \sim \frac{4v_2}{c} \exp\left(-\frac{4v_2}{c}n\right). \tag{1.17}$$

Using Eqs. 1.16 and 1.17, the energy spectrum of accelerated particles dN/dE is given by

$$\frac{dN}{dE} \propto E^{-\frac{3v_2}{v_1 - v_2} - 1} = E^{-\alpha}, \tag{1.18}$$

where the spectral index $\alpha = (r + 2)/(r - 1)$. In the case of extreme high speed shock waves, $r = 4$ and the spectral index $\alpha = 2.0$ are given. The value of spectral index agree very well with the cosmic ray spectrum around the earth.[1] The next important question is "what is the maximum energy necessary to accelerate via DSA"? To estimate this, we must evaluate the acceleration time scale $t_{\rm acc}$. This can be described as

$$t_{\rm acc} = \Delta t \left\langle \frac{E}{\Delta E} \right\rangle = \frac{3c}{4(v_1 - v_2)} \Delta t. \tag{1.19}$$

[1]The observed spectral index is 2.7, which is larger than $\alpha = 2.0$. However, this can be attributed to the fact that cosmic rays with higher energy escape the Galaxy more rapidly.

where Δt is the time needed for a round trip. The round-trip time Δt can be decomposed into the upstream and downstream transit times:

$$\Delta t = \frac{4D_1}{v_1 c} + \frac{4D_2}{v_2 c}, \tag{1.20}$$

where D_1 and D_2 are the diffusion coefficients in the upstream and downstream sections, respectively. For simplification, we assume $D_1 = D_2 = D$ and a strong shock ($v_1 = 4v_2 = v_s$). In this case, the diffusion coefficient D is expressed as

$$D = \frac{c\, r_{\rm gyro}}{3}\, \eta, \tag{1.21}$$

where $r_{\rm gyro} = E/(Z_e B)$ (Z_e indicates the charge of the accelerated particle) is the gyroradius and $\eta\ (\geq 1) = (B/\delta B)^2$ is the degree of magnetic field fractionation, or the so-called "gyrofactor".[2] Therefore, Eq. 1.21 can be rewritten as follows:

$$t_{\rm acc} = \frac{20}{3}\, \frac{c}{v_s^2}\, \frac{E}{Z_e\, B}\, \eta. \tag{1.22}$$

Here, we estimate the maximum energy of cosmic rays in an SNR from shock wave characteristics. Since the age of an SNR can be approximated as $t_{\rm age} = R/v_s$ (where R is the radius of the SNR), the maximum energy $E_{\rm max}$ is given by

$$\begin{aligned} E_{\rm max} &= \frac{E}{t_{\rm acc}}\, t_{\rm age} \\ &= \frac{3}{20}\, \frac{v_s}{c}\, \frac{Z_e\, B\, R}{\eta} \\ &\sim 100 \times \eta^{-1}\, Z_e \left(\frac{v_s}{5000\ {\rm km\ s^{-1}}}\right) \left(\frac{B}{10\ \mu{\rm G}}\right) \left(\frac{R}{10\ {\rm pc}}\right) {\rm TeV}. \end{aligned} \tag{1.23}$$

Therefore, cosmic rays can be accelerated up to ~100 TeV in a typical young SNR.

1.4 Radiative Processes of High Energy Cosmic Rays

Accelerated cosmic rays can be observed by their non-thermal emissions, which are produced by the many physical processes causing cosmic ray energy loss. In this section, we introduce the cosmic ray radiative (energy loss) process.

[2] The condition $\eta = 1$ corresponds to the "Bohm diffusion limit," which indicates the most efficient accelerating state.

1.4.1 Synchrotron Radiation

Relativistic charged electrons emit synchrotron radiation through helical motion in a magnetic field. The total power per unit frequency emitted by a single electron is described as follows (e.g., Rybicki and Lightman 1979):

$$P(\omega) = \frac{\sqrt{3}}{2\pi} \frac{q_e^3 B \sin\alpha}{m_e c^2} F\left(\frac{\omega}{\omega_c}\right), \tag{1.24}$$

where B is the field strength; q_e and m_e are the charge and mass of an electron, respectively; and α is the pitch angle between the electron and the magnetic field. The characteristic synchrotron photon energy ε_c is given by

$$\varepsilon_c = \frac{3}{2} \frac{\gamma^2 q_e B \sin\alpha}{mc}. \tag{1.25}$$

The function $F(\omega/\omega_c)$ is also defined as

$$F\left(\frac{\omega}{\omega_c}\right) = \frac{\omega}{\omega_c} \int_{\omega/\omega_c}^{\infty} K_{5/3}(\xi) d\xi, \tag{1.26}$$

where $K_{5/3}$ is the modified Bessel function. The asymptotic forms for the small and large values of ω/ω_c are

$$F\left(\frac{\omega}{\omega_c}\right) \sim \begin{cases} \frac{4\pi}{\sqrt{3}\,\Gamma(1/3)} \left(\frac{\omega/\omega_c}{2}\right)^{1/3}, & (x \ll 1) \\ \left(\frac{\pi}{2}\right)^{1/2} e^{-\omega/\omega_c} \left(\frac{\omega}{\omega_c}\right)^{1/2}, & (x \gg 1) \end{cases} \tag{1.27}$$

Integrating Eq. 1.24 over the frequency range, we obtain the total emitted power $P_{\rm synch}$ as

$$P_{\rm synch} = \frac{4}{3} \sigma_{\rm T} c \beta^2 \gamma^2 U_{\rm B}, \tag{1.28}$$

where $\sigma_{\rm T}$ ($=8\pi r_0^2/3$) is the Thomson cross section and $U_{\rm B}$ ($=B^2/8\pi$) is the magnetic energy density. The value $P_{\rm synch}$ is also called the "energy loss rate" $(dE/dt)_{\rm synch} = -P_{\rm synch}$. We have hitherto described only cases of a single cosmic ray electron. In reality, the synchrotron spectrum comprises radiation from many cosmic ray electrons. The number density of electrons with energies from E to $E + dE$ can be approximately expressed as

$$N(E)dE = CE^{-p}dE, \tag{1.29}$$

where C is a parameter depending on pitch angle. To obtain the synchrotron spectrum, we sum up electrons with different energies, and the total power per unit volume per unit frequency $P_{\rm tot}$ is derived as Abramowitz and Stegun (1965).

$$P(\omega)_{\rm tot} = \int P(\omega)N(E)dE \tag{1.30}$$

$$= \frac{\sqrt{3}\, q_e^3 C B \sin\alpha}{2\pi m_e c^2 (p+1)} \Gamma\left(\frac{p}{4}+\frac{19}{12}\right)\Gamma\left(\frac{p}{4}-\frac{1}{12}\right)\left(\frac{m_e c\omega}{3q_e B\sin\alpha}\right)^{-(p-1)/2}. \tag{1.31}$$

where Γ is the Gamma function. As the parameters in this equation are constant except for B and ω, we have

$$P(\omega)_{\rm tot} \propto A B^{(p+1)/2}\, \omega^{-(p-1)/2}, \tag{1.32}$$

where A is a constant. Therefore, the spectral index s is related to the accelerated electron distribution index p by

$$s = \frac{p-1}{2}. \tag{1.33}$$

We then obtain the photon index Γ of the power-law spectrum of the synchrotron X-rays, defined as $P(\omega)_{\rm tot} = \omega I(\omega)_{\rm tot} \propto \omega^{-\Gamma}$:

$$\Gamma = \frac{p+1}{2} \tag{1.34}$$

Finally, we note the energies of synchrotron X-ray photons ε in young SNRs: (Zirakashvili and Aharonian 2007):

$$\varepsilon = \frac{2.2\ {\rm keV}}{\eta(1+\kappa^{1/2})^2}\left(\frac{v_1}{3000\ {\rm km\ s^{-1}}}\right)^2 \frac{16}{\gamma_s^2}, \tag{1.35}$$

where κ is the ratio of the upstream and downstream magnetic fields and $\gamma_s = 3r/(r-1)$ is the power-law index of particles accelerated in the absence of energy loss with a compression ratio r. In the regime of Bohm diffusion, we can substitute $\kappa = 1$ and $\gamma_s = 4$ (see Sect. 1.3.2) in Eq. 1.36:

$$\varepsilon = 0.55 \times \eta^{-1}\left(\frac{v_1}{3000\ {\rm km\ s^{-1}}}\right)^2 ({\rm keV}). \tag{1.36}$$

This equation indicates that the photon energy of synchrotron X-rays can be determined using only the shock speed v_1 and gyrofactor η.

1.4.2 Inverse Compton Scattering

Relativistic cosmic ray electrons also contribute to the origin of γ-rays through the scattering up to higher energies of low-energy photons (e.g., the CMB). The radiation mechanism is called "inverse Compton scattering," and the energy of a scattered interstellar photon $\varepsilon' = h\nu'$ is described as

$$\varepsilon' = \frac{4}{3}\gamma^2\varepsilon_0, \tag{1.37}$$

where γ is the Lorentz factor and $\varepsilon_0 = h\nu$ is the initial energy of the interstellar photon. For instance, for an electron of 10 TeV ($\gamma = 2 \times 10^7$) scattering a CMB photon ($\varepsilon_0 = 2.725\,\mathrm{K} = 2.348 \times 10^{-4}\,\mathrm{eV}$; see Table 1.1), the scattered photon energy is calculated as 250 GeV. This photon energy corresponds to the energy band of γ-rays; therefore, the γ-ray emitting process is so-called a "leptonic process," as distinguished from π^0-decay ("hadronic process") γ-rays (see Sect. 1.4.3). The total power emitted by a single electron via inverse Compton scattering is described as (e.g., Rybicki and Lightman 1979):

$$P_{\mathrm{IC}} = \frac{4}{3}\sigma_{\mathrm{T}} c \beta^2 \gamma^2 U_{\mathrm{photon}}, \tag{1.38}$$

where $U_{\mathrm{photon}} (= n_{\mathrm{photon}}\varepsilon_0)$ is the energy density of the seed photons. We note that the Thomson scattering is only valid in cases where $\gamma\varepsilon_0 \gg mc^2$. Using Eq. 1.28, we obtain the relationship

$$\frac{P_{\mathrm{synch}}}{P_{\mathrm{IC}}} = \frac{U_{\mathrm{B}}}{U_{\mathrm{photon}}}. \tag{1.39}$$

The ratio of the radiative losses caused by synchrotron emission to those of inverse Compton scattering is the same as that of the magnetic field energy density to the photon energy density. Therefore, in the case of leptonic origin γ-rays alone, we can determine the strength of the magnetic fields directly by comparing P_{synch} with P_{IC}.

1.4.3 π^0-Decay Emission

Accelerated cosmic ray protons also emit γ-rays via a π^0-decay process:

$$p(\mathrm{CR}) + p(\mathrm{ISM}) \rightarrow p + p + \pi^0, \tag{1.40}$$

$$\pi^0 \rightarrow 2\gamma, \tag{1.41}$$

where p(CR) and p(ISM) are accelerated cosmic ray proton and interstellar proton, respectively. We note here that the kinematic energy of a cosmic ray proton $E_{\mathrm{kin}} =$

$E_{\rm p} - m_{\rm p}c^2$ should exceed ~280 MeV. The resulting π^0 decays with a mean lifetime of $\sim 8.4 \times 10^{-17}$ s into two photons. Each of these photons has an energy of 67.5 MeV (half the energy of the π^0) in a static system and are emitted in opposite directions. Since the energies of such photons are enhanced because the π^0 obtains part of the kinematic energy of a cosmic ray proton, this so-called "hadronic process" is an important source of γ-ray production in the universe. The theory of hadronic production was first proposed by Hayakawa (1952) and is widely accepted among researchers worldwide. The γ-ray emissivity $q_\gamma(E_\gamma)$ with energy E_γ for an arbitrary proton spectrum is given by Aharonian and Atoyan (1996):

$$q_\gamma(E_\gamma) = 2 \int_{E_{\rm min}}^{\infty} \frac{q_\pi(E_\pi)}{\sqrt{E_\pi^2 - {m_\pi}^2 c^4}} dE_\pi. \tag{1.42}$$

where E_π and m_π are the kinematic energy and mass of the π^0, respectively, $E_{\rm min}$ is the minimum energy of 2γ production from π^0 mesons, and $q_\pi(E_\pi)$ is the π^0 spectrum as given below:

$$q_\pi(E_\pi) = \frac{cn_{\rm H}}{f_\pi} \sigma_{\rm pp}\left(m_{\rm p}c^2 + \frac{E_\pi}{f_\pi}\right) E_{\rm p}\left(m_{\rm p}c^2 + \frac{E_\pi}{f_\pi}\right), \tag{1.43}$$

where $n_{\rm H}$ is the ambient interstellar gas density, f_π is the mean fraction of the kinetic energy of a proton transferred to the secondary meson per collision, and $E_{\rm p}$ is the energy distribution of the protons. Here, $\sigma_{\rm pp}(E_{\rm p})$ is the interaction cross section between cosmic ray protons with $E_{\rm kin} \geq 1$ GeV and can be approximated as

$$\sigma_{\rm pp}(E_{\rm p}) \sim 30[0.95 + 0.06 \ln(E_{\rm kin})/1 \text{ GeV}] \text{ mb}. \tag{1.44}$$

Here, we use typical values $\sigma_{\rm pp}(E_{\rm p}) \sim 40$ mb and $f_\pi \sim 0.45$ (e.g., Gabici 2013). The cooling time scale of protons via the hadronic process $t_{\rm pp}$ can then be described as

$$t_{\rm pp} = (n_{\rm H}\sigma_{\rm pp} f_\pi c)^{-1} \sim 6 \times 10^7 \left(\frac{n_{\rm H}}{1 \text{ cm}^{-3}}\right) \text{ year}. \tag{1.45}$$

Therefore, the initial spectrum of the accelerated cosmic ray protons is expected to remain unchanged. Next, let us consider the differences between the energy spectra of cosmic ray protons and those of observed γ-rays. The energy of γ-rays produced by the hadronic process E_γ is proportional to the cosmic ray proton energy $E_{\rm p}$ as $E_\gamma = h\nu \sim 0.1 E_{\rm p}$. To calculate the total energy of γ-rays F_ν, we assume the following energy distribution of cosmic ray protons:

$$N_{\rm p}(E_{\rm p}) dE_{\rm p} = C E_{\rm p}^{-p} dE_{\rm p}, \tag{1.46}$$

where C is a constant. The total energy of γ-rays F_ν is given by

$$F_\nu d\nu = \int (0.1E_\mathrm{p}) C E_\mathrm{p}^{-p} dE_\mathrm{p} \tag{1.47}$$

$$= Ch \int (10h\nu)^{1-p} d\nu \tag{1.48}$$

$$F_\nu \propto \nu^{1-p}. \tag{1.49}$$

Then, the photon index Γ is given by

$$\Gamma = p. \tag{1.50}$$

Therefore, the observed γ-ray spectrum produced by the hadronic process almost reproduces the parent proton spectrum, although at energies scaled down by a factor of $\sim$0.1. Consequently, observing hadronic γ-ray emission allows for the direct measurement of cosmic ray properties. Finally, we introduce the relationship between F_ν and the interstellar gas density n_H. Given a total energy of accelerated protons W_p, we obtain

$$F_\nu = \frac{1}{4\pi d^2} \left(\frac{W_\mathrm{p}}{t_\mathrm{pp}} \right),$$

$$F_\nu \propto \left(\frac{W_\mathrm{p}\, n_\mathrm{H}}{d^2} \right), \tag{1.51}$$

where d is the distance to the source. Thus, the γ-ray flux is proportional to the interstellar gas density. This fact strongly suggests that the spatial distribution of hadronic γ-rays is correlated with the interstellar gas distribution.

1.5 Association Between SNRs and the Interstellar Gas

SNRs have a profound influence on the surrounding ISM via shock interaction, which in turn affects SNR evolution. It is therefore important to study the detailed physical properties of the interaction between SNRs and the ISM to understand the physics of shock interaction. In this section, we summarize previous studies on the SNR–ISM interaction.

1.5.1 Overview of Previous Studies

The physical interaction between SNR shocks and the surrounding interstellar gas has been studied for several decades. Previous studies mainly discussed shock

compression (and acceleration) of the interstellar gas (e.g., Seta et al. 1998) and low-mass star formation trigged by SNR shock waves (e.g., Fukui et al. 1999). The physical conditions of shocked gas have already been revealed in some middle-aged SNRs aged several 10,000 year (e.g., Denoyer 1979; Wootten 1977, 1981).

Recently, studies comparing high energy emission and the interstellar gas have again begun to attract attention from the perspective of efficient cosmic ray acceleration in conjunction with γ-ray origination. Figure 1.4 shows the spectrum of the middle-aged SNR W28, which is emitted in the radio continuum and via thermal X-rays and γ-rays (e.g., Brogan et al. 2006; Rho and Borkowski 2002; Aharonian et al. 2008; Abdo et al. 2010). In particular, it has been actively debated whether the VHE γ-rays are of hadronic origin. Distinguishing hadronic and leptonic γ-rays

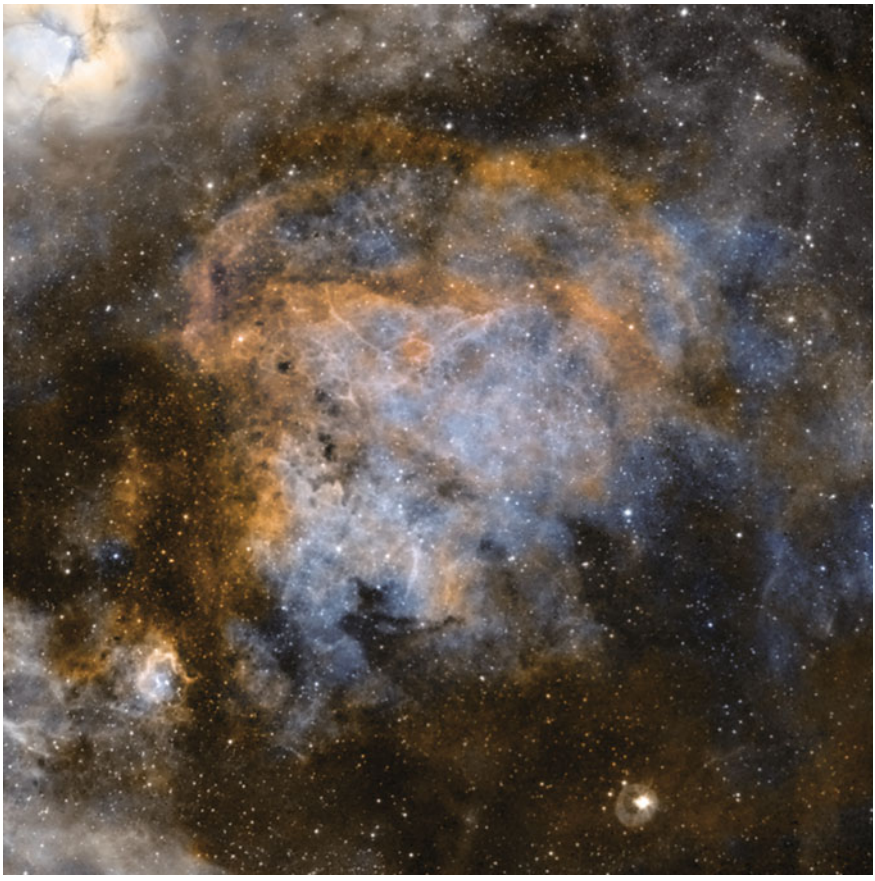

Fig. 1.4 Three color composite image of the middle-aged SNR W28: *orange* is the radio continuum obtained by the very large array (Dubner et al. 2000), *gray* is the optical light captured by the cerro tololo Inter-American observatory (Keohane et al. 2005), and *blue* represents X-rays imaged by *ROSAT* (Rho and Borkowski 2002)

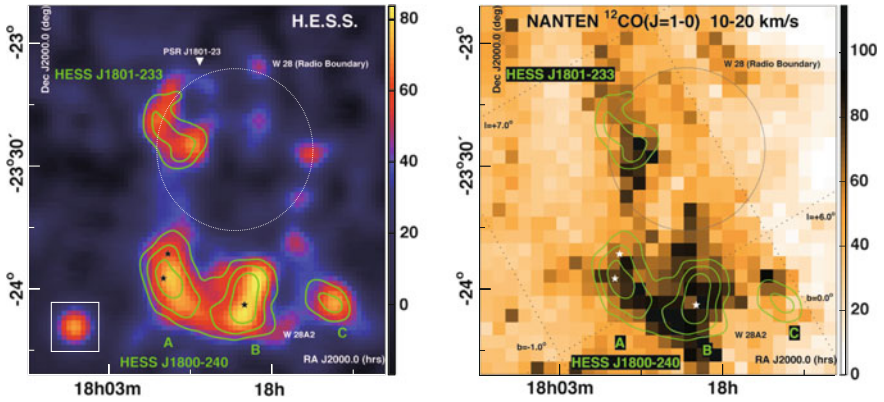

Fig. 1.5 Distributions of H.E.S.S. VHE γ-rays (*left panel*) and NANTEN ^{12}CO($J = 1$–0) emission (*right panel*) toward W28 (Aharonian et al. 2008). The *green* contours show VHE γ-ray significance levels of 4, 5, and 6 σ. The *dashed circles* indicate a boundary of the radio continuum (Brogan et al. 2006). We can easily confirm clear correlation between the VHE γ-rays and the interstellar gas

from only spectral studies using the DSA model is generally difficult owing to the presence of many free parameters (e.g., magnetic field strength) and some unrealistic approximations (e.g., assumption of homogeneous gas density). However, if the γ-rays are of hadronic origin, the spatial distribution of γ-ray flux will be proportional to the CO maps because the CO integrated intensity can be converted to a molecular hydrogen density (see also Eq. 1.51). SNR W28 is also known to have shock waves and escaped cosmic-ray protons that are interacting with the dense molecular gas (e.g., Arikawa et al. 1999); hence, Aharonian et al. (2008) was able to compare the H.E.S.S. γ-ray and NANTEN CO datasets. Figure 1.5 shows the intensity maps of VHE γ-rays and CO. The distribution of VHE γ-rays extends to the exterior of the radio boundary and has four outstanding peaks. We can see a clear correlation between the two images and can conclude that the VHE γ-rays are consistent with hadronic origin. Subsequently, *AGILE* and *Fermi* detected GeV γ-rays, allowing an estimation of the total proton energy, $W_{\rm p} = 2.3$–3.3×10^{49} erg (Giuliani et al. 2010; Abdo et al. 2010). The acceleration rate, $W_{\rm p}/E_{\rm SN} \sim$2–3 %, is less than that estimated in Sect. 1.3.1 ($\sim 10\,\%$) and is quite reasonable. Most recently, Yoshiike et al. (2013, 2016) made similar comparisons for the middle-aged SNRs W44, IC443, and W51C and obtained similar results to those obtained for W28 ($W_{\rm p}/E_{\rm SN} \sim 1\,\%$). These results indicate that middle-aged SNRs emitting γ-rays are one of the main components of cosmic ray proton acceleration. Unfortunately, this is not enough to explain the cosmic ray spectrum below the *knee* energy because middle-aged SNRs cannot accelerate cosmic ray protons to $E_{\rm p} \sim 10^{15}$ eV. Figure 1.6 shows the energy spectrum of the middle-aged SNRs W51C and W44 and the young SNRs RX J1713.7−3946 and Cas A. In middle-aged SNRs, the maximum energy of the expected γ-ray spectrum is $\sim 10^{11}$–10^{12} eV. On the other hand, the maximum energy for young SNRs reaches $\sim 10^{13}$–10^{14} eV. The energy of cosmic ray protons $E_{\rm p}$ is

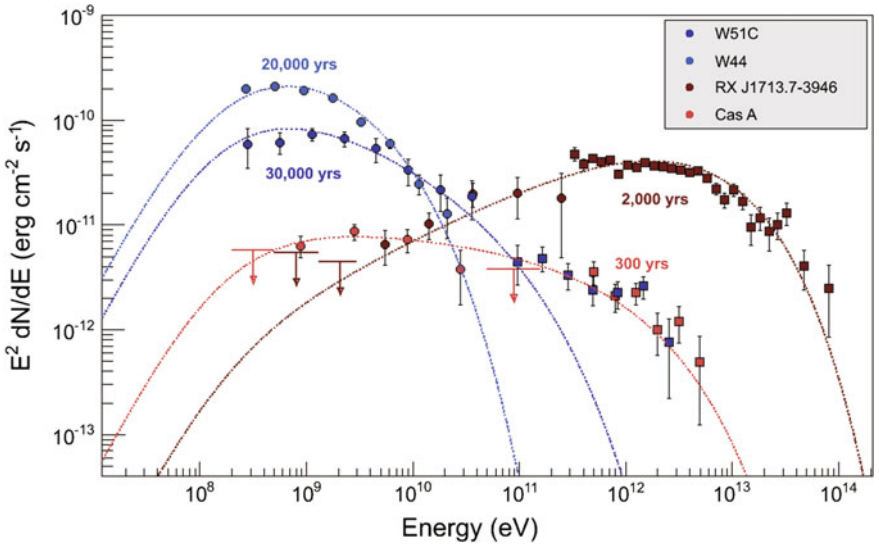

Fig. 1.6 Spectral energy distribution of γ-rays toward four typical SNRs (Funk 2012). The *filled circles* and *squares* correspond to observed positions of GeV and VHE γ-rays, respectively. Each *dashed line* indicates the expected energy spectrum from the DSA model

$\sim$10 times higher than the γ-ray energy and hence RX J1713.7−3946 is the best candidate for cosmic ray acceleration at $E_{\rm p} \sim 10^{15}$ eV. Therefore, the young SNR RX J1713.7−3946 is the best observation target for understanding efficient acceleration of cosmic ray protons above the *knee* energy.

1.5.2 Previous Studies of the Young SNR RX J1713.7−3946

Young SNR RX J1713.7−3946 (also known as G347.3−0.5) is the best target for clarifying efficient cosmic ray acceleration as this SNR emits strong synchrotron X-rays and GeV–VHE γ-rays with a shell-like structure (e.g., Acero et al. 2009; Abdo et al. 2011; Aharonian et al. 2007, see also Fig. 1.7). However, the hadronic or leptonic origin of these γ-rays has not yet been determined (as will be discussed later). The SNR has a large apparent diameter ($\sim$1°) and is located relatively close to the Galactic center at $(l, b) = (347.^{\circ}3, -0.^{\circ}5)$, where contamination by the Galactic foreground/background is heavy at any wavelength (see Fig. 1.8). Therefore, RX J1713.7−3946 was not known to be an SNR from radio continuum radiation and was discovered in the X-ray spectrum for the first time by *ROSAT* (Pfeffermann and Aschenbach 1996). After that, Koyama et al. (1997) showed using *ASCA* satellite (formerly named Astro-D) data that X-ray emission is synchrotron-radiation induced with no thermal features and is derived at a distance of 1 kpc based on a

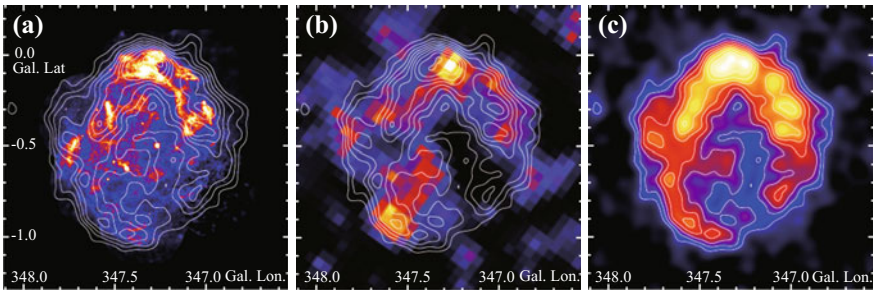

Fig. 1.7 Distribution of **a** *XMM-Newton* X-rays (Acero et al. 2009), **b** *Fermi* GeV γ-rays (Abdo et al. 2011), and **c** H.E.S.S. VHE γ-rays (Aharonian et al. 2007) toward the SNR RX J1713.7−3946. *White* contours show the H.E.S.S. VHE γ-ray intensity and are plotted every 20 smoothed counts from 20 smoothed counts

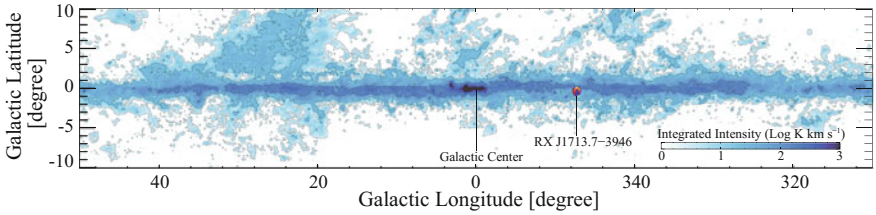

Fig. 1.8 Distribution of ^{12}CO(J = 1–0) in the Galaxy taken by the Cfa 1.2-m telescopes and the NANTEN telescope (Dame et al. 2001; Mizuno and Fukui 2004). Overlaid is the VHE γ-ray emission toward RX J1713.7−3946 with H.E.S.S (Aharonian et al. 2007)

relatively small X-ray absorption $N_{\rm H}$(X-ray), corresponding to an HI column density of $(6.2 \pm 1) \times 10^{21}\,{\rm cm}^{-2}$ for the northwest rim. Coincidentally, Wang et al. (1997) pointed out the possibility that RX J1713.7−3946 is the remnant of the AD393 guest star as recorded in Sung Shu by Shen (C.E. 500) and strongly supported a short distance of ∼1 kpc and an age of ∼1,600 year. Slane et al. (1999) suggested the possible association of a molecular cloud named "cloud A," and an LSR velocity $V_{\rm LSR}$ of ∼90 km s^{-1} from observations of the ^{12}CO(J = 1–0) emission line at 8′.8 resolution suggests a large distance of 6.3 ± 0.4 kpc. The authors also mentioned that an enhanced value of the CO $J = 2$–$1/J = 1$–0 line ratio of ∼2.0 in cloud A indicates physical interaction with the SNR shock waves. The currently determined distance to RX J1713.7−3946 of ∼1 kpc (e.g., Fukui et al. 2003) had not, as of the late 1990s, been determined. The decisive evidence of a smaller distance came from the results of a NANTEN CO survey (Mizuno and Fukui 2004) in 2003. Fukui et al. (2003) revealed the detailed structure of CO in RX J1713.7−3946 at a finer resolution of ∼2′.7 and proved the existence of interacting molecular clouds at $V_{\rm LSR}$ ∼7 km s^{-1}, which corresponds to a distance of 1 kpc.

Figure 1.9 shows the *ROSAT* X-ray image overlaid with the NANTEN ^{12}CO(J = 1–0) contours in the velocity range from −11 to −3 km s^{-1}. The authors found that the CO emission delineates the outer boundary of the SNR except for the

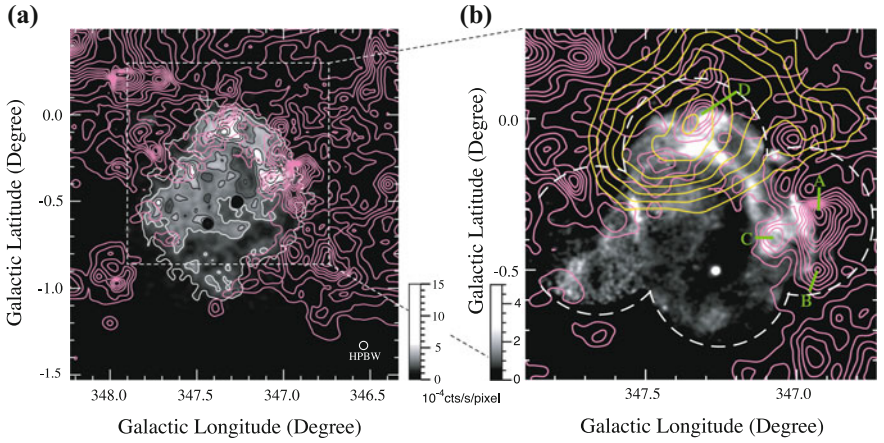

Fig. 1.9 **a** Intensity distribution of *ROSAT* X-ray image superimposed with NANTEN CO contours (Fukui et al. 2003). **b** Close-up view of RX J1713.7−3946 with *XMM-Newton* X-rays superimposed with NANTEN CO contours (*magenta*) and CANGAROO VHE γ-rays Fukui et al. (2003)

southeast region, and its peaks (named A to D in Fig. 1.9b) have good spatial correspondence with the X-ray intensity peaks, especially in the western region (upper right in Fig. 1.9). This correlation suggests that the SNR shock waves are strongly interacting with the ISM. Additionally, they also found that cloud A shows less spatial contact with the edge of the SNR and that molecular peak C has a broad wing-like component probably caused by the shock interaction. Therefore, the authors concluded that the kinematic distance and age are 1 kpc and ∼1,600 year, respectively. These physical parameters are consistent with previous studies (Pfeffermann and Aschenbach 1996; Koyama et al. 1997; Wang et al. 1997) and supported by many studies using CO and X-rays (e.g., Moriguchi et al. 2005; Cassam-Chenaï et al. 2004). In this thesis, I use these values.

The γ-ray radiation from the northwest rim of SNR RX J1713.7−3946 was detected by the CANGAROO 3.8-m atmospheric imaging Cherenkov telescope for the first time (Muraishi et al. 2000). The authors discussed the emitting process and concluded that the VHE γ-rays are mostly of leptonic origin (inverse Compton scattering), but Fukui et al. (2003)'s results suggested that the spatial correlation between the CO peak D and the VHE γ-rays provides convincing evidence for hadronic origin (see the yellow contours in Fig. 1.9b). More detailed studies of VHE γ-ray origin were performed by Aharonian et al. (2004, 2006, 2007) based on H.E.S.S. observations. The authors revealed a shell-like morphology of VHE γ-rays and compared this with the NANTEN CO distribution (Aharonian et al. 2006; see Fig. 1.10). If the hadronic process is at work, we would expect that the azimuthal profile of γ-rays is approximately proportional to that of the CO intensity. As a result, the comparative study was successful in providing a global agreement between the two measurements. However, the authors found that the correlation is not complete in the sense

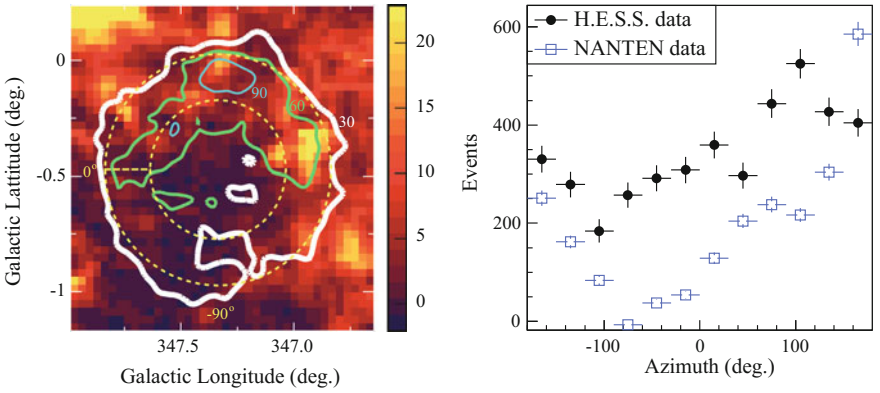

Fig. 1.10 Comparison between the H.E.S.S. VHE γ-rays and NANTEN CO (Aharonian et al. 2006). *Left* panel shows the map of the NANTEN CO image overlaid with H.E.S.S. VHE γ-ray contours. The contour levels are 30, 60, and 90 smoothed counts. *Right* panel shows azimuth profile plot of VHE γ-rays and CO between the *two dashed yellow circle* shown in the *left* panel

that the southeastern rim ($60°-90°$ in an azimuth plot) of the VHE γ-ray shell has no counterpart in CO. Therefore, although the hadronic process is the most likely the origin of the VHE γ-rays in the SNR, more detailed investigations are required.

From here on, I will describe recent progress in X-ray, GeV γ-ray measurements (and determination of the origin of the γ-rays), and numerical simulations of RX J1713.7−3946. With the beginning of the 21st century, X-ray properties of RX J1713.7−3946 began to be gradually revealed through observations with three space telescopes: *XMM-Newton*, *Suzaku*, and *Chandra*. Cassam-Chenaï et al. (2004) presented the spatial distribution of the absorbing column density $N_{\rm H}$(X-ray) and the photon index Γ obtained by *XMM-Newton*. Their maps do not have fine enough resolution for comparison with the ISM structures, but the map of $N_{\rm H}$(X-ray) has revealed strong variations over the entire SNR ($0.4 \times 10^{22}\,{\rm cm}^{-2} \leq N_{\rm H}({\rm X\text{-}ray}) \leq 1.1 \times 10^{22}\,{\rm cm}^{-2}$). The authors conducted a careful analysis of X-ray absorption using a coarse resolution of CO map (Dame et al. 2001), HI, and a star counting method, which favors a shorter distance ($d = 1.3 \pm 0.4$ kpc). Furthermore, the value of the photon index Γ has showed strong variation ($1.8 \leq \Gamma \leq 2.6$). This trend was well supported by more detailed analysis of the *XMM-Newton* data (Hiraga et al. 2005; Acero et al. 2009). Cassam-Chenaï et al. (2004) also investigated a compact central object, "1WGA J1713.4−3949," in the SNR and proposed that this point source is the compact relic of RX J1713.7−3946's supernova progenitor. Around the same time, *Chandra* revealed a filamentary structure (10″ scale) and the short time variability (∼1 year) of X-ray emissions (Uchiyama et al. 2003, 2007). This variability was deemed to be caused by rapid particle acceleration and cooling over a ∼1 year scale, leading us to believe that the cosmic ray electrons should be efficiently accelerated (so-called "Bohm diffusion regime"; Uchiyama et al. 2007) and that the magnetic field strength is ∼1 mG (∼100 times higher than that in a typical SNR). Takahashi et al. (2008) and Tanaka et al. (2008) discovered hard synchrotron

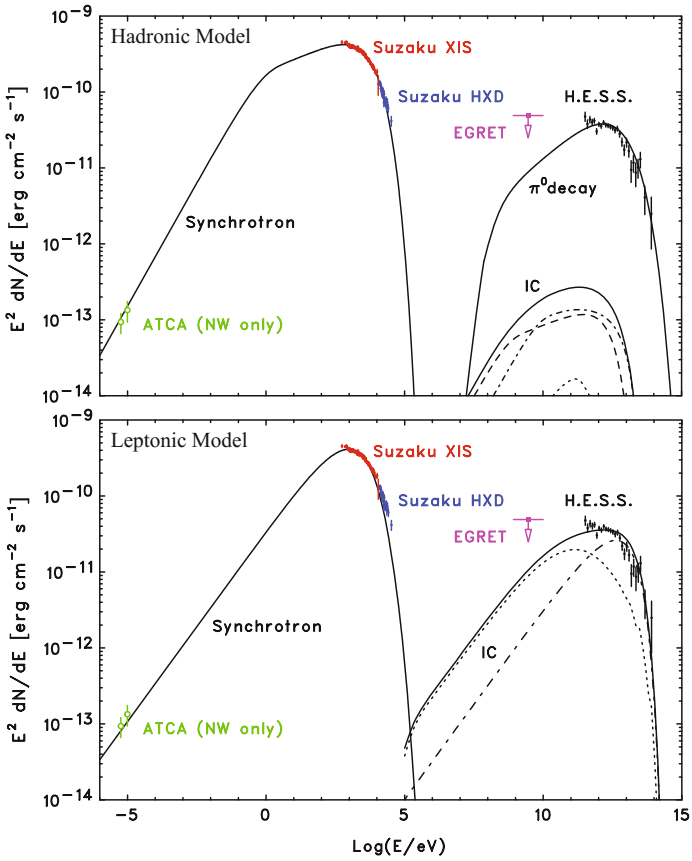

Fig. 1.11 Spectral energy distribution of RX J1713.7−3946 with a hadronic and leptonic models (Tanaka et al. 2008). The hadronic model assumes a high magnetic field $B = 200\,\mu$G. The *dash-dotted line*, *dashed line*, and *soiled lines* in the leptonic model indicate pure inverse Compton (IC) component, 2nd IC component with seed photon of additional optical radiation, and the total, respectively

X-rays of up to 40 keV emanating from the SNR using *Suzaku*. Their spectra are well fitted by an interstellar absorbed power-law function with an exponential cut-off. The authors concluded that the existence of this cut-off indicates evidence for cosmic ray electrons in the regime close to the Bohm diffusion limit (Tanaka et al. 2008; also see Sect. 1.3.2). It is not known what has triggered the efficient acceleration.

Tanaka et al. (2008) also discussed the origin of VHE γ-rays based on broad-band energy spectrum data from *Suzaku* and H.E.S.S. Figure 1.11 shows the spectral energy distributions of RX J1713.7−3946 for the hadronic and leptonic models. The DSA models can reproduce the observed data (*suzaku* XIS and HXD X-rays, and H.E.S.S. VHE γ-rays) by changing the unknown parameters such as magnetic field B and/or the amount of seed photons. According to the authors, the hadronic model is favored over the leptonic model because the high magnetic field strength $B \sim 200\,\mu$G

for the hadronic model is consistent with Uchiyama et al. (2007) and because the leptonic model assumes an unrealistic component of optical radiation with an energy density of 140 eV cm^{-3} (the typical radiation field is 0.54 eV; also see Table 1.1). Recently, the *Fermi* Large Area Telescope (LAT) revealed the GeV γ-ray spectrum of the SNR (Abdo et al. 2011, also see the significance map in Fig. 1.7) and it was concluded that the GeV to VHE γ-ray emissions are of leptonic origin.

Most recently, Inoue et al. (2009, 2012) presented magnetohydrodynamics numerical simulations of interaction between the shock and molecular and atomic gases. These indicate that the interaction between the shock waves and the **clumpy interstellar gas** excites turbulence, which amplifies the magnetic field around the clumps (Inoue et al. 2009, 2012). The authors also suggested that the presence of an amplified magnetic field would lead to a photon index of the hadronic γ-ray emission $(p - 1/2)$ identical to that of the inverse Compton emission $(p + 1)/2$ when $p = 2$, and thus, the spectra in the two scenarios are indistinguishable from that of γ-ray observation alone. Comparison of the spatial distributions of the γ-rays and the interstellar gas is the only way to distinguish whether their origins are hadronic or leptonic.

1.6 Thesis Outline

Considering the history of studies on RX J1713.7−3946, it is now necessary to study the interaction between the SNR's shock waves and its surroundings in detail[3] to understand the origin of γ-rays and the efficient mechanism of cosmic ray acceleration. This thesis will produce a decisive answer to the above questions using the CO, X-ray, and γ-ray datasets. Chapter 2 provides a quantitative relationship between the synchrotron X-rays (=cosmic ray electrons) and the interstellar gas and discusses magnetic amplification owing to the shock–cloud interaction. Chapter 3 provides evidence for cosmic ray proton acceleration by comparing the patterns of VHE γ-rays and total interstellar gas (both CO and HI). Chapter 3 proposes a scenario wherein efficient acceleration of cosmic ray electrons is caused by the shock–cloud interaction. In Chap. 4, we summarize our results and discuss future prospects for study.

References

A.A. Abdo, M. Ackermann, M. Ajello, A. Allafort, L. Baldini, J. Ballet et al., Astrophys. J. **718**, 348 (2010)

A.A. Abdo, M. Ackermann, M. Ajello, A. Allafort, L. Baldini, J. Ballet et al., Astrophys. J. **734**, 28 (2011)

[3]We note that the magnetic field strength is already known to be ∼1 mG by Uchiyama et al. (2007), although it was measured in a small region of ∼100 arcsec^2. Therefore, the overall magnetic field strength in the SNR is still unknown.

M. Abramowitz, I.A. Stegun, *Dover Books on Advanced Mathematics*, Corrected edition, ed. by Milton Abramowitz, Irene A Stegun (Dover, New York, 1965)
F. Acero, J. Ballet, A. Decourchelle, M. Lemoine-Goumard, M. Ortega, E. Giacani et al., Astrophys. J. **505**, 157 (2009)
F.A. Aharonian, A.M. Atoyan, Astron. Astrophys. **309**, 917 (1996)
F.A. Aharonian, A.G. Akhperjanian, K.-M. Aye, A.R. Bazer-Bachi, M. Beilicke, W. Benbow et al., Nat. **432**, 75 (2004)
F. Aharonian, A.G. Akhperjanian, A.R. Bazer-Bachi, M. Beilicke, W. Benbow, D. Berge et al., Astron. Astrophys. **449**, 223 (2006)
F. Aharonian, A.G. Akhperjanian, A.R. Bazer-Bachi, M. Beilicke, W. Benbow, D. Berge et al., Astron. Astrophys. **464**, 235 (2007)
F. Aharonian, A.G. Akhperjanian, A.R. Bazer-Bachi, B. Behera, M. Beilicke, W. Benbow et al., Astron. Astrophys. **481**, 401 (2008)
Y. Arikawa, K. Tatematsu, Y. Sekimoto, T. Takahashi, Publ. Astron. Soc. Jpn. **51**, L7 (1999)
A. Bamba, G. Pühlhofer, F. Acero, D. Klochkov, W. Tian, R. Yamazaki et al., Astrophys. J. **756**, 149 (2012)
J.J. Beatty, S. Westerhoff, Annu. Rev. Nucl. Part. Sci. **59**, 319 (2009)
C.L. Brogan, J.D. Gelfand, B.M. Gaensler, N.E. Kassim, T.J.W. Lazio, Astrophys. J. Lett. **639**, L25 (2006)
G. Cassam-Chenaï, A. Decourchelle, J. Ballet, J.-L. Sauvageot, G. Dubner, E. Giacani et al., Astron. Astrophys. **427**, 199 (2004)
T.M. Dame, D. Hartmann, P. Thaddeus, Astrophys. J. **547**, 792 (2001)
L.K. Denoyer, Astrophys. J. Lett. **232**, L165 (1979)
B.T. Draine, *Physics of the Interstellar and Intergalactic Medium* (Princeton University Press, New Jersey, 2011)
G.M. Dubner, P.F. Velázquez, W.M. Goss, M.A. Holdaway, Astron. J. **120**, 1933 (2000)
D.J. Fixsen, Astrophys. J. **707**, 916 (2009)
Y. Fukui, T. Onishi, R. Abe, A. Kawamura, K. Tachihara, R. Yamaguchi et al., Publ. Astron. Soc. Jpn. **51**, 751 (1999)
Y. Fukui, Y. Moriguchi, K. Tamura, H. Yamamoto, Y. Tawara, N. Mizuno et al., Publ. Astron. Soc. Jpn. **55**, L61 (2003)
S. Funk, APS April Meeting Abstracts, 3002 (2012)
S. Gabici, Cosm. Rays Star-Form. Environ. **34**, 221 (2013)
V.L. Ginzburg, S.I. Syrovatskii, *The Origin of Cosmic Rays* (Macmillan, New York, 1964)
A. Giuliani, M. Tavani, A. Bulgarelli, E. Striani, S. Sabatini, M. Cardillo et al., Astron. Astrophys. **516**, L11 (2010)
S. Hayakawa, Prog. Theor. Phys. **8**, 571 (1952)
C. Heiles, R. Crutcher, Cosm. Magn. F. **664**, 137 (2005)
A.M. Hillas, Annu. Rev. Astron. Astrophys. **22**, 425 (1984)
J.S. Hiraga, Y. Uchiyama, T. Takahashi, F.A. Aharonian, Astron. Astrophys. **431**, 953 (2005)
T. Inoue, R. Yamazaki, S.-I. Inutsuka, Astrophys. J. **695**, 825 (2009)
T. Inoue, R. Yamazaki, S.-I. Inutsuka, Y. Fukui, Astrophys. J. **744**, 71 (2012)
J.W. Keohane, J. Rho, T.G. Pannuti, K.J. Borkowski, P.F. Winklery, X-Ray and Radio Connections (2005)
K. Koyama, R. Petre, E.V. Gotthelf, U. Hwang, M. Matsuura, M. Ozaki et al., Nat. **378**, 255 (1995)
K. Koyama, K. Kinugasa, K. Matsuzaki, M. Nishiuchi, M. Sugizaki, K. Torii et al., Publ. Astron. Soc. Jpn **49**, L7 (1997)
A. Mizuno, Y. Fukui, Milky W. Surv. Struct. Evol. Galaxy **317**, 59 (2004)
Y. Moriguchi, K. Tamura, Y. Tawara, H. Sasago, K. Yamaoka, T. Onishi et al., Astrophys. J. **631**, 947 (2005)
H. Muraishi, T. Tanimori, S. Yanagita, T. Yoshida, M. Moriya, T. Kifune et al., Astron. Astrophys. **354**, L57 (2000)

E. Pfeffermann, B. Aschenbach, in *Proceedings of Roentgenstrahlung from the Universe*, ed. by H.U. Zimmermann, J.H. Trümper, H. Yorke, vol. 267 (1996)
J. Rho, K.J. Borkowski, Astrophys. J. **575**, 201 (2002)
G.B. Rybicki, A.P. Lightman, *Radiative Processes in Astrophysics* (Wiley-Interscience, New York, 1979)
M. Seta, T. Hasegawa, T.M. Dame, S. Sakamoto, T. Oka, T. Handa et al., Astrophys. J. **505**, 286 (1998)
P. Slane, B.M. Gaensler, T.M. Dame, J.P. Hughes, P.P. Plucinsky, A. Green, Astrophys. J. **525**, 357 (1999)
P. Slane, J.P. Hughes, R.J. Edgar, P.P. Plucinsky, E. Miyata, H. Tsunemi et al., Astrophys. J. **548**, 814 (2001)
T. Takahashi, T. Tanaka, Y. Uchiyama et al., Publ. Astron. Soc. Jpn. **60**, 131 (2008)
T. Tanaka, Y. Uchiyama, F.A. Aharonian, T. Takahashi, A. Bamba, J.S. Hiraga et al., Astrophys. J. **685**, 988 (2008)
W.W. Tian, Z. Li, D.A. Leahy, J. Yang, X.J. Yang, R. Yamazaki et al., Astrophys. J. **712**, 790 (2010)
Y. Uchiyama, F.A. Aharonian, T. Takahashi, Astron. Astrophys. **400**, 567 (2003)
Y. Uchiyama, F.A. Aharonian, T. Tanaka, T. Takahashi, Y. Maeda, Nat. **449**, 576 (2007)
Z.R. Wang, Q.-Y. Qu, Y. Chen, Astron. Astrophys. **318**, L59 (1997)
H.A. Wootten, Astrophys. J. **216**, 440 (1977)
A. Wootten, Astrophys. J. **245**, 105 (1981)
S. Yoshiike, T. Fukuda, H. Sano, A. Ohama, N. Moribe, K. Torii et al., Astrophys. J. **768**, 179 (2013)
S. Yoshiike, T. Fukuda, H. Sano et al. in preparation (2016)
V.N. Zirakashvili, F. Aharonian, Astron. Astrophys. **465**, 695 (2007)

Chapter 2
Non-thermal X-Ray Enhancement Around Dense Gas Clumps

Supernova remnants (SNRs) have a profound influence on the interstellar medium (ISM) via shock interaction and injection of heavy elements. If the ISM is dense enough, this dynamical interaction can also affect the evolution of an SNR through the distortion of its shell morphology. It is therefore important to study the detailed physical properties of the interaction between SNRs and ISM to understand what can occur.

RX J1713.7−3946 is a unique SNR emitting very high energy (VHE, Energies $E > 100$ GeV) γ-rays and X-rays, which are likely emitted by cosmic ray particles accelerated in the SNR via diffusive shock acceleration (DSA; see Sect. 1.3.2 for details). Note that the X-rays of the SNR are purely non-thermal synchrotron emissions, indicating that cosmic ray electrons are accelerated in the SNR up to the 10 TeV range; in addition to RX J1713.7−3946, only two known SNRs produce such non-thermal X-rays: RX J0852.0−4622 (Vela Jr.) and HESS J1731−347 (e.g., Koyama et al. 1997; Slane et al. 2001; Tian et al. 2010). Detailed theoretical modeling of this high-energy radiation made over a wide range of physical parameters appropriate for the SNR has shown that the observed properties of high energy radiation can be reproduced under reasonable sets of physical parameters relevant to cosmic ray acceleration (e.g., Zirakashvili and Aharonian 2007, 2010). It is thus becoming increasingly important to observationally constrain the physical parameters of the SNR (such as its magnetic field) and their distributions.

As mentioned in Sect. 1.5.2, molecular clumps interacting with SNR RX J1 713.7−3946 were discovered in the ^{12}CO($J = 1$–0) emission at $V_{\rm LSR}$, the rest velocity with respect to the local reference frame (around -7 km s^{-1}). This shows that the distribution of the CO emission in RX J1713.7−3946 correlates well with the X-ray distribution in pc scale (Fukui et al. 2003, see Fig. 1.9 in Sect. 1.5.2); the northwestern rim of the X-ray image coincides with the most prominent CO peaks (Fukui et al. 2003; Moriguchi et al. 2005; Fukui 2008). This X-ray distribution is now theoretically interpreted as being caused by interaction between the shock front and the molecular clumps, as modeled in the magnetohydrodynamic (MHD) numerical simulations

H. Sano, *Shock-Cloud Interaction in RX J1713.7–3946*,
Springer Theses, DOI 10.1007/978-4-431-55636-7_2

by Inoue et al. (2009, 2012). This correlation provides a robust verification of the physical association of the CO clumps with the non-thermal X-ray shell. **However, to date, there has not been a quantitative study to clarify the connection among the X-rays, ISM clumps, and accelerated cosmic ray electrons.**

Furthermore, Fukui et al. (2003) found that CO peak C shows broad CO wings and suggested that these may result from dynamical acceleration by the SNR blast wave. Such broad molecular wings are found in several SNRs, including IC443, W44, and W28. (e.g., Denoyer 1979; Wootten 1977, 1981). Moriguchi et al. (2005) showed that the ^{12}CO(J = 3–2) distribution in peak C shows a hint of bipolarity, which could possibly be associated with the presence of an infrared compact source with the spectrum of a protostar. This may indicate an alternative possibility that the broad wings are driven by the outflow from a protostar rather than a shock interaction. The question whether the SNR is accelerating molecular gas to high velocities in peak C is yet unanswered. It is therefore important to clarify whether the CO broad wings are caused by blast-wave acceleration or protostellar activity.

In this chapter, we establish a connection between synchrotron X-rays and the surrounding ISM distribution. The present work is aimed at better understanding the SNR shock-cloud interaction and thereby establishing the origin of the distribution of synchrotron X-rays in SNR RX J1713.7−3946. This study will be extended to the other SNRs with non-thermal features, allowing us to deepen our understanding of the role of the interaction between high energy radiation and cosmic ray acceleration in the ISM. In this work, we show a comparison of the spatial distribution among CO, HI, and X-rays over the entire SNR to clarify the relationship between the dense gas and the high-energy electrons. Furthermore, we reveal the molecular properties of the core of RX J1713.7−3946, the broad wings in peak C, and the other cloud cores nearby.

2.1 Datasets of CO, HI, and X-Rays

2.1.1 CO

We conducted ^{12}CO(J = 2–1, 4–3) and ^{13}CO(J = 2–1) observations using the NANTEN2 4-m sub-mm telescope belonging to Nagoya University, which is installed at Pampa La Bola (4865 m above the sea level) in northern Chile.

The ^{12}CO(J = 2–1) and ^{13}CO(J = 2–1) data at 230 GHz were gathered from August to November 2008. The telescope used a 4 K cooled double sideband (DSB) receiver as a front end and had a typical system temperature of ∼250 K in the single sideband (SSB), including the atmosphere toward zenith. The telescope has an angular resolution (full width at half maximum; FWHM) of 90″ at 230 GHz. We used an acoustic optical spectrometer with 2,048 channels, a bandwidth of 390 km s^{-1}, and resolution per channel of 0.38 km s^{-1}. Observations in ^{12}CO(J = 2–1) were conducted in on-the-fly (OTF) mode with an integration time of 1.0 or

2.0 s per grid, producing a Nyquist-sampled 30″ grid dataset. The telescope has a beam size of 90″ at 230 GHz. The ambient temperature load was employed for intensity calibration. The absolute intensity scale was estimated by observing the Ori KL object [$5^h35^m14\overset{s}{.}52$; $-5°22'28\overset{''}{.}2$ (J2000)] (Schneider et al. 1998) at the ^{12}CO(J = 2–1) line. The main beam efficiency, η_{mb}, was estimated to be 0.83. The rms noise fluctuations with 1.0 and 2.0 s integrations were better than 0.66 and 0.51 K per channel, respectively. The pointing accuracy was estimated to be better than ∼15″ through two-hourly observations of Jupiter. Images were smoothed by means of a Gaussian kernel with a FWHM of 60″. Observations in ^{13}CO, including peaks A, B, C, and D, were conducted in the OTF mode over an area of 22 arcmin^2 (Moriguchi et al. 2005) with an integration time of 2.0 s, producing a Nyquist-sampled 30″ grid dataset. The pointing accuracy for this task was also checked through two-hourly Jupiter observations and was found to be as accurate as ∼15″, and the rms noise fluctuations were better than 0.68 K per channel. The ambient temperature load was also employed for absolute intensity calibration, which was calibrated by observing Oph EW4 [$16^h26^m21\overset{s}{.}92$; $-24°25'40\overset{''}{.}4$ (J2000)] (Kulesa et al. 2005).

Observations in ^{12}CO(J = 4–3) were conducted from November to December 2007 over a 9 arcmin^2 region, including peak C and toward a point in peak A. The telescope has a beam size of 38″ at 460 GHz, as measured by observing Jupiter. A SIS receiver with an SSB temperature of 300 K including the atmosphere toward zenith was used as a front end. The typical rms noise fluctuations were 0.28 K per channel, and absolute intensity calibration was conducted as described by Pineda et al. (2008).

In addition, we used the ^{12}CO(J = 1–0) data at 115 GHz taken with the NANTEN 4-m telescope, as published in Moriguchi et al. (2005). The angular resolution of the data is 2.′6 (FWHM) and the velocity resolution and rms noise fluctuations are 0.65 km s^{-1} and 0.3 K, respectively. Observations were conducted in position-switching mode with a 2′ grid spacing (for more detailed information, see also Moriguchi et al. 2005). The ^{12}CO(J = 2–1) data were used for comparison with the X-ray images, whereas the ^{12}CO(J = 1–0) data was primarily used to estimate molecular mass from the integrated ^{12}CO intensity $W(^{12}\mathrm{CO})$ (K km s^{-1}) using the relationship $N(\mathrm{H_2}) = X_{\mathrm{CO}} \cdot [W(^{12}\mathrm{CO})\ (\mathrm{K\ km\ s^{-1}})]\ (\mathrm{cm^{-2}})$ with an X_{CO} factor of 2.0×10^{20} (cm^{-2} (K km s^{-1})$^{-1}$) (Bertsch et al. 1993).

We also used the data produced by Moriguchi et al. (2005). They observed the peaks A, C, and D with the ASTE sub-mm telescope in ^{12}CO(J = 3–2) in November 2004. These data were taken in position-switching mode with a 30″ grid spacing using a 23″ beam. An AOS spectrometer with a 450 km s^{-1} bandwidth and 0.43 km s^{-1} resolution was used. The system temperature was 300–400 K (DSB) and the typical rms achieved was 0.4–0.9 K with 30 s integration. The observed regions are shown in Fig. 2.1.

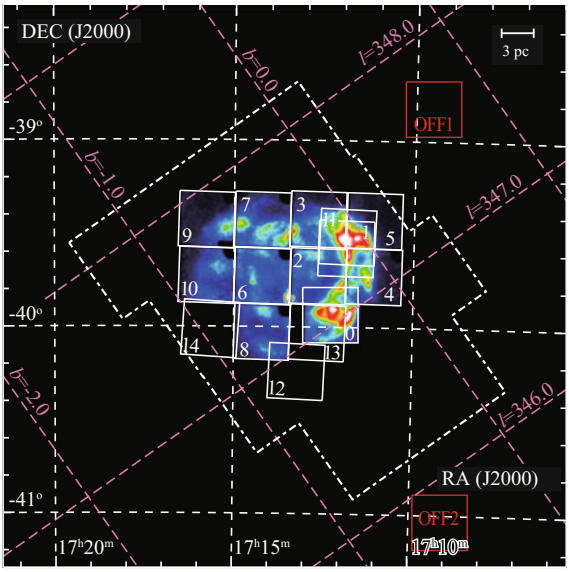

Fig. 2.1 *Suzaku* FoV of each observation of RX J1713.7−3946 overlaid on the *Suzaku* XIS 0+2+3 mosaic image (1–5 keV) taken from Tanaka et al. (2008). The small squares correspond to the FoV of the XIS. The numbers in the XIS FoV are pointing IDs used throughout this paper (see also Table 2.1). We also show the observed area in the ^{12}CO(J = 1–0, 2–1, 3–2, 4–3) and ^{13}CO(J = 2–1) enclosed by *white*, *red*, *green*, *yellow*, and *orange dash-dotted lines*, respectively

2.1.2 HI

The 21-cm HI spectral data were produced by the Southern Galactic Plane Survey (SGPS; McClure-Griffiths et al. 2005) using the Australia Telescope Compact Array (ATCA) combined with the 64-m Parkes Radio Telescope. The combined beam size and the grid spacing of the dataset are 2′.2 and 40″, respectively, and the velocity resolution and typical rms noise fluctuations are 0.82 km s^{-1} and 1.9 K, respectively. We applied a correction for HI self-absorption following the previous analysis of cold HI gas without CO emission (see Sect. 3.2.3.3).

2.1.3 X-Rays

We used *Suzaku* archive data of RX J1713.7−3946 taken from the Data Archives and Transmission System (DARTS at ISAS/JAXA). These observations comprising 15 pointings toward the main features and 2 OFF pointings of RX J1713.7−3946 and, excluding the four pointings observed in February 2010, were published by Takahashi et al. (2008) and Tanaka et al. (2008). Previous and current observations are summarized in Table 2.1, and the FoV of each observation is shown in Fig. 2.1. The *Suzaku* satellite has two active detector systems: the X-ray Imaging Spectrometer (XIS; Koyama et al. 2007) and the Hard X-ray Detector (HXD; Takahashi et al. 2007). The XIS comprises four CCD cameras, each of which is placed at the focus of an X-ray Telescope module (XRTs; Serlemitsos et al. 2007). For this work, we

Table 2.1 Summary of the *Suzaku* archive data of RX J1713.7−3946

Pointing ID	ObsID	α_{J2000} (^{h} ^{m} ^{s})	δ_{J2000} ($^{\circ}$ $'$ $''$)	XIS Exp. (ks)	Date	SCI
0.....	100026010	17 12 17.0	−39 56 11	69	September 26, 2005	OFF
1.....	501063010	17 11 51.5	−39 31 13	18	September 11, 2006	OFF
2.....	501064010	17 12 38.0	−39 40 14	21	September 11, 2006	OFF
3.....	501065010	17 12 38.2	−39 22 15	22	September 11, 2006	OFF
4.....	501066010	17 11 04.5	−39 40 10	21	September 12, 2006	OFF
5.....	501067010	17 11 05.1	−39 22 10	21	September 12, 2006	OFF
6.....	501068010	17 14 11.6	−39 40 14	21	September 13, 2006	OFF
7.....	501069010	17 14 11.4	−39 22 15	18	September 19, 2006	OFF
8.....	501070010	17 14 11.8	−39 58 14	21	September 19, 2006	OFF
9.....	501071010	17 12 17.6	−39 18 50	21	September 20, 2006	OFF
10.....	501072010	17 15 44.5	−39 40 10	20	October 5, 2006	OFF
11.....	504027010	17 11 50.8	−39 31 00	62	February 15, 2010	ON
12.....	504028010	17 13 14.0	−40 14 22	19	February 16, 2010	ON
13.....	504029010	17 12 39.8	−40 01 50	21	February 17, 2010	ON
14.....	504030010	17 15 39.0	−40 00 47	22	February 17, 2010	ON
OFF1.....	100026020	17 09 31.9	−38 49 24	35	September 25, 2005	OFF
OFF2.....	100026030	17 09 05.1	−41 02 07	38	September 28, 2005	OFF

Notes The details of pointing IDs from 0 to 10, OFF1, and OFF2 are also shown in Takahashi et al. (2008) and Tanaka et al. (2008)

analyzed only XIS data. The spaced-row charge injection (SCI; Nakajima et al. 2008; Uchiyama et al. 2009) was used in the latter four pointings (see also Table 2.1). Unfortunately, XIS 2 has been out of service since 9 November 2006, possibly owing to micrometeorite damage, and XIS 0 incurred anomaly in Segment A on June 23, 2009. Thus, to obtain data from the latter four pointings, we used XIS 0 (excluding data for Segment A), XIS 1, and XIS 3. To do so, we used "cleaned event files" that were processed and screened by versions 2.0 or 2.4 of the *Suzaku* pipeline depending on observation dates. We first created photon count images from the cleaned event files in the 1–5 and 5–10 keV energy bands, which were produced by subtracting the non-X-ray background (NXB) using **xisnxbgen**, which estimates the NXB count rate based on night time Earth observation data. We then corrected for XRT vignetting effects by simulating flat field images using **xissim** (Ishisaki et al. 2007). In addition, we masked calibration sources in the region of ^{55}Fe in the 5–10 keV energy band. Finally, we smoothed the images using a Gaussian kernel with a FWHM of 45″. We performed data reduction using version 6.11 of the HEAsoft tools.

2.2 Analysis

2.2.1 *Large-Scale CO, HI, and X-Ray Distributions*

Figure 2.2 shows mosaic images of RX J1713.7−3946 that were constructed by using data from XIS 0+1+2+3. Figure 2.2a and b show soft band (1–5 keV) and hard band (5–10 keV) images, respectively. The unit for the images is 10^{-4} counts s^{-1} $pixel^{-1}$ and the pixel size is $\sim 16\farcs7$. We find that the soft and hard band images are very similar, as was discussed in the previous study by Tanaka et al. (2008). Figure 2.2 clearly shows the western rim as well as several peaks of $\sim 10 \times 10^{-4}$ counts s^{-1} $pixel^{-1}$ in the northern rim and inside the SNR. In the soft band image,

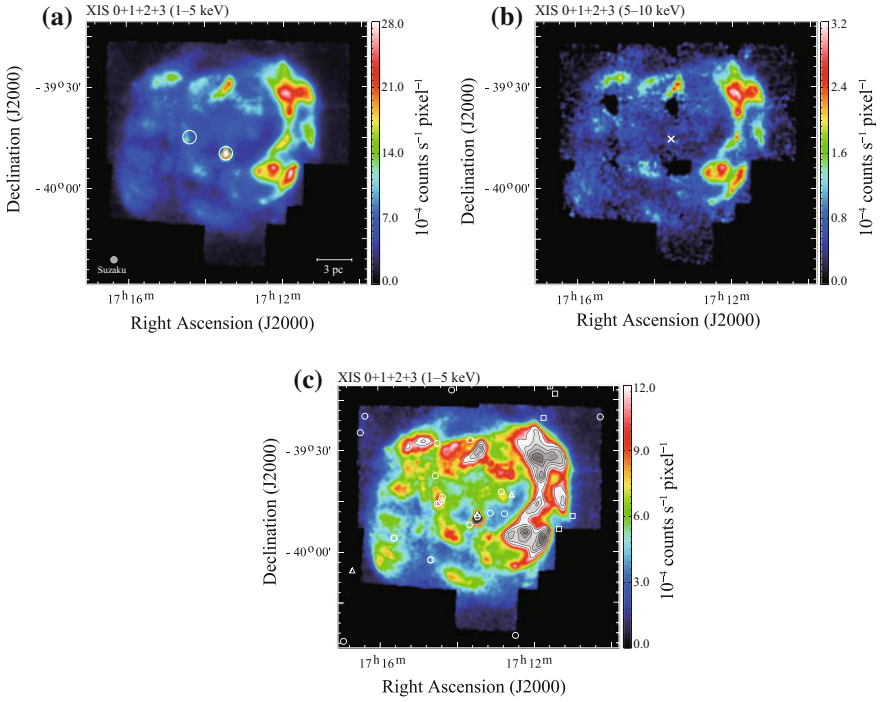

Fig. 2.2 *Suzaku* XIS (XIS 0+1+2+3) mosaic images of RX J1713.7−3946 in the **a** 1–5 keV and **b** 5–10 keV energy bands. The color scale indicates the count rate on a linear scale. The color bar numbers are in units of 10^{-4} counts s^{-1} $pixel^{-1}$ with a pixel size of $\sim 16\farcs7$. Both images are smoothed using a Gaussian kernel with an FWHM of 45″. The positions of the two point-like sources are shown with large circles in (**a**) (see Table 2.2). **c** Same XIS mosaic image (1–5 keV) as (**a**) but with the color scale changed to emphasize the region of low photon counts (below 12 × 10^{-4} counts s^{-1} $pixel^{-1}$). Regions above this level are shown in *gray* scale; the lowest contour level and the contour interval are 12 and 4 × 10^{-4} counts s^{-1} $pixel^{-1}$, respectively. The small *circles*, *triangles*, and *squares* show the position of seven X-rays point source, three pulsars, and two Wolf–Rayet stars, respectively

thick white circles indicate locations of the two bright point-like sources toward the inner part of the SNR. The left source is associated with a Wolf–Rayet star CD−39 11212B (Pfeffermann and Aschenbach 1996), which corresponds to two cataloged X-ray point sources (1WGA J1714.4−3945 and EXO 1710−396; see also Table 2.2). Owing to its X-ray spectral characteristics, the other source is thought to be a neutron star (Lazendic et al. 2003), which is cataloged as an X-ray point source (1WGA J1713.4−3949) and a pulsar (PSR J1713−3949). We also show a modified color scale image in the 1–5 keV energy band, which enhances the regions of the low photon count $\sim 7 \times 10^{-4}$ counts s^{-1} $pixel^{-1}$. In addition to the localized peaks in X-rays, we find diffuse X-ray emission extended within the SNR. To estimate the level of the background X-rays in the 1–5 keV X-ray image, we show two histograms of X-ray counts in Figure D1 (see Appendix D); one corresponds to the entire region observed by *Suzaku* (Fig. 2.1), whereas the other corresponds to nine $6'$ diameter circles without significant peaks inside the SNR (Figure D1). In the latter histogram, there is a peak at $\sim 3.86 \times 10^{-4}$ counts s^{-1} $pixel^{-1}$ that we identify as the background within the SNR. Similarly, we believe that a primary peak at $\sim 1.16 \times 10^{-4}$ counts s^{-1} $pixel^{-1}$ for the entire region indicates the background level outside the SNR. In Fig. 2.2c we plot the positions of the X-ray point sources, pulsars, and Wolf–Rayet stars (Table 2.2) in order to test whether the X-ray distribution is influenced by these point sources. As we see no excess in the regions around these point sources (except for the two bright point-like sources marked in the figure), we conclude that the X-ray features inside the SNR are not caused by the point sources but are intrinsic to the SNR.

Figure 2.3 shows four overlays of the ^{12}CO(J = 2–1) distribution and X-ray images in the 1–5 keV (Fig. 2.3a and b) and 5–10 keV (Fig. 2.3c and d) energy bands, respectively. A V_{LSR} range of CO from −20.2 to −9.1 km s^{-1} is shown in Fig. 2.3a and c and that from −9.1 to 1.8 km s^{-1} in Fig. 2.3b and d. These velocity ranges correspond to those of the interacting molecular gas (Fukui et al. 2012). Figure 2.3 indicates that CO and X-rays show good correlation at a pc scale, as already noted by Moriguchi et al. (2005). It is remarkable that most of the X-ray features are found toward CO clumps. The most outstanding X-ray flux is seen in the west of the shell, where the strongest CO emission is located (Fig. 2.3b and d); the second brightest X-ray regions are seen in the north of the shell, where CO emission is also distributed (Fig. 2.3a and c). The southern part of the CO emission appears to delineate the southern rim of the SNR (Fig. 2.3b and d), whereas the eastern shell with weak X-rays has only a few small CO features (Fig. 2.3b and d).

The CO distribution in the region of RX J1713.7−3946 is highly clumpy. To make a detailed comparison with the X-ray distribution, we cataloged CO clumps in the ^{12}CO(J = 1–0) data in Figure A1 in Appendix A. We identified 22 CO clumps in total, which were selected from the ^{12}CO(J = 1–0) data using the following three criteria: (1) the peak position is located within the SNR boundary, (2) the peak brightness temperature is higher than 1 K, and (3) the total clump surface area defined as the region surrounded by the contour at half of the maximum integrated intensity is larger than a three-beam area. We give the observed parameters of these clumps in ^{12}CO(J = 1–0) and ^{12}CO(J = 2–1) in Table 2.3. Thirteen of these are identified

Table 2.2 Summary of the X-ray point sources toward RX J1713.7−3946

Name	α_{J2000} ($^h\ ^m\ ^s$)	δ_{J2000} ($^\circ\ '\ ''$)	Source type	Ref.
2MASS J17110082−3949312	17 11 00.820	−39 49 31.22	Wolf–Rayet star	1
WR 84	17 11 21.70	−39 53 22.2	Wolf–Rayet star[a]	2
CD−39 11212B	17 14 27.129	−39 45 47.25	Wolf–Rayet star	1
2MASS J17112850−3913168	17 11 28.502	−39 13 16.88	Wolf–Rayet star	1
2MASS J17113611−3911079	17 11 36.118	−39 11 07.95	Wolf–Rayet star	1
2MASS J17114613−3920277	17 11 46.133	−39 20 27.78	Wolf–Rayet star	1
2MASS J17142712−3945472	17 14 27.129	−39 45 47.25	Wolf–Rayet star	1
PSR J1712−3943A	17 12 35.0	−39 43 14	pulsar	3
PSR J1712−3943B	17 12 35.0	−39 43 14	pulsar	3
PSR J1713−3949	17 13 28	−39 49.0	pulsar[a]	4
PSR J1716−4005	17 16 42.06	−40 05 27.0	pulsar	5
1RXS J171019.3−392006	17 10 19.298	−39 20 06.50	X-ray source	6
1RXS J171229.0−402459	17 12 28.997	−40 24 59.51	X-ray source	6
EXMS B1709−397A	17 12 46	−39 48.9	X-ray source	7
GPS 1709−396	17 12 51.0	−39 42 25	X-ray source	8
EXMS B1709−397B	17 13 08	−39 48.7	X-ray source	7
1WGA J1713.4−3949	17 13 28	−39 49.8	X-ray source[a]	4, 9
2XMM J171338.9−392658	17 13 38.91	−39 26 58.4	X-ray source	10
CXOPS J171340.5−395213	17 13 40.5	−39 52 13	X-ray source	11
AX J1714.1−3912	17 14 07.0	−39 12 12	X-ray source	12
EXO 1710−396	17 14 22	−39 44.0	X-ray source[b]	13
1WGA J1714.4−3945	17 14 24	−39 45	X-ray source[b]	14, 15
2XMM J171429.6−394559	17 14 29.72	−39 45 59.8	X-ray source	10
2XMM J171429.7−392801	17 14 29.74	−39 28 01.5	X-ray source	10
CXOU J171432.4−393735	17 14 32.48	−39 37 35.3	X-ray source	16
CXOPS J171440.6−400234	17 14 40.6	−40 02 34	X-ray source	11
2XMM J171440.7−400232	17 14 40.7	−40 02 32	X-ray source	10
CXOPS J171537.1−395559	17 15 37.1	−39 55 59	X-ray source	11
2XMM J171537.0−395559	17 15 37.0	−39 55 59	X-ray source	10
1RXS J171620.2−391946	17 16 20.201	−39 19 46.49	X-ray source	6
1RXS J171627.5−392439	17 16 27.502	−39 24 39.49	X-ray source	6
1RXS J171657.1−402627	17 16 57.101	−40 26 26.99	X-ray source	6

Notes [a] and [b] sources are connected with two X-ray point-like sources shown in Fig. 2.2, respectively. (1) Cutri et al., 2003; (2) van der Hucht, 2001; (3) Burgay et al., 2006; (4) Lazendic et al., 2003; (5) Eatough et al., 2013; (6) Voges et al., 1999; (7) Reynolds et al., 1999; (8) Gottwald et al., 1995; (9) Landt and Bignall, 2008; (10) Lin et al., 2012; (11) van den Berg et al., 2012; (12) Uchiyama et al., 2002; (13) Lu et al., 1996; (14) Slane et al., 1999; (15) Pfeffermann and Aschenbach, 1996; (16) Guillot et al., 2009

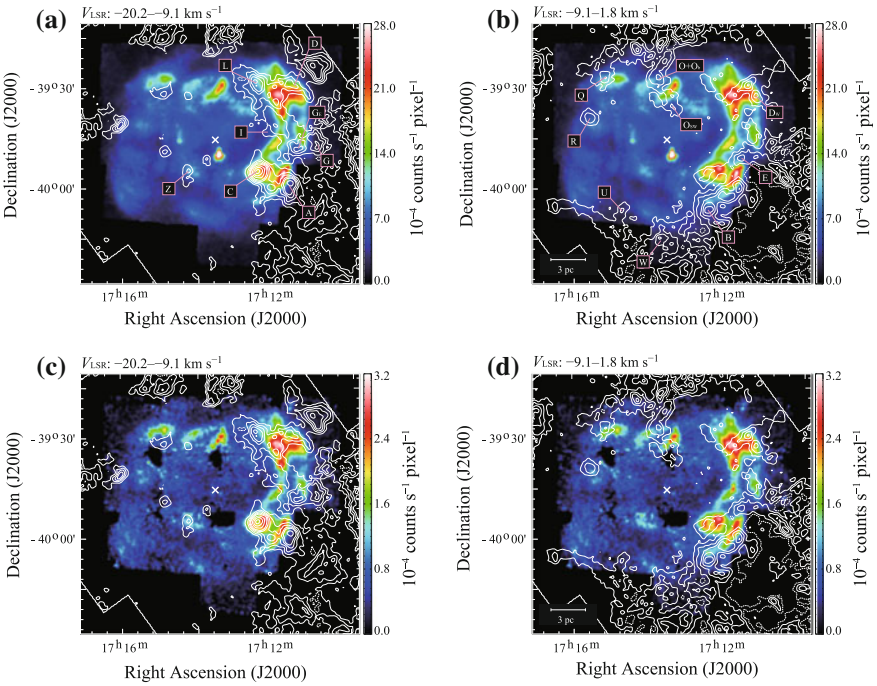

Fig. 2.3 Pair of ^{12}CO($J = 2$–1) velocity channel maps (*white contours*) superimposed on the *Suzaku* XIS mosaic image in two energy bands (**a**, **b**: 1–5 keV and, **c**, **d**: 5–10 keV) in color scale. The velocity ranges are **a**, **c** −20.2–−9.1 km s^{-1} and **b**, **d** −9.1–1.8 km s^{-1}, respectively. The lowest contour level and the contour interval of CO are 3.1 K km s^{-1} ($\sim 3\sigma$) in **b** and **d**, respectively. In **a** and **c**, the contour levels are 3.1, 6.2, 9.3, 12.4, 15.5, 21.7, 27.9, and 31.0 K km s^{-1}. The CO clumps discussed in Sect. 2.2.2 are indicated in the figure

either by Fukui et al. (2003) or Moriguchi et al. (2005); the rest are newly identified in the present work. Most of the CO clumps have a single velocity component of line width ∼3–5 km s^{-1}. Only clump O (Moriguchi et al. 2005) has two velocity components with ∼7.5 km s^{-1} separation, and it is divided into two clumps, O and O$_b$. Five of the clumps D$_W$, G$_E$, O$_b$, O$_{SW}$, and Z have molecular mass higher than 50 $M_\odot$ (see also Table 2.3), whereas four of them C$_E$, Q$_W$, Z$_{NW}$, and Z$_{NE}$ have molecular mass less than 50 $M_\odot$. We focus hereafter on the 18 CO clumps having molecular mass greater than 50 $M_\odot$, as shown in Fig. 2.3, to ensure consistent derivation of physical parameters for a quantitative comparison with the X-ray characteristics (Sect. 2.1.3). Except for the five clumps C, I, L, O$_{SW}$, and Z, which are located inside the SNR boundary, most of the clumps (A, B, D, D$_W$, E, G, G$_E$, O, O$_b$, Q, R, U, and W) are distributed on the outer boundary of the SNR shell.

Finally, we compare the cold HI gas without CO with the X-rays in the southeastern rim of the SNR (hereafter SE rim; see Sect. 3.2.3.3). The cold HI gas has a density of around 100 cm^{-3} and is likely interacting with the shock in a similar way to the CO.

Table 2.3 Properties of CO clumps

Name (1)	^{12}CO($J = 1$–0)						^{12}CO($J = 2$–1)				
	α_{J2000} (^{hms}) (2)	δ_{J2000} ($^{\circ\prime\prime\prime}$) (3)	T_{R^*} (K) (4)	V_{peak} (km s^{-1}) (5)	ΔV_{LSR} (km s^{-1}) (6)	Mass ($M_\odot$) (7)	α_{J2000} (^{hms}) (8)	δ_{J2000} ($^{\circ\prime\prime\prime}$) (9)	T_{R^*} (K) (10)	V_{peak} (km s^{-1}) (11)	ΔV_{LSR} (km s^{-1}) (12)
A.....	17 11 35.9	−39 59 01.8	8.5	−10.3	4.8	686	17 11 38.4	−39 58 46.9	6.6	−10.0	4.5
B.....	17 12 26.5	−40 06 06.3	4.2	−8.0	4.6	190	17 12 26.8	−40 05 55.5	3.3	−8.1	4.5
C.....	17 12 25.9	−39 56 04.4	9.4	−12.0	3.8	397	17 12 27.0	−39 54 58.0	7.5	−11.9	4.6
$C_{E.....}$	17 13 01.3	−39 53 35.2	1.1	−9.1	1.6	10	17 12 57.4	−39 53 42.3	3.7	−8.8	1.4
D.....	17 11 28.0	−39 30 37.6	4.0	−11.1	4.8	292	17 11 32.5	−39 30 03.9	3.3	−9.3	4.8
$D_{W.....}$	17 11 01.3	−39 34 17.6	2.3	2.4	3.3	137	17 11 34.3	−39 32 31.2	3.1	−1.1	6.0
E.....	17 11 29.1	−39 50 38.5	2.0	−6.1	7.2	159	17 11 55.4	−39 51 07.2	2.0	−6.0	5.0
G.....	17 10 55.6	−39 45 55.2	3.3	−10.8	8.0	307	17 10 56.3	−39 45 20.6	2.8	−11.5	4.8
$G_{E.....}$	17 11 27.1	−39 47 49.6	5.4	−12.8	2.6	168	17 11 21.0	−39 47 24.4	4.3	−12.3	2.7
I.....	17 12 08.2	−39 43 43.3	1.8	−9.9	5.4	103	17 12 16.6	−39 43 22.8	1.3	−10.4	5.9
L.....	17 12 25.8	−39 28 53.4	4.0	−12.0	5.7	370	17 12 30.2	−39 28 14.6	3.2	−11.7	6.0
O.....	17 13 46.7	−39 27 49.8	1.1	−6.4	4.9	61	17 13 46.0	−39 26 28.6	1.2	−4.6	4.7
$O_{b.....}$	17 13 46.7	−39 27 49.8	1.9	1.1	3.4	80	17 13 46.0	−39 26 28.6	1.9	1.0	3.8
$O_{SW.....}$	17 13 24.8	−39 37 08.6	2.8	−1.6	2.0	60	17 13 08.9	−39 36 43.2	3.5	−1.3	1.3

(continued)

Table 2.3 (continued)

Name (1)	^{12}CO(J = 1–0)						^{12}CO(J = 2–1)				
	α_{J2000} (^{hms}) (2)	δ_{J2000} ($^{\circ\prime\prime\prime}$) (3)	T_{R^*} (K) (4)	V_{peak} (km s^{-1}) (5)	ΔV_{LSR} (km s^{-1}) (6)	Mass ($M_\odot$) (7)	α_{J2000} (^{hms}) (8)	δ_{J2000} ($^{\circ\prime\prime\prime}$) (9)	T_{R^*} (K) (10)	V_{peak} (km s^{-1}) (11)	ΔV_{LSR} (km s^{-1}) (12)
Q.....	17 15 13.4	−39 25 06.2	2.9	−2.8	3.2	108	17 15 11.7	−39 26 47.4	2.8	−2.2	2.8
Q$_{W.....}$	17 14 49.3	−39 31 35.1	3.0	−14.3	2.4	46	17 14 53.0	−39 31 30.7	3.7	−14.1	1.8
R.....	17 15 39.9	−39 38 34.6	4.1	−3.3	2.4	67	17 15 32.0	−39 39 28.5	3.2	−3.1	2.2
U.....	17 14 34.2	−40 06 27.0	3.7	−4.8	1.3	58	17 14 13.4	−40 06 25.2	3.0	−4.6	1.3
W.....	17 13 42.8	−40 16 40.7	5.0	−5.1	3.0	402	17 13 30.0	−40 15 03.6	3.3	−4.9	3.4
Z.....	17 14 18.7	−39 56 55.1	2.6	−20.1	2.7	72	17 13 53.3	−39 54 46.8	2.9	−19.8	2.9
Z$_{NW....}$	17 13 45.0	−39 52 14.9	3.0	−19.8	2.6	36	17 13 45.6	−39 51 09.2	5.1	−19.8	1.8
Z$_{NE.....}$	17 14 57.4	−39 49 59.3	2.2	−20.0	3.3	31	17 14 53.3	−39 49 25.7	3.6	−19.6	2.5

Notes Col. (1): Clump name. Cols. (2–7) and (8–12): Observed properties of the ^{12}CO(J = 1–0, 2–1) spectra obtained at the peak positions of the CO clumps. Cols. (2)–(3): Position of the peak CO intensity. Col. (4): Peak radiation temperature T_{R^*}. Col. (5): V_{peak} derived from a single Gaussian fitting. Col. (6): FWHM line width ΔV_{LSR}. Col. (7): Total mass of the clumps derived using the relation between the molecular hydrogen column density $N(H_2)$ and the ^{12}CO(J = 1–0) intensity $W(^{12}CO)$, $N(H_2) = 2.0 \times 10^{20}[W(^{12}CO)$ (K km s^{-1})] (cm^{-2}) (Bertsch et al. 1993). See the text for more details. Cols. (8–12): The observed properties, same as Cols. (2–6) for the ^{12}CO(J = 2–1) spectra. The properties of A–E, G, I–O, and Q–W derived from ^{12}CO(J = 1–0) are shown by Moriguchi et al. (2005)

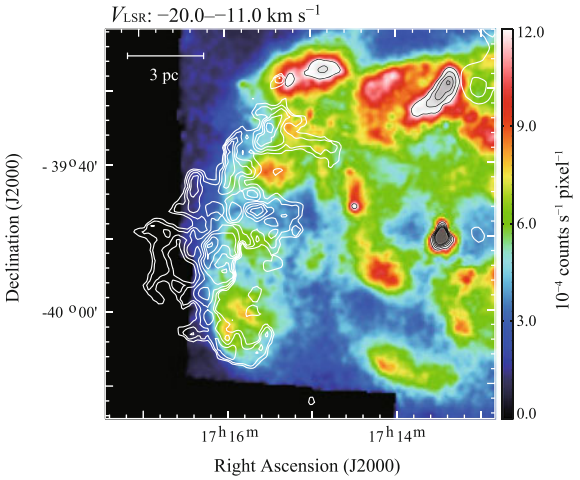

Fig. 2.4 Same XIS mosaic image (1–5 keV) as Fig. 2.2c toward the SE rim. The *white* contours indicate the distribution of HI proton column density (self-absorption corrected; see Sect. 3.2.3.3). The lowest contour level and the contour interval in HI proton column density are 2.0 and 0.1 × 10^{21} cm^{-2}, respectively. The velocity range is −20.0 to −11.0 km s^{-1}

Figure 2.4 shows an enlarged view in the SE rim overlaid with the HI proton column density contours with an integration range of −20.0 to −11.0 km s^{-1}. We applied HI self-absorption by following the analysis in Sect. 3.2.3.3. The lowest contour level and the contour interval in the HI proton column density are 2.0 × 10^{21} cm^{-2} and 0.1 × 10^{21} cm^{-2}, respectively. It is remarkable that the HI distribution corrected for the self-absorption is complementary to the X-ray peaks in the low-photon-count region in the SE rim.

2.2.2 *Detailed Comparison with X-Ray Data*

We here make a detailed comparison of the spatial distributions of the CO/HI clumps with those in the X-ray images in terms of radial and azimuthal distributions.

In Fig. 2.5, the left and middle panels of each row show images of the CO integrated intensity overlaid onto the distributions of soft band (1–5 keV, left) and hard band (5–10 keV, middle) X-rays. The crosses in each image indicate the centers of gravity of the CO clumps listed in Table 2.4, which are somewhat different from the peak positions listed in Table 2.2, and each arrow indicates the direction of the center of the SNR. The dashed white circles represent radii 0.°06 and 0.°12 of the center of gravity. We see a trend wherein X-ray intensity is enhanced toward the CO clumps, although the CO peaks generally show offsets from the X-ray peaks. In the right panels of Fig. 2.5, we plot radial profiles of the CO integrated intensity and X-ray counts averaged at each radius for the 1–5 and 5–10 keV bands. To quantitatively characterize the radial distribution, we first identify the peak in the 1–5 keV radial distribution. In addition, we defined the separation between the center of gravity of the CO clumps and that of the X-ray peaks in the radial distribution. Ten of the 17

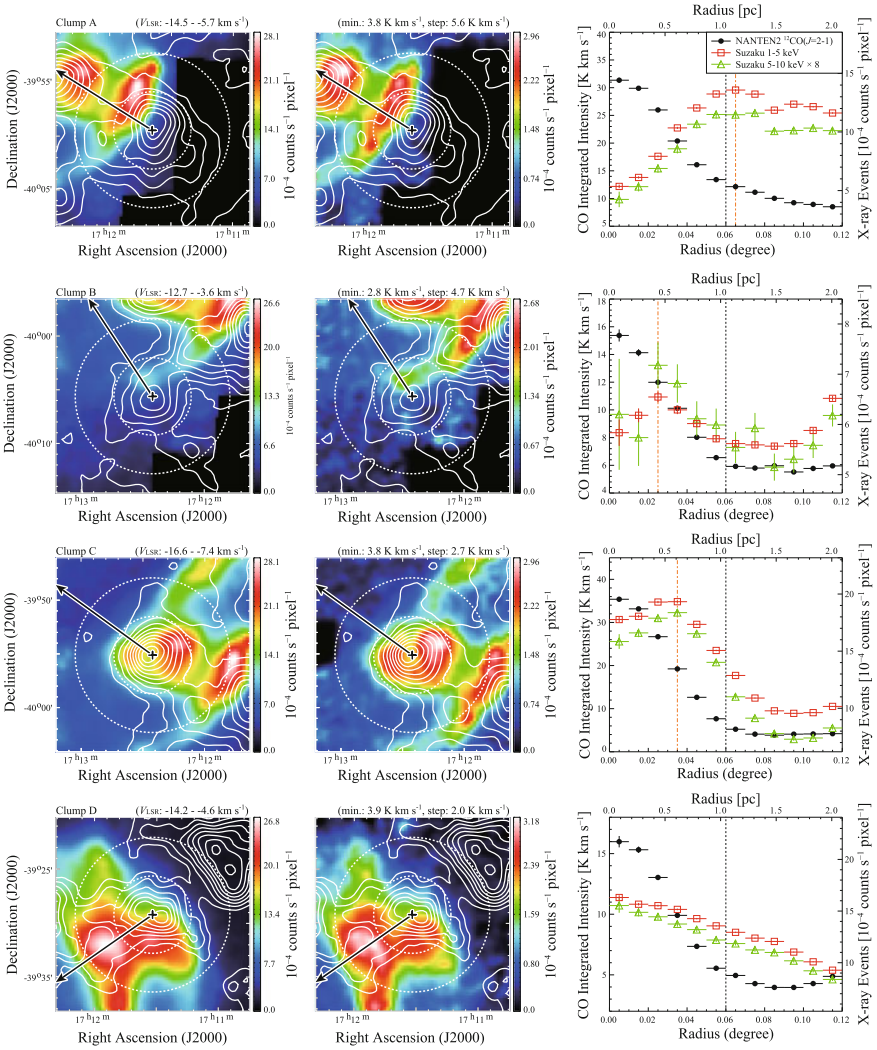

Fig. 2.5 Distribution of ^{12}CO($J=$ 2–1) emission (*white contours*) superimposed on the *Suzaku* 1–5 keV (*left*) and 5–10 keV (*middle*) images. Velocity range in integration and contour levels are shown in the *top of left* and *middle panels*, respectively. Each *arrow* indicates the direction of the center of the SNR. The crosses show the position of the center of gravity for each CO clump (see also Table 2.4). The *dashed white circles* represent radii 0.°06 and 0.°12 of the center of gravity for each CO clump. *Right panels* show the radial profiles around each molecular clump in the ^{12}CO(J=2–1) integrated intensity and the two *Suzaku* energy bands (1–5 keV and 5–10 keV, in units of 10^{-4} counts s^{-1} pixel^{-1}) in Fig. 2.2. The radial profiles from the 5–10 keV band have been scaled such that they has the same area as the 1–5 keV profiles (scaled by a factor 8), for the sake of direct comparison. The *orange dash-dotted lines* indicate X-ray peak radius in the 1–5 keV energy band

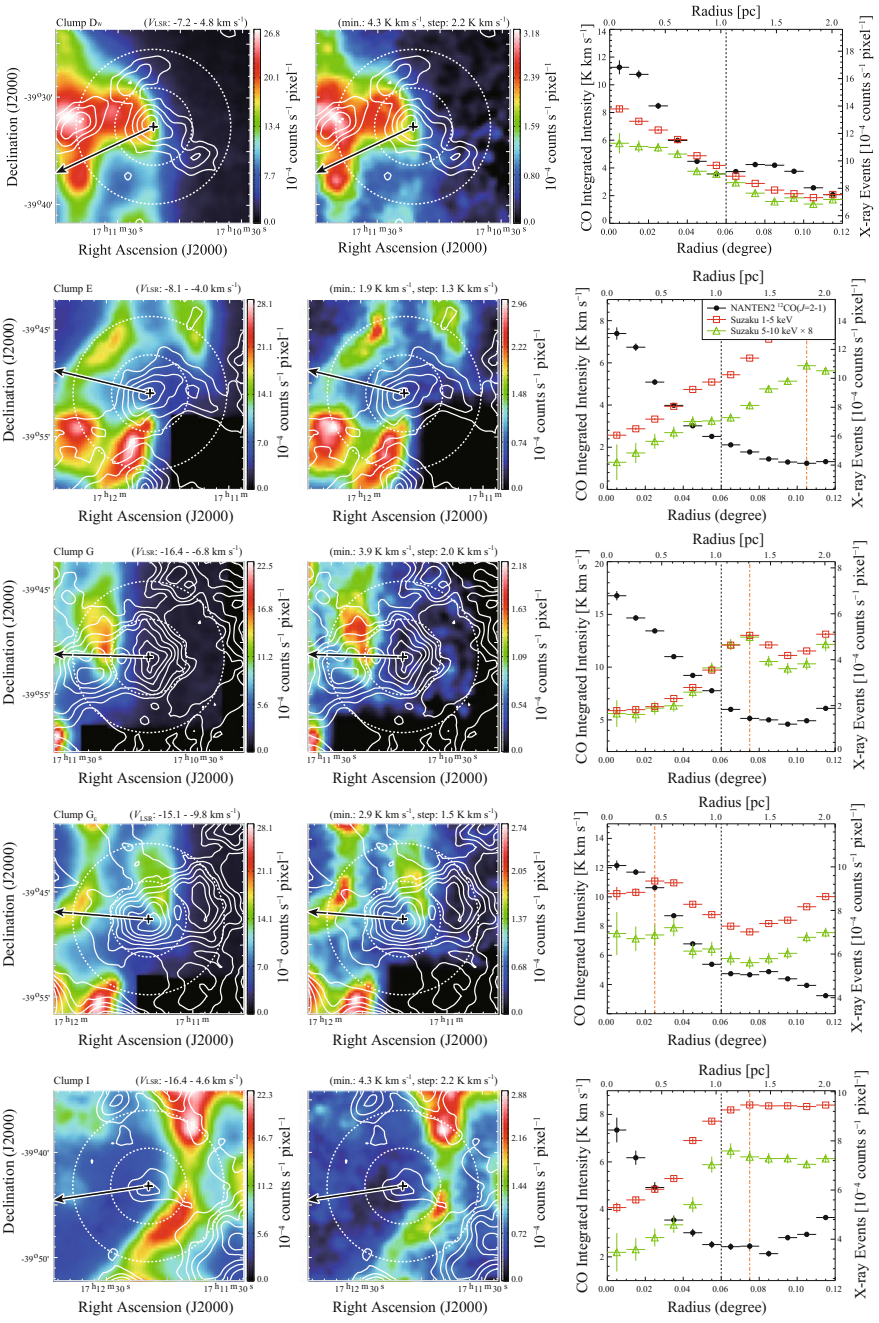

Fig. 2.5 (continued)

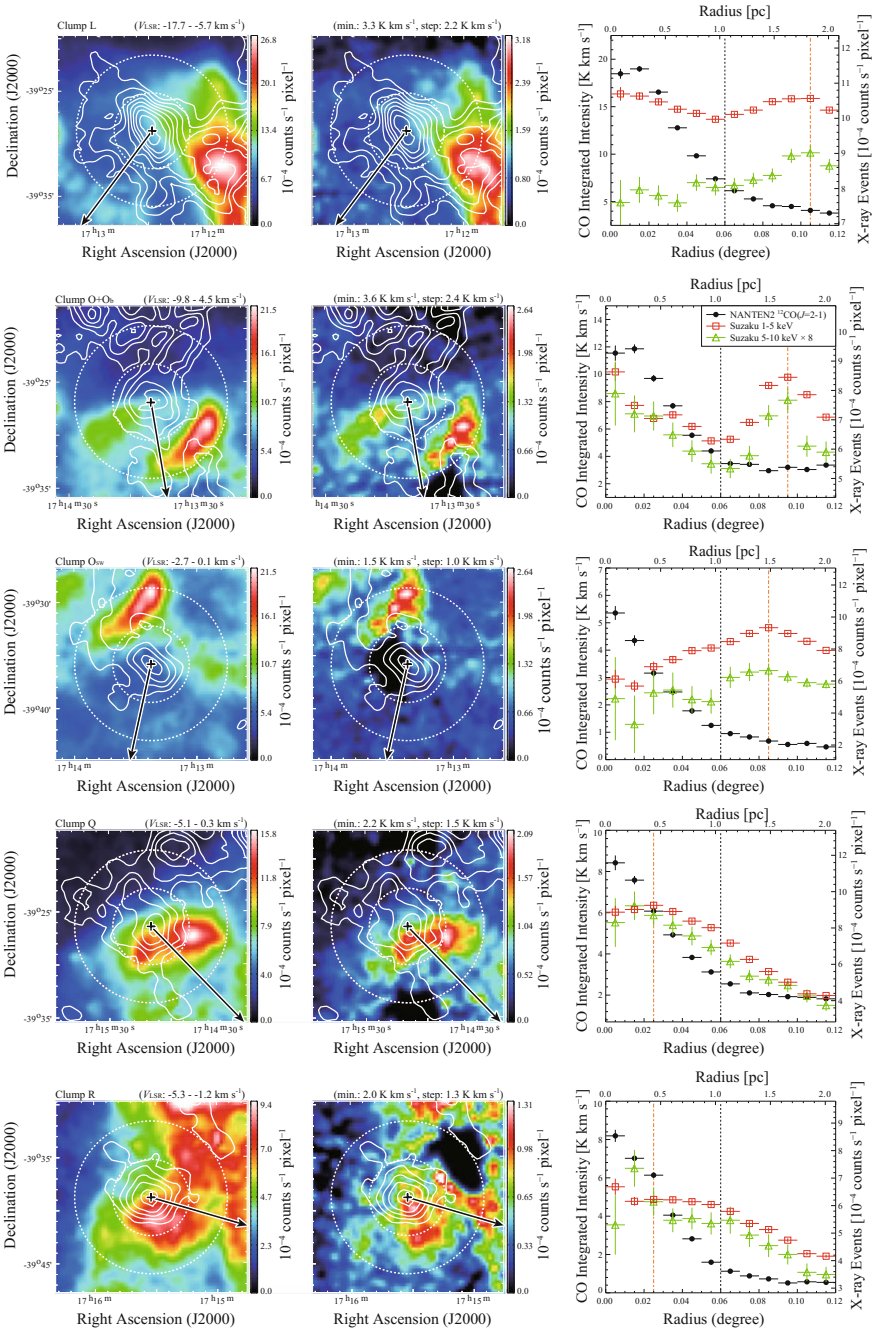

Fig. 2.5 (continued)

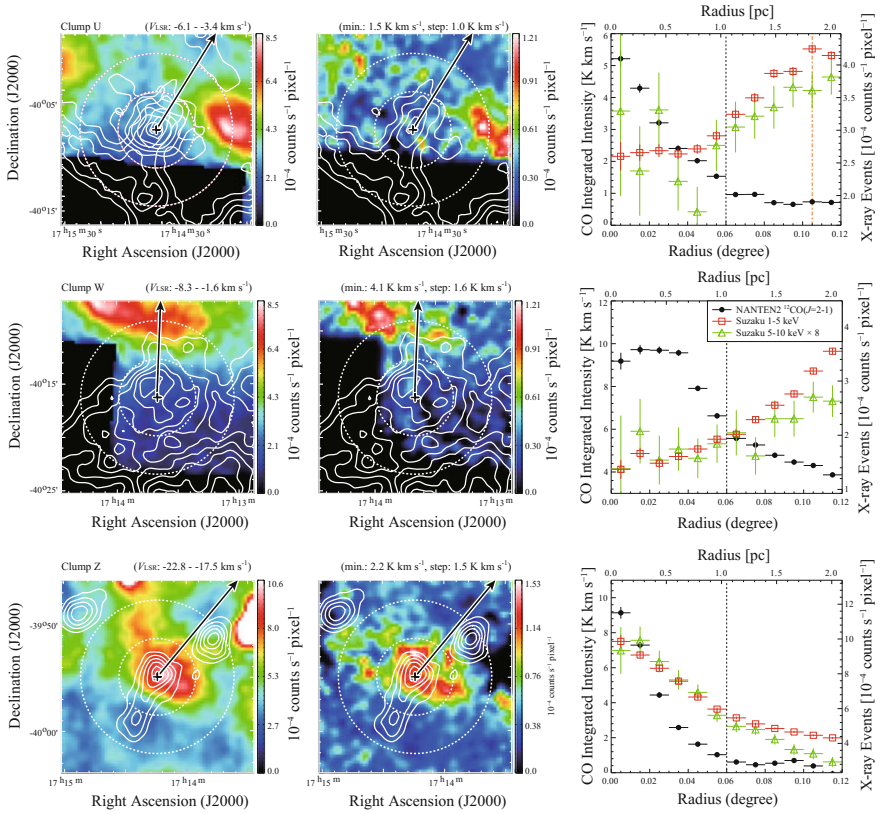

Fig. 2.5 (continued)

Table 2.4 Results of radial and azimuthal distribution

Name (1)	α_{J2000} (^{h} ^{m} ^{s}) (2)	δ_{J2000} ($^\circ$ $'$ $''$) (3)	V_{LSR} (km s^{-1}) (4)	Radius (degree) (5)	Separation (degree) (6)	Peak Intensity ($\times 10^{-4}$ counts s^{-1} pixel) (7)	Angle (Fraction) (degree), (%) (8)	Interacting Mass ($M_\odot$) (9)
A.....	17 11 39.1	−39 59 22.2	−14.5–−5.7	0.050	0.065	18.50 ± 0.07	−120–+120, (67)	460 ± 60
B.....	17 12 25.3	−40 05 37.5	−12.7–−3.6	0.050	0.025	10.88 ± 0.05	−150–+90, (67)	130 ± 20
C.....	17 12 25.3	−39 55 07.4	−16.6–−7.4	0.040	0.035	19.64 ± 0.07	−180–+180, (100)	400 ± 30
D.....	17 11 31.9	−39 29 13.6	−14.2–−4.6	0.040	···	22.25 ± 0.07	−150–+150, (83)	240 ± 20
Dw.....	17 11 12.8	−39 32 43.5	−7.2–4.8	0.040	···	21.18 ± 0.07	−120–+90, (58)	80 ± 11
E.....	17 11 38.7	−39 50 56.8	−8.1–−4.0	0.040	0.105	19.81 ± 0.07	−180–+180, (100)	159 ± 13
G.....	17 10 54.5	−39 46 25.7	−16.4–−6.8	0.050	0.075	11.81 ± 0.09	−60–+60, (33)	100 ± 30
GE.....	17 11 22.2	−39 47 34.0	−15.1–−9.8	0.050	0.025	13.16 ± 0.13	−150–+150, (83)	140 ± 14
I.....	17 12 09.3	−39 43 11.9	−16.4–−4.6	0.030	0.075	14.22 ± 0.07	−180–+180, (100)	103 ±9
L.....	17 12 28.2	−39 28 45.9	−17.7–−5.7	0.045	0.105	19.91 ± 0.07	−180–+180, (100)	370 ± 30
O.....	17 13 48.9	−39 26 24.9	−11.3–−1.6	0.055	0.095	14.02 ± 0.14	−120–+120, (67)	41 ±5
Ob.....	17 13 46.9	−39 26 45.9	−4.6–2.2	0.035	0.085	13.92 ± 0.14	−120–+120, (67)	53 ±7

(continued)

Table 2.4 (continued)

Name (1)	α_{J2000} (^{h} ^{m} ^{s}) (2)	δ_{J2000} ($^\circ$ $'$ $''$) (3)	V_{LSR} (km s^{-1}) (4)	Radius (degree) (5)	Separation (degree) (6)	Peak Intensity ($\times 10^{-4}$ counts s^{-1} pixel) (7)	Angle (Fraction) (degree), (%) (8)	Interacting Mass ($M_\odot$) (9)
Osw.....	17 13 22.4	−39 35 50.6	−2.7–0.1	0.030	0.085	14.5± 0.2	−180–+180, (100)	60 ±5
Q.....	17 15 09.6	−39 38 48.7	−5.1–0.3	0.040	0.025	10.83 ± 0.12	−150–+120, (75)	81 ±9
R.....	17 15 32.4	−39 39 28.5	−5.3–−1.2	0.035	0.025	6.7± 0.2	−150–+150, (83)	56 ±6
U.....	17 14 44.5	−40 07 24.4	−6.1–−3.4	0.030	0.105	5.54 ± 0.07	−90–0, (25)	15 ±5
W.....	17 13 40.2	−40 16 16.9	−8.3–−1.6	0.080	···	4.58 ± 0.07	−30–+30, (17)	70 ± 30
Z.....	17 14 14.3	−39 54 55.7	−22.8–−17.5	0.025	···	3.60 ± 0.06	−150–+180, (92)	66 ±6
HI SE rim.....	17 16 09.3	−40 03 10.6	−20.0–−11.0	···	···	6.97 ± 0.09	−90–+60, (42)	56 ± 11
O+Ob.....	17 13 49.7	−39 26 54.9	−9.8–4.5	0.040	0.095	14.03 ± 0.14	−120–+120, (67)	94 ±8
D+Dw.....	···	···	···	···	···	21.72 ± 0.05	···	320 ± 30
O+Ob+Osw.	···	···	···	···	···	14.19 ± 0.09	···	154 ± 10
G+GE.....	···	···	···	···	···	12.49 ± 0.08	···	240 ± 30
E+I.....	···	···	···	···	···	17.02 ± 0.05	···	260 ± 20

Notes Col. (1): Clump name. Cols. (2)–(3): Position of the center of gravity with the ^{12}CO(J = 2–1) integrated intensity (except for the SE rim). Cols. (4): Integration range of velocity for the estimation of the ^{12}CO(J = 2–1) or HI. (5): Radius of a CO clump defined as the radial distance from the center of gravity of the clump to the point where the intensity is at half maximum. (6) Separation of the X-ray peak from the center of gravity of each CO/HI clump. (7) X-ray peak intensity with the statistical error around each clump shown in Fig. 2.8. (8) Azimuth angle range of the X-rays (1–5 keV) above the background level estimated in Appendix A (see also Sect. 2.2.1). (9) Interacting clump mass defined as the total CO/HI mass within the azimuth angle range of the X-rays (1–5 keV) for each clump.

clumps have X-ray peaks and positive X-ray slopes inside the peak in Fig. 2.5. Clump W has no peak and shows a clear positive X-ray slope. On the other hand, four of the CO clumps show negative slopes and the other shows a nearly flat slope. As the radial distributions of the X-ray peaks are generally smooth and monotonic, linear approximation is reasonable for estimating intensity gradients. Only the CO clumps O+O$_b$ show a complicated, non-monotonic radial distribution of X-ray peaks, which may be caused by a blending of the two velocity components. We made least-squares fits to the X-ray peak distributions using a straight line for simplicity for the 10 clumps within the peak, and for clump W and the other six clumps within a radius of 0.°06. The respective slope values are listed in Table 2.5 and are shown as a histogram in Fig. 2.6. Twelve of the 16 clumps (75%) show positive slopes, indicating that the X-rays show a decrease toward the CO clump and are brighter in the neighborhood of the clump. With the exception of clump Z, the four clumps with negative or flat slopes also show a clear relative enhancement of X-rays in their vicinities (in Fig. 2.5 left and middle panels). Clump Z has no clear X-ray depression toward the center, whereas enhanced X-rays are seen in its surroundings (Fig. 2.5 left and middle panels

Table 2.5 Fitting results of the X-rays radial distribution

Name (1)	Fitting range (degree) (2)	Slope ($\times 10^{-4}$ counts s^{-1} pixel degree^{-1}) (3)	Comments (4)
A.....	0.00–0.07	+152 ±2	Positive slope with peak
B.....	0.00–0.03	+40 ±10	Positive slope with peak
C.....	0.00–0.04	+56 ±6	Positive slope with peak
D.....	0.00–0.06	−59 ±2	Negative slope
Dw.....	0.00–0.06	−84 ±3	Negative slope
E.....	0.00–0.11	+82 ±1	Positive slope with peak
G.....	0.00–0.08	+57 ±1	Positive slope with peak
GE.....	0.00–0.03	+40 ± 20	Positive slope with peak
I.....	0.00–0.08	+70 ±2	Positive slope with peak
L.....	0.00–0.10	+2 ±1	Flat
O+Ob.....	...	...	...
Osw.....	0.00–0.09	+43 ±3	Positive slope with peak
Q.....	0.00–0.03	+20 ± 20	Positive slope with peak
R.....	0.00–0.03	−10 ± 10	negative slope
U.....	0.00–0.10	+19 ±1	Positive slope with peak
W.....	0.00–0.06	+10 ±2	Positive slope with no peak
Z.....	0.00–0.06	−79 ±4	Negative slope

Notes Col. (1): Clump name. Col. (2): Fitting range of X-rays in radial plot (see also the text for details). Col. (3): Slope of least-squared fitted straight line of X-rays with 1 sigma error. (4) Comments.

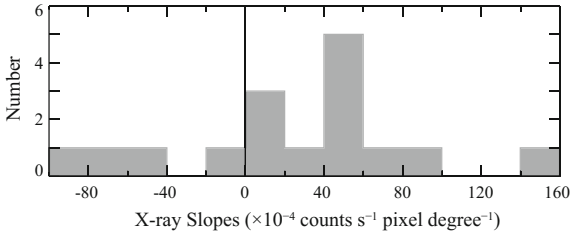

Fig. 2.6 Histogram of the X-ray slope estimated by linear fitting to the radial profile for each CO clump. The fitting ranges and results are shown in Table 2.5

in the last low). We conclude that the enhancement of X-rays around a clump are a general trend among the CO clumps. We note that, on average, each CO clump has a radius of $0.^{\circ}04 \pm 0.^{\circ}01$ and that X-ray peaks are distributed with a separation $0.^{\circ}07 \pm 0.^{\circ}03$ from the center of each clump (see also Table 2.4).

We performed a similar analysis of the cold HI in the SE rim. The HI distribution estimated from self-absorption clearly delineates the outer boundary of the X-rays (Fig. 2.7) and the relative distributions are similar to those for clump A. The HI column density distribution is fairly flat and has no clear peak. Thus, instead of using the HI peak, we draw a line passing through the center of the SNR and the soft X-ray peak, and then, we define the HI column density peak on the line. The radial distributions are plotted centered on this HI peak. We find a trend similar to that of the CO clumps wherein the X-rays are clearly enhanced around the cold HI.

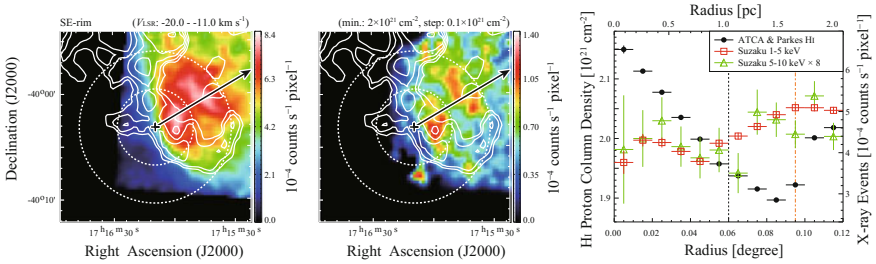

Fig. 2.7 Distribution of the cold HI column density (*white contours*) superimposed on the *Suzaku* images in the 1–5 (*left*) and 5–10 keV (*middle*) bands. Velocity range of integration and contour levels are shown in the *top of the left* and *middle panels*, respectively. Each *arrow* indicates the direction of the center of the SNR passing through the X-ray peak in the 1–5 keV image. The *crosses* show the position representing the cold HI clump and is determined as the crossing point of the HI cloud with the arrow, $(\alpha_{J2000}, \delta_{J2000}) = (17^{h}\ 16^{m}\ 9.3^{s}, -40^{\circ}\ 3'\ 10.6'')$ (also see the text). The *dashed white circles* represent radii of $0.^{\circ}06$ and $0.^{\circ}12$ centered on the crosses. *Right panel* shows the radial profile around the crosses in the HI column density and the X-ray counts in the two energy bands (1–5 and 5–10 keV) in Fig. 2.2. The radial profile in the 5–10 keV band is scaled by a factor of 8 relative to the 1–5 keV band for the sake of direct comparison. The *orange dash-dotted line* indicates the X-ray peak radius in the 1–5 keV band

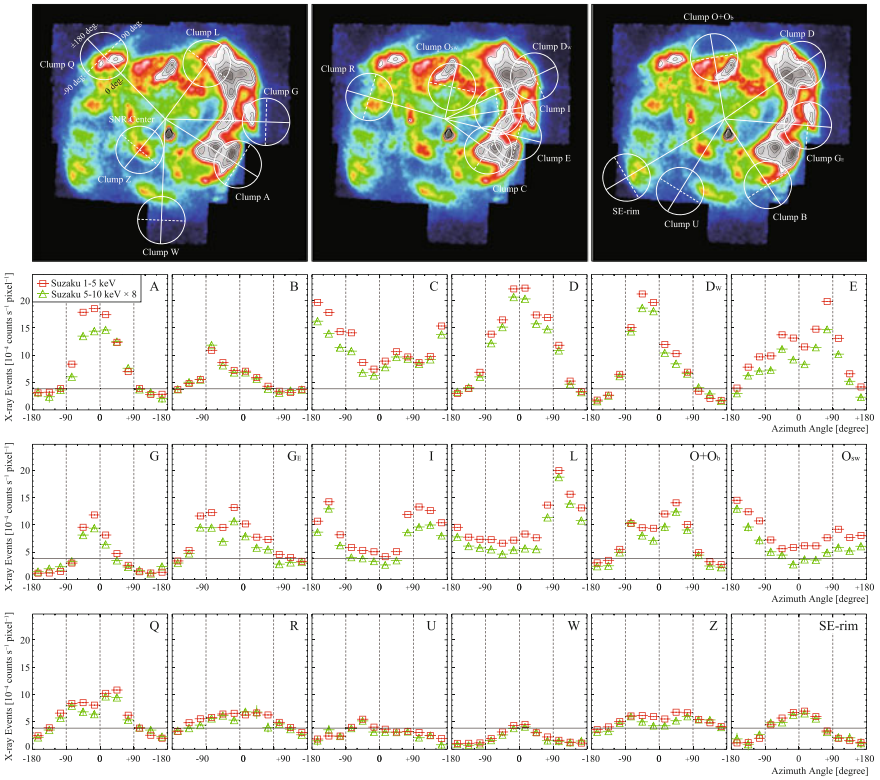

Fig. 2.8 *Top panels* Same XIS mosaic image (1–5 keV) as in Fig. 2.2c. Overlaid *white circles* are centered on the center of gravity of each CO/HI clump. The azimuthal distribution of X-rays is averaged within each circle (radius = 0.°12). Each *white* solid straight line connects the centers of the circle and the SNR and each *dashed white line* in the circle is vertical to the solid line. The azimuthal angle is measured using the solid line as the origin counterclockwise from −180° to 180° (e.g., clump Q in *top panel*). *Other panels* Azimuthal distributions of *Suzaku* XIS 1–5 keV (*red square*) and 5–10 keV (*green triangles* are scaled by a factor of eight) averaged in the circles for each clump. The *horizontal solid lines* indicate the background level of the X-rays estimated inside the SNR for the 1–5 keV energy band (see the text)

In Fig. 2.8, the top three panels show the same XIS mosaic images (1–5 keV) as those in Fig. 2.2c. The lines connecting the CO/HI clump positions (shown in Figs. 2.5 and 2.7 and in Table 2.4) and the center of the SNR $(l, b) = (347.^{\circ}3, -0.^{\circ}5)$ or $(\alpha_{J2000}, \delta_{J2000}) = (17^{h}\ 13^{m}\ 34^{s}, -39^{\circ}\ 48'\ 17'')$ are taken as the origins of the azimuth angle, which is measured counterclockwise. The azimuthal angular distribution of the X-rays around each CO/HI clump is estimated with respect to the direction of the center of the SNR. We measured the azimuthal angular extent of the X-rays in each clump in the 1–5 keV band image by adopting the background level inside the SNR as the threshold (Sect. 2.2.1). The results are shown in Fig. 2.8 and Table 2.4. The upper panel of Fig. 2.9 shows the range of angles and the lower panel shows a

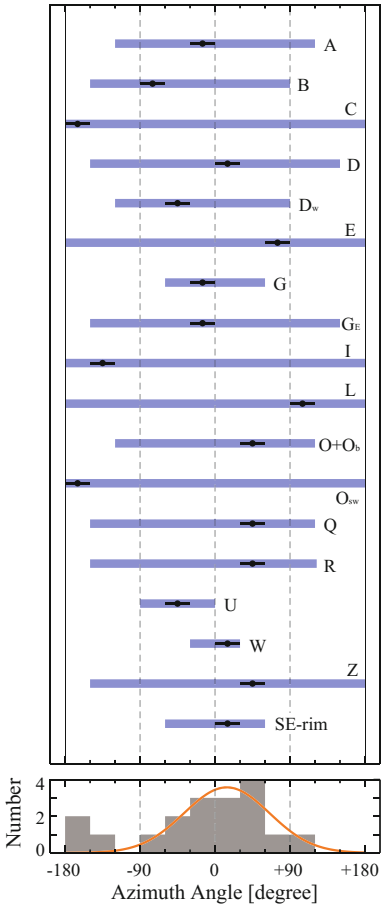

Fig. 2.9 The azimuthal angular extent of the X-rays above the background level in each CO/HI clump for the 1–5 keV band image (*top panel*; see also Table 3). Each *black dot* indicates the angle of X-ray peak intensities in Fig. 2.8. The histogram of the X-ray peak positions is shown in the *lowest panel*. The *red curve* indicates the fitting result by a Gaussian function for the clumps from $-90°$ to $+120°$

histogram of the peak angles. The five clumps inside the SNR, clumps C, E, I, L, and O_{SW}, are fully surrounded by the X-rays, which show a peak toward the azimuthal angle of $-180°$ to $-120°$ (clumps C, I, and O_{SW}) or $+60°$ to $+120°$ (clumps E and L). These distributions indicate that the clumps inside the SNR are surrounded by enhanced X-rays, whereas those on the border of the SNR have enhanced X-rays only toward the center of the SNR. In Fig. 2.9, lower panel, we see a trend that the X-ray intensity is enhanced at an azimuthal angle of around $0°$ and scattering is high, $\pm 60°$ (clumps A, D, D_W, G, G_E, O+O_b, Q, R, U, W, Z, and SE rim). The histogram was fitted by a Gaussian function from $-120°$ to $120°$, and we find that the best-fit parameters of center and sigma are $14° \pm 5°$ and $51° \pm 5°$, respectively.

2.2.3 Sub-Millimeter Results; $^{12}CO(J = 4–3)$ Distribution

We observed the $^{12}CO(J = 4–3)$ transition in a region of $3'.0 \times 3'.0$ in equatorial coordinates around clump C and toward the peak position of Clump A. Figure 2.10 shows four images of clump C in the $^{12}CO(J = 2–1, 3–2,$ and $4–3)$ and $^{13}CO(J = 2–1)$ transitions, where the $^{12}CO(J = 3–2)$ distribution is taken from

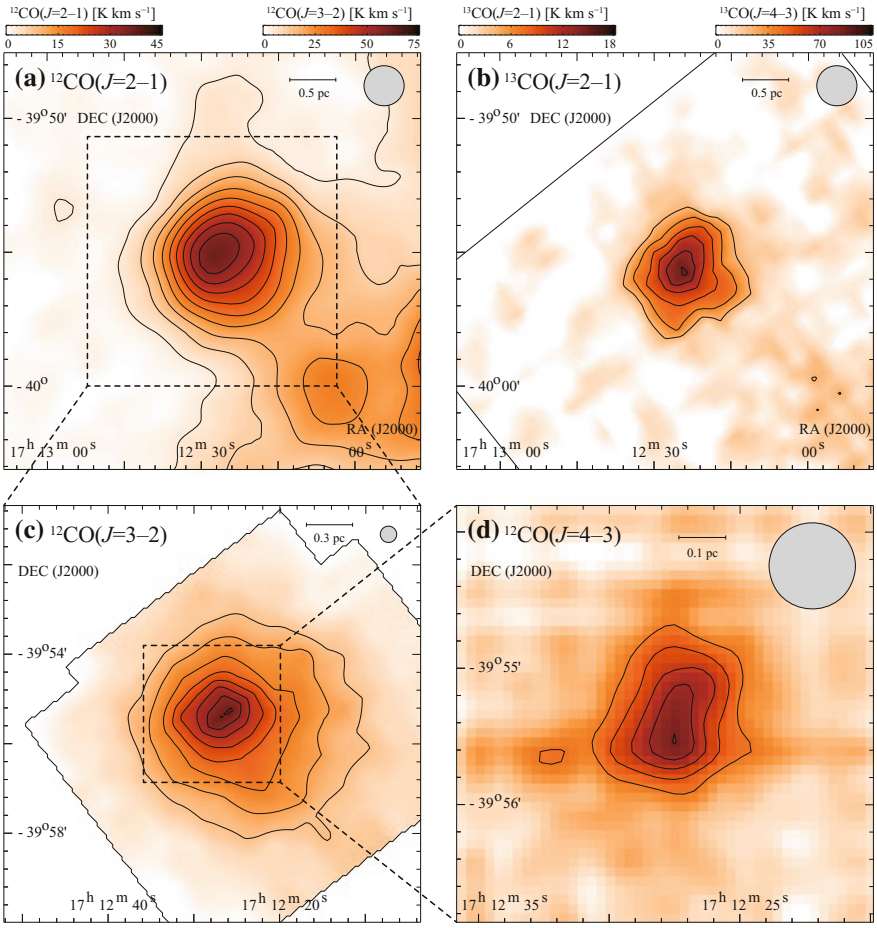

Fig. 2.10 Intensity distributions of the $^{12}CO(J = 4–3, 3–2, 2–1)$ and $^{13}CO(J = 2–1)$ transitions of clump C. The velocity range is from -30 to 7 km s^{-1} in (**d**); from -20 to -7 km s^{-1} in (**c**); from -16.6 to -7.3 km s^{-1} in (**a**); and from -16 to -8 km s^{-1} in (**b**). The CO contours are every 10.2 K km s^{-1}($\sim 3.0\sigma$) from 41.6 K km s^{-1}($\sim 12.2\sigma$) in (**d**); every 5.0 K km s^{-1} ($\sim 5.3\sigma$) from 30.2 K km s^{-1} ($\sim 31.8\sigma$) in (**c**); every 3.8 K km s^{-1} ($\sim 4\sigma$) from 2.7 K km s^{-1} ($\sim 3\sigma$) in (**a**); and every 1.8 K km s^{-1}($\sim 2.6\sigma$) from 7.28 K km s^{-1} ($\sim 10.6\sigma$) in (**d**). The lowest contours are half of the peak intensity value for each emission, except for (**a**). The open cross shows the positions of the *IRAS* point source (see Table 2.6)

(Moriguchi et al. 2005). The ^{12}CO($J = 4$–3) core is the most compact and its size increases toward the lower J transitions, suggesting a sharp intensity decrease with radius since the higher J transitions have higher critical densities for collisional excitation.

2.2.4 ^{12}CO($J = 4$–3) Broad Wings

Figure 2.11 shows that the broad ^{12}CO($J = 4$–3) wings first detected by Fukui et al. (2003) reveal a clear bipolar signature centered on *IRAS* 17089−3951 (Table 2.6) and on the peak position of the dense cloud core in clump C. This bipolarity verifies that the wings are driven by a protostar and not by the SNR shock waves. The *IRAS* source position also shows a good correlation with an extended *Spitzer* sources at 8.28 μm (from IPAC Infrared Science Archive; Fig. 2.11a). In addition to the ^{12}CO($J = 1$–0) and ^{12}CO($J = 3$–2) transitions, wings toward clump C are also seen in the current ^{12}CO($J = 2$–1) data (Moriguchi et al. 2005), although the wing intensities of these lower-J transitions are more than a few times weaker than the ^{12}CO($J = 4$–3) wings. It is not clear if clumps A and D show signs of bipolar outflow in either the ^{12}CO($J = 1$–0) and ^{12}CO($J = 3$–2) data (Moriguchi et al. 2005) or in the current ^{12}CO($J = 2$–1) data. We also find that the distribution of wing-like components is complementary to the X-ray intensity around clump C. Figure 2.12 shows two overlays of

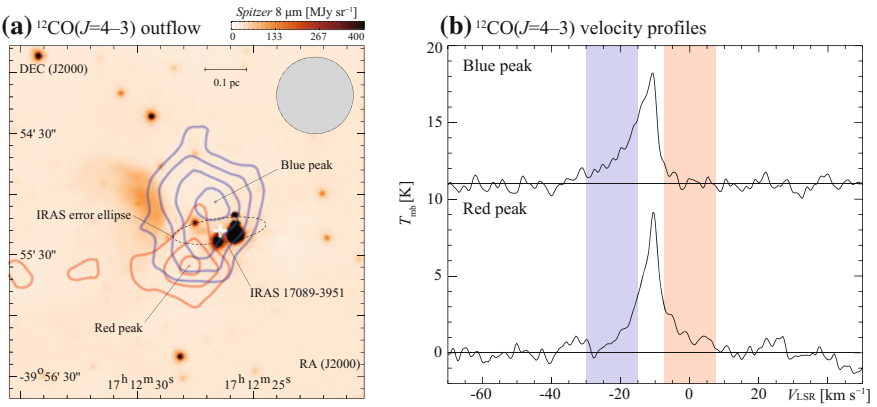

Fig. 2.11 **a** Overlay map RX J1713.7−3946 *Spitzer* 8μm image in color scale (from GRIMPS Archive) and ^{12}CO($J = 4$–3) intensity contours taken by NANTEN2. The *blue* contours are from −30 to −15 km s^{-1} and the *red* contours from −8 to 7 km s^{-1}. The lowest contour level of the *red* and *blue* contours are 9.6 K km s^{-1} (∼4σ) for each. The contour interval of the *black* contour is 10.2 K km s^{-1} (∼3σ), whereas that of the others is 4.8 K km s^{-1} (∼2σ). Open cross and enclosed *black dashed circle* show the positions of the *IRAS* point source (see Table 2.6) and the 90% confidence region, respectively. (b) ^{12}CO($J = 4$–3) spectra covering a velocity range from −70 to 50 km s^{-1}. Areas *shaded blue* and *red* correspond to the respective color contours in (**a**)

Table 2.6 Properties of *IRAS* point sources

Clump name (1)	*IRAS* point sources (2)	l (deg) (3)	b (deg) (4)	α(J2000) (^{hms}) (5)	δ(J2000) ($^{\circ\prime\prime\prime}$) (6)	semimajor $^{\prime}$ (7)	semiminor $^{\prime}$ (8)	Posang deg. (9)	F_{12} (Jy) (10)	F_{25} (Jy) (11)	F_{60} (Jy) (12)	F_{100} (Jy) (13)	L_{IRAS} ($L_{\odot}$) (14)
A	17082−3955	346.94	−0.31	17 11 41.04	−39 59 11.21	23	5	98	5.4	3.8	17.5	138	137
C	17089−3951	347.08	−0.39	17 12 26.46	−39 55 17.98	23	6	98	4.4	13.0	98.5	234	311
D	17079−3926	347.31	0.01	17 11 25.59	−39 29 53.29	39	6	98	2.0	20.0	88.6	739	562

Notes Cols. (1)–(2): Clump name (Moriguchi et al. 2005) and *IRAS* point source near the ^{12}CO($J = 3$–2) peaks. Cols. (3)–(6): Position of the *IRAS* sources. Cols. (7)–(9): Semimajor axis, semiminor axis, and position angle of the position error of the *IRAS* sources. Cols (10)–(13): Fluxes of 12, 25, 60, and 100 ¯m, respectively. Col. (14): *IRAS* luminosity estimated using the formula of Emerson (1988). Col. (18). (see Cols. (2)–(4) and (10)–(15) are Moriguchi et al. 2005 Table 3)

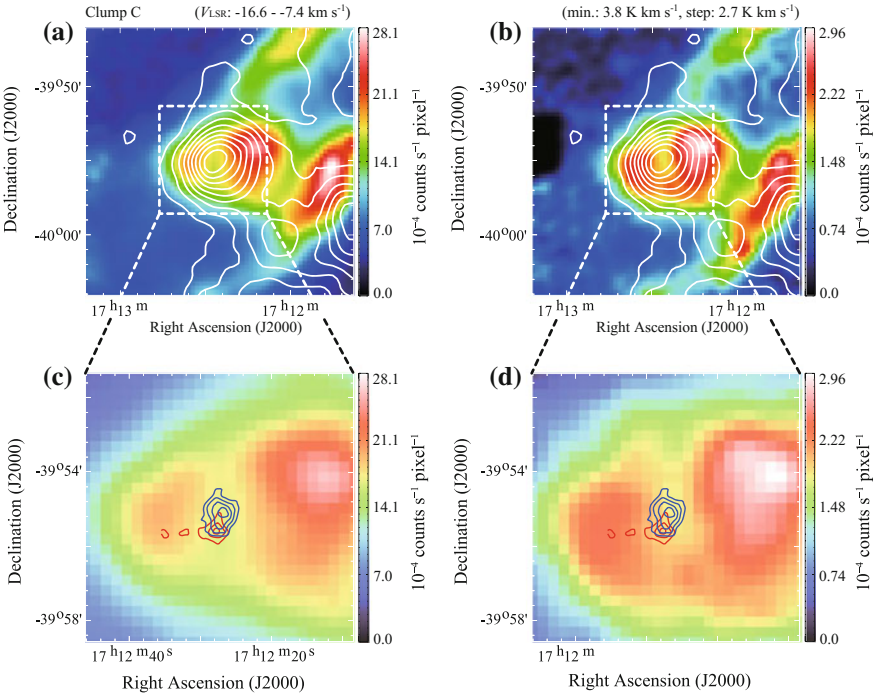

Fig. 2.12 Distribution of ^{12}CO($J = 2$–1) emission (*white contours*) superimposed on the *Suzaku* **a** 1–5 keV and **b** 5–10 keV images toward clump C. The velocity range and contour levels are the same as those in Fig. 2.5. **c** and **d** show the enlarged view of clump C overlaid with ^{12}CO($J = 4$–3) intensity contours. The contours are the same as those in Fig. 2.11a

^{12}CO($J = 4$–3) wing component and X-ray images in the 1–5 keV (Fig. 2.12a) and 5–10 keV (Fig. 2.12a) energy bands, respectively. Clump C is surrounded by bright X-ray emissions both on its east and west sides with a local minimum toward the center of the core (see also Fig. 2.5). Figure 2.12b shows a remarkable coincidence between the X-ray depression and the cloud core at a ∼0.1 pc scale. This depression is not caused by interstellar absorption, as we find a similar distribution of X-ray emissions in the higher energy band (5–10 keV) that are barely absorbed (see Appendix E). This morphology suggests that X-ray emissions are enhanced on the surface of the cloud core.

2.3 Analysis of Detailed Molecular Properties

2.3.1 LVG Analysis

We used the large velocity gradient (LVG) model of line radiation transfer to estimate density and temperature from the multi-J transitions of CO; i.e., ^{12}CO($J = 3$–2, 4–3) and ^{13}CO($J = 2$–1). We applied the LVG analysis (Goldreich and Kwan 1974; Scoville and Solomon 1974) to estimate the physical parameters of the molecular gas surrounding clumps A and C by adopting a spherically symmetric uniform model having a radial velocity gradient of dv/dr. The ^{12}CO($J = 2$–1) transition was not included in the analysis because this transition may be subject to self-absorption owing to low excitation foreground gas (e.g., Mizuno et al. 2010). We calculated level populations of ^{12}CO and ^{13}CO molecular rotational states and line intensities. The LVG model requires three independent parameters to calculate emission line intensities, i.e., kinetic temperature, density of molecular hydrogen, and $X/(dv/dr)$. $X/(dv/dr)$ is the abundance ratio between CO and H_2 divided by the velocity gradient in the cloud. Using the abundance ratio [^{12}CO]/[^{13}CO] $\sim$75 (Güsten and Philipp 2004) and [^{12}CO]/[H_2] $\sim 5\times10^{-5}$ (Blake et al. 1987), we estimated the mean velocity gradient between the peaks to be $\sim$12.5 km s^{-1} pc^{-1}. Accordingly, we adopted $X/(dv/dr) = 4.0\times10^{-6}$ (km s^{-1} pc^{-1})$^{-1}$ for ^{12}CO.

To solve for the temperatures and densities that reproduce the observed line intensity ratio, we calculated chi-square χ^2 as follows:

$$\chi^2 = \Sigma[(R_{\rm obs} - R_{\rm model})^2/\sigma] \tag{2.1}$$

where $R_{\rm obs}$ is the observed line intensity ratio between different excitation lines or isotopes, $R_{\rm model}$ is the line ratio of the LVG calculations, and σ is the standard deviation for $R_{\rm obs}$ used in the analysis. The error in the observed intensity was estimated based on the noise level of the observations and the calibration error. We assumed that an error of calibration from T_A^* to $T_{\rm MB}$ is 10% for all the line intensities. The data used were derived from the line profiles in Fig. 2.13 upper, and three ratios were estimated for a 1.5 km s^{-1} velocity interval in the three peaks, as listed in Table 2.7.

The lower panels of Fig. 2.13 show the results of fitting to the data obtained with a chi-square minimization approach to find the temperature and density solutions. Each locus of a black solid line surrounding a cross indicates the chi-square χ^2, which corresponds to the 95% confidence level of a chi-square distribution. The crosses denote the lowest point of the chi-square estimate. In addition, we are able to reject each region outside the black solid line at the 95% confidence level. Table 2.7 summarizes the results of the LVG analysis. Density and temperature are relatively well constrained in clumps A and C. The temperature of the clumps is in a range of 10–12 K, and density is somewhat higher in clump C, $\sim10^4$ cm^{-3}, than that in clump A, $\sim6\times10^3$ cm^{-3}.

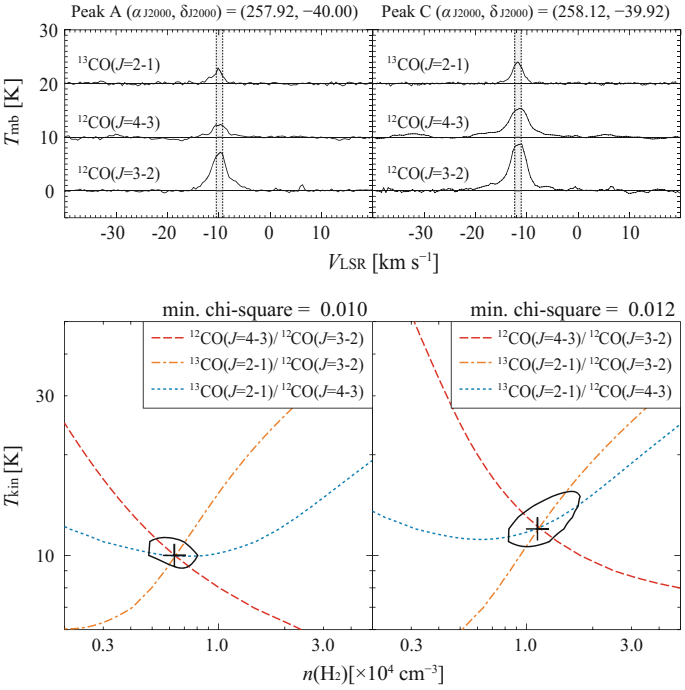

Fig. 2.13 Results of an LVG analysis for molecular clumps A and C. *Top* CO line profiles for each molecular peak are smoothed to 90″ by a Gaussian beam corresponding to the ^{13}CO($J = 2$–1) beam size. *Bottom* Results of an LVG analysis for molecular peaks as indicated by the *Top panels*. Each locus of a *black solid line* surrounding the cross indicates the chi-square χ^2 of 3.84, which corresponds to the 95% confidence level of a chi-square distribution with one degree of freedom. The crosses denote the lowest point of chi-square

Table 2.7 Results of LVG analysis at molecular clumps

Name (1)	α_{J2000} (2) (°)	δ_{J2000} (3) (°)	^{12}CO		^{13}CO	$n(H_2)$ (7) (10^4cm^{-3})	T_{kin} (K) (8)
			$J = 3$–2 (4) (K)	$J = 4$–3 (5) (K)	$J = 2$–1 (6) (K)		
A	257.92	−40.00	6.6	2.1	1.9	$0.6^{+0.2}_{-0.1}$	10^{+1}_{-1}
C	258.12	−39.92	8.5	5.2	3.4	$1.1^{+0.6}_{-0.3}$	12^{+4}_{-1}

Notes Col. (1): Clump name. Col. (2)–(3): Position of the observed point with the maximum ^{12}CO($J = 3$–2) intensity peak. Col. (4)–(6): Radiation temperature averaged to the line of sight over a velocity integral of 1.5 km s^{-1}. Col. (7): Density of molecular hydrogen. Col. (8): Kinetic temperature. The parameter $X/(dV/dR)$ =4.0 × 10^{-6} (km s^{-1} pc^{-1})$^{-1}$ is used

2.3.2 Density Distribution of Clump C

Clump C is associated with a dense cloud core with a strong intensity gradient (Fig. 2.10). The total molecular mass of the core is estimated to be 400 $M_\odot$ from the ^{12}CO(J = 1–0) integrated intensity (Moriguchi et al. 2005) for an X factor of 2.0 × 10^{20} [$W(^{12}\mathrm{CO})$/(K km s^{-1})] (Bertsch et al. 1993). We shall derive the density distribution by employing a simple power-law analysis assuming a spherical symmetry. First, we de-convolve the intensity distribution in order to correct for the beam size. We assume the relation to derive a de-convolved core radius r in each transition given by $r^2 = s^2 + r'^2$, where r, s, and r' stand for the observed radius, the beam radius, and the de-convolved radius, respectively, at a half power level of the peak intensity (Table 2.8). Then, we estimate the averaged density within r, $\overline{n(\mathrm{H_2})(< r)}$, to match

Table 2.8 Density distribution and core radius for peak C

Property	^{12}CO			^{13}CO
	J = 2–1	J = 3–2	J = 4–3	J = 2–1
Beam size (arcsec)	90	22	38	90
Core radius (pc)	0.62	0.44	0.23	0.32
Average brightness (K)	0.79	1.87	1.28	0.29
Number density (10^3cm^{-3})	0.33±0.05	1.51±0.23	3.55±0.53	1.78±0.27

Notes Cols. Number density is derived by assuming T_{kin} = 12 K and $X/(dV/dR)$ =4.0 × 10^{-6} (km s^{-1} pc^{-1})$^{-1}$. We assume that the error of density caused by calibration from T_{A}^* to T_{MB} is ±15% for all intensities

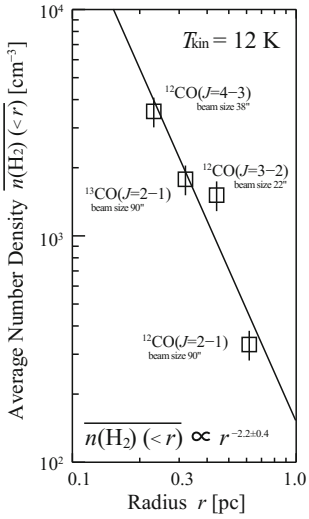

Fig. 2.14 The molecular density distribution of clump C. The calculations are conducted for T_{kin} = 12 K (see Table 2.7). The *solid line* is a regression line obtained by least squares fitting. Error bars represent only those for the radiation temperature calibration, ±15 %. See Table 2.8. for further

the observed averaged integrated intensity to the LVG estimate within the radius by assuming a kinetic temperature of 12 K and the same model parameters in Sect. 2.3.1. Considering the low luminosity of the *IRAS* source (300 $L_{\odot}$), we infer that the local temperature variation in the core is not significant and that a uniform temperature is a good approximation. The result, which is shown in Fig. 2.14, indicates that the average density distribution is well approximated by a power law, $r^{-2.2\pm0.4}$. Such a steep density gradient is consistent with a star forming cloud core (Larson 1969; Penston 1969; Lizano and Shu 1989; Onishi et al. 1999). As shown in Fig. 2.14, the line width does not vary much among the different density regimes, suggesting that the infall motion is not very large. An alternative interpretation for the density distribution will be discussed later.

2.3.3 *Physical Parameters of the Outflow*

The bipolarity of the broad CO wings in Fig. 2.11 verifies that the wings are caused by bipolar outflow driven by a protostar and is consistent with a compact dense core having a steep density gradient (Sect. 2.3.2). The physical parameters of the outflow are estimated using the method described by (Moriguchi et al. 2005, Table 2.9). The average intensities of the red component are 8.9 K and 2.0 K for the ^{12}CO(J = 2–1) and ^{12}CO(J = 4–3) transitions in a velocity range from -8 km s^{-1} to -3 km s^{-1}, respectively. The density in the line emitting wings is then estimated to be $\sim 5 \times 10^3$ cm^{-3} from the line intensity ratio, $\sim$0.23, between the ^{12}CO(J = 2–1) and ^{12}CO(J = 4–3) transitions. The beam filling factor is estimated to be as small as 5% for an assumed excitation temperature of 12 K for the rotational levels of ^{12}CO. This result is similarly obtained from the blue component, which yields a beam filling factor of $\sim$4 %. Therefore, the CO wings represent highly clumped gas, which is fairly typical for outflows. The present ^{12}CO(J = 4–3) data verify that the wings represent

Table 2.9 Outflow properties at clump C in ^{12}CO(J = 4–3)

Property	Blue component	Red component
Integrated intensity (K km s^{-1})	17.5	14.7
Size (arcmin)	0.85	0.58
Size (pc)	0.25	0.17
ΔV (km s^{-1})	15	15
$t_{\rm dyn}$ (10^4 yr)	1.6	1.1

Notes Integrated intensity is derived by summing the integrated intensities of the observed points in the area enclosed by a contour of 13.4 K within the velocity range of -30 km s^{-1} $\leq V_{\rm LSR} \leq -15$ km s^{-1} for the blue-shifted component and 11.0 K within -8 km s^{-1} $\leq V_{\rm LSR} \leq 7$ km s^{-1} for the red-shifted component, respectively. Size is defined as an effective diameter = $\sqrt{(A/\pi)} \times 2$, where A is the region enclosed by a contour of 13.4 K km s^{-1} and 11.0 K km s^{-1} for the blue-shifted and red-shifted components, respectively. ΔV is the velocity range of the wing component. The dynamical age, $t_{\rm dyn}$, is defined as $2R/\Delta V$

outflow and show that the ^{12}CO($J = 4$–3) wings are much more compact than the ^{12}CO($J = 1$–0) wings, indicating that the ^{12}CO($J = 4$–3) wings are dense outflow gases whose spatial extent is smaller than that of wings with low densities (Table 2.9, for the ^{12}CO($J = 1$–0) wings see Table 4 of Moriguchi et al. 2005). The most likely driving source of the outflow is the far infrared source *IRAS* 17089−3951. General properties for bipolar outflows are found elsewhere (e.g., Lada 1985; Fukui 1989; Fukui et al. 1993) and the outflow shown is seen to be typical in terms of size and velocity of an outflow associated with a low mass protostar.

2.4 Discussion

We present a general scenario following discussions given by Fukui et al. (2003) and Moriguchi et al. (2005). The progenitor of the supernova was a high mass star formed some Myr ago in the region that created a cavity in the ISM from its stellar wind. The local region is a star-forming region with a loose spatial association extending over a few tens of pc. Star formation in clump C may have been triggered by the progenitor of the SNR (Koo et al. 2008; Desai et al. 2010). The progenitor star caused a supernova explosion 1,600 yr ago, as recorded in a contemporary Chinese document (Wang et al. 1997), and the blast wave expanded into the cavity. The SNR is now interacting with the molecular clumps, and its interacting layer is traced by synchrotron X-rays, as supported by the high degree of spatial anti-correlation with CO clumps at a 0.1 pc scale.

We have compared the X-ray distribution with that of the CO and HI dense clumps over the entire SNR and present a schematic image of the results in Fig. 2.15. This figure indicates that the CO and dense HI clumps form an inhomogeneous shell and that the X-rays are enhanced around all the clumps. We infer that the five CO clumps C, E, I, L, and O_{SW} survived the SNR blast waves and are now embedded within the SNR, while the other twelve CO clumps and the HI clump are shock-interacting on their inner sides. As mentioned above, the ISM shell was formed over a timescale of Myr by the stellar winds of an OB star that experienced a supernova explosion 1,600 yr ago. Thus, the density in the cavity surrounded by the ISM shell is expected to be very low. The observational results also indicate that there is little dense gas left in the interior of the cavity (Figs. 2.3 and A.1). According to numerical simulations on the interaction of the ISM with the strong stellar winds from an O-type star (Weaver et al. 1977), the gas density inside the evacuated wind bubble is $\sim$0.01 cm^{-3}, which applies to the interior of the cavity.

The shock waves of the SNR first propagated in the stellar-wind cavity and then began interaction with the CO/HI clumps some 1,000 yr ago, as determined by the ratio of the shell thickness and the shock velocity, 3 pc/3000 km s^{-1}. According to MHD numerical simulations by Inoue et al. (2012), the CO/HI clumps, which have a density of $\sim 10^2$–10^3 cm^{-3}, are surrounded by an interclump gas with a density of $\sim$1 cm^{-3}, which is two orders of magnitude higher than that in the cavity. These authors showed that the shock is stalled in the dense clumps. The shock

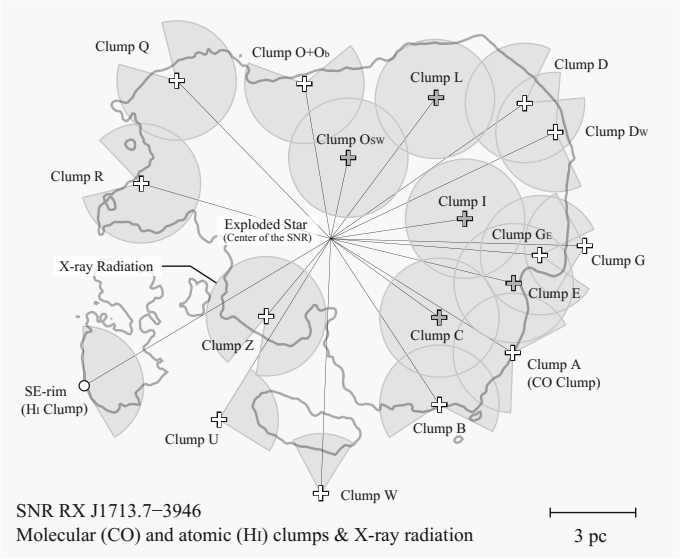

Fig. 2.15 Schematic image of the distribution of the molecular (CO) clumps (open crosses), atomic (HI) clump (*circle*) and the X-rays (shaded partial or full circles) superimposed on the *Suzaku* 1–5 keV X-ray outer boundary of the SNR (*gray* contours). The *black* open crosses (clumps C, I, E, L, and Osw) indicate the clumps fully surrounded by X-rays

velocity becomes $V_{\rm sh,clump} = V_{\rm sh,interclump}(n_{\rm interclump}/n_{\rm clump})^{0.5}$, where the interclump density $n_{\rm interclump} = 1\ {\rm cm}^{-3}$ and the clump density $n_{\rm clump} = 10^2$–$10^3\ {\rm cm}^{-3}$. The shock velocity difference between the dense CO/HI clumps and the interclump gas assumes a factor of ∼10–30. They calculated that the temperature of the shocked dense gas becomes much lower than the temperature in the post-shock diffuse gas and argued that thermal X-ray emission from the CO/HI clumps is strongly suppressed after passage of the shock (see Sect. 4.3 of Inoue et al. 2012). The interclump gas does not emit significant thermal X-rays either because the density ∼1 $\rm cm^{-3}$ is less than ∼2 $\rm cm^{-3}$, the average density inside the SNR obtained from the upper limit of the thermal X-rays (Takahashi et al. 2008). Moreover, in this case, the penetrating depth in a typical timescale of interaction of ∼1000 yr can then be estimated to be ∼0.1 pc for $n = 10^3\ {\rm cm}^{-3}$ and ∼3 pc for $n = 1\ {\rm cm}^{-3}$, respectively. Clump C has a present diameter of at least 0.6 pc and a density of $10^3\ {\rm cm}^{-3}$ (Fig. 2.14), and according to the argument above, it should not have been affected significantly by shock penetration, whereas the ambient lower density gas is significantly disturbed and accelerated over a scale length of the SNR radius. We therefore infer that clump C (and other four clumps) is able to survive against the shock wave as originally suggested by Fukui et al. (2003), whereas the lower density ambient gas is significantly disturbed and accelerated.

An important consequence of this interaction is that the large velocity difference created between the clumps and the interclump space induces turbulence, which

leads to turbulent dynamo action. The magnetic field is then amplified to as high as 1 mG, which is consistent with the field strength derived from rapid time variation of the X-ray filaments (Uchiyama et al. 2007), while an alternative is that fluctuations in field orientation may explain the rapid time variation (Helder et al. 2012). The synchrotron flux integrated over the line of sight is proportional to $B^{1.5}$ if the spectral index of electrons p is 2.0 (e.g., Rybicki and Lightman 1979). It is therefore possible to enhance the X-ray radiation around the CO and HI clumps. It is known that owing to the effect of synchrotron cooling, the power of synchrotron X-ray emission is not enhanced by magnetic field amplification if the amplification takes place in the vicinity of a forward shock where electrons are being accelerated (e.g., Nakamura et al. 2012). In the present case, as discussed by Inoue et al. (2009, 2010, 2012), the magnetic field amplification owing to the shock–cloud interaction is effective at least 0.1 pc downstream from the shock front. This indicates that the synchrotron X-rays are emitted after the acceleration process, and thus, the power of the synchrotron X-rays is enhanced by amplification. The observed power of the X-ray emission around the CO and HI clumps is 2–7 times higher than the background level inside the SNR. If the X-ray enhancement was only caused by magnetic field amplification, the magnetic field around the CO and HI clumps would be an estimated 2–4 times higher than that present elsewhere in the SNR. The averaged magnetic field around the CO and HI clumps becomes 30–60 μG if the initial field is assumed to be 15 μG (e.g., Tanaka et al. 2008). The average field strength can also be estimated from the width of synchrotron X-ray filaments as ∼100 μG (Bell 2004; Hiraga et al. 2005; Ballet 2006). Note that the dependence of the synchrotron flux on the magnetic field strength can be much more sensitive than that in the above-mentioned standard case, because the high-energy electrons that contribute the X-ray synchrotron emission can be in the cut-off regime (Bykov et al. 2008). Moreover, such enhanced magnetic field in turbulence may lead to more efficient acceleration than that in the case of diffusive shock acceleration (Lazarian and Vishniac 1999; Hoshino 2012).

Finally, we discuss the quantitative relationship between the CO/HI interacting clump mass and the X-ray enhancement. We estimated the interacting clump masses (column (9) of Table 2.8) with the shock waves as defined by the total CO/HI mass within the azimuth angle range of the X-rays with respect to the center of gravity (column (8) of Table 2.8). For the case wherein two CO clumps have small separation ($<0.^{\circ}2$) and the X-ray peak is situated between the CO clumps, we summed up the interacting clump masses and averaged the X-ray intensities (D+D_W, O+O_b+O_{SW}, G+G_E, and E+I; see also Table 2.8). In Fig. 2.16, we plot the CO/HI interacting clump mass as a function the X-ray peak intensity. Here, we approximate the mass of the SE rim to be 134 $M_\odot$ on the assumption that it has a size 0.8 pc^2 along the X-ray boundary. The result, shown in Fig. 2.16, indicates that the correlation between the interacting clump mass and the X-ray intensity is good with a correlation coefficient of ∼0.85 in double logarithm. We can conclude that the intensity is roughly proportional to the interacting mass of each CO/HI clump at a pc scale. This result suggests that the ISM distribution is crucial to producing the non-thermal X-ray distribution in young SNRs.

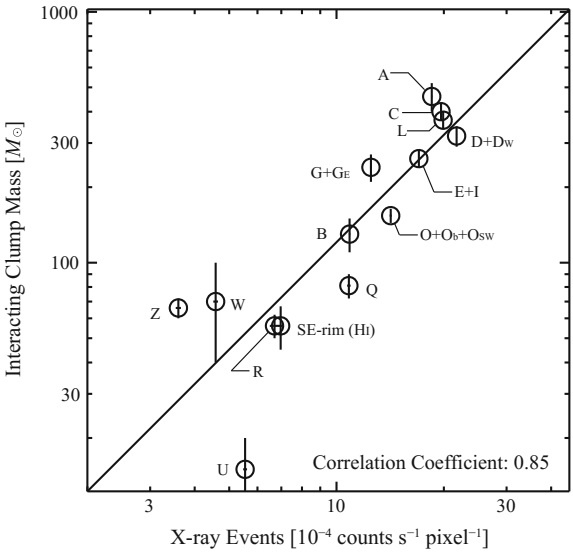

Fig. 2.16 Correlation plot between the X-ray peak intensity in the azimuthal distributions derived in Fig. 2.8 and the interacting clump mass with the shock waves, which is estimated by the CO or HI mass within the azimuth angle range of the X-rays for each clump (see for more details the text, and column (9) of Table 2.8). The linear regression by the least-squares fitting is shown by the solid line, where the correlation coefficient is ∼0.85 in double logarithm

2.5 Conclusions

We summarize the present work as follows.

1. We have shown that all the major CO and HI clumps with mass greater than 50 $M_\odot$ interacting with shock waves in RX J1713.7−3946 are associated with non-thermal X-rays. The X-rays are enhanced within ∼1 pc of the CO and HI peaks, whereas at smaller scales down to 0.1 pc, the CO peaks tend to be anti-correlated with X-ray intensity, which is decreased around the CO and HI clumps. We have shown good correlation between the CO/HI clump mass interacting with the shock waves and the X-ray intensity.
2. Sub-millimeter results indicate that the core of clump C has a strong density gradient consistent with an average density distribution of $r^{-2.2\pm0.4}$, where r is the radius from the center of the core. The density and temperature, averaged over $90''$ (= 0.2 pc), are 0.8–1.7 × 10^4 cm^{-3} and 11–16 K, respectively, as derived from the LVG analysis. Clump C is also associated with a bipolar outflow as evidenced by the ^{12}CO(J = 4–3) broad wings of at least 30 km s^{-1} velocity extent. Along with the far infrared spectrum, these identify the region as a site of recent low-mass star formation within Myr. This verifies that the broad wings are not produced by the shock acceleration driven by the SNR, as suggested before by Fukui et al. (2003). Clump A has density and temperature of 5–8 × 10^3 cm^{-3} and 9–11 K, respectively, somewhat lower than those of clump C. The *IRAS* sources in clump A and D are also likely protostars, as noted by Moriguchi et al. (2005), because of the high density of these peaks.

3. The present findings in (1) are compared with numerical simulations of MHD in a realistic highly inhomogeneous density distribution by Inoue et al. (2009, 2012). These simulations indicate that the magnetic field is amplified around dense CO/HI clumps as a result of enhanced turbulence induced by the shock–cloud interaction. We interpret that magnetic fields amplified by this interaction enhance the X-ray intensity, which is proportional to the 1.5-th power of the magnetic field strength. Such enhanced magnetic fields may also lead to efficient acceleration additional to the DSA. More comparative study of the distribution of X-rays and the ISM will allow us to develop deeper insight into the origin of X-ray distributions.

References

J. Ballet, Adv. Space Res. **37**, 1902 (2006)
A.R. Bell, Mon. Not. R. Astron. Soc. **353**, 550 (2004)
D.L. Bertsch, T.M. Dame, C.E. Fichtel, S.D. Hunter, P. Sreekumar, J.G. Stacy et al., Astrophys. J. **416**, 587 (1993)
G.A. Blake, E.C. Sutton, C.R. Masson, T.G. Phillips, Astrophys. J. **315**, 621 (1987)
M. Burgay, N. Rea, G.L. Israel, A. Possenti, L. Burderi, T. di Salvo et al., Mon. Not. R. Astron. Soc. **372**, 410 (2006)
A.M. Bykov, Y.A. Uvarov, D.C. Ellison, Astrophys. J. Lett. **689**, L133 (2008)
R.M. Cutri, M.F. Skrutskie, S. van Dyk, C.A. Beichman, J.M. Carpenter, T. Chester et al., VizieR Online Data Catalog **2246** (2003)
L.K. Denoyer, Astrophys. J. Lett. **232**, L165 (1979)
K.M. Desai, Y.-H. Chu, R.A. Gruendl, W. Dluger, M. Katz, T. Wong et al., Astron. J. **140**, 584 (2010)
R.P. Eatough, M. Kramer, A.G. Lyne, M.J. Keith, Mon. Not. R. Astron. Soc. **431**, 292 (2013)
J.P. Emerson, NATO ASIC Proceedings 241: Formation and Evolution of Low Mass Stars, vol. 193 (1988)
Y. Fukui, T. Iwata, A. Mizuno, J. Bally, A.P. Lane, Protostars and Planets **III**, 603 (1993)
Y. Fukui, Eur. South. Obs. Conf. Workshop Proc. **33**, 95 (1989)
Y. Fukui, Y. Moriguchi, K. Tamura, H. Yamamoto, Y. Tawara, N. Mizuno et al., Publ. Astron. Soc. Jpn. **55**, L61 (2003)
Fukui,Y. in, *AIP Conference Proceedings, Proceedings of 4th International Meeting on High-Energy Gamma-Ray Astronomy*, ed. F.A. Aharonian, W. Hofmann, F. Rieger, Vol. 1085, p. 104 (Melville, NY: AIP, 2008)
Y. Fukui, H. Sano, J. Sato, K. Torii, H. Horachi, T. Hayakawa et al., Astrophys. J. **746**, 82 (2012)
R. Güsten, S.D. Philipp, The Dense Interstellar Medium in Galaxies, vol. 253 (2004)
P. Goldreich, J. Kwan, Astrophy. J. **189**, 441 (1974)
M. Gottwald, A.N. Parmar, A.P. Reynolds, N.E. White, A. Peacock, B.G. Taylor, Astron. Astrophys. Suppl. **109**, 9 (1995)
S. Guillot, R.E. Rutledge, E.F. Brown, G.G. Pavlov, V.E. Zavlin, Astrophys. J. **699**, 1418 (2009)
E.A. Helder, J. Vink, A.M. Bykov, Y. Ohira, J.C. Raymond, R. Terrier, Space Sci. Rev. **173**, 369 (2012)
J.S. Hiraga, Y. Uchiyama, T. Takahashi, F.A. Aharonian, Astron. Astrophys. **431**, 953 (2005)
M. Hoshino, Phys. Rev. Lett. **108**, 135003 (2012)
T. Inoue, R. Yamazaki, S.-I. Inutsuka, Astrophys. J. **695**, 825 (2009)
T. Inoue, R. Yamazaki, S.-I. Inutsuka, Astrophys. J. Lett. **723**, L108 (2010)
T. Inoue, R. Yamazaki, S.-I. Inutsuka, Y. Fukui, Astrophys. J. **744**, 71 (2012)

Y. Ishisaki, Y. Maeda, R. Fujimoto, M. Ozaki, K. Ebisawa, T. Takahashi et al., Publ. Astron. Soc. Jpn. **59**, 113 (2007)
B.-C. Koo, C.F. McKee, J.-J. Lee, H.-G. Lee, J.-E. Lee, D.-S. Moon et al., Astrophys. J. Lett. **673**, L147 (2008)
K. Koyama, K. Kinugasa, K. Matsuzaki, M. Nishiuchi, M. Sugizaki, K. Torii et al., Publ. Astron. Soc. Jpn. **49**, L7 (1997)
K. Koyama, H. Tsunemi, T. Dotani, M.W. Bautz, K. Hayashida, T.G. Tsuru et al., Publ. Astron. Soc. Jpn. **59**, 23 (2007)
C.A. Kulesa, A.L. Hungerford, C.K. Walker, X. Zhang, A.P. Lane, Astrophys. J. **625**, 194 (2005)
C.J. Lada, Ann. Rev. Astron. Astrophys. **23**, 267 (1985)
H. Landt, H.E. Bignall, Mon. Not. R. Astron. Soc. **391**, 967 (2008)
R.B. Larson, Mon. Not. R. Astron. Soc. **145**, 271 (1969)
A. Lazarian, E.T. Vishniac, Astrophys. J. **517**, 700 (1999)
J.S. Lazendic, P.O. Slane, B.M. Gaensler, P.P. Plucinsky, J.P. Hughes, D.K. Galloway et al., Astrophys. J. Lett. **593**, L27 (2003)
D. Lin, N.A. Webb, D. Barret, Astrophys. J. **756**, 27 (2012)
S. Lizano, F.H. Shu, Astrophys. J. **342**, 834 (1989)
F.J. Lu, T.P. Li, X.J. Sun, M. Wu, C.G. Page, Astron. Astrophys. Suppl. **115**, 395 (1996)
N.M. McClure-Griffiths, J.M. Dickey, B.M. Gaensler, A.J. Green, M. Haverkorn, S. Strasser, Astrophys. J. **158**, 178 (2005)
Y. Mizuno, A. Kawamura, T. Onishi, T. Minamidani, E. Muller, H. Yamamoto et al., Publ. Astron. Soc. Jpn. **62**, 51 (2010)
Y. Moriguchi, K. Tamura, Y. Tawara, H. Sasago, K. Yamaoka, T. Onishi et al., Astrophys. J. **631**, 947 (2005)
H. Nakajima, H. Yamaguchi, H. Matsumoto, T.G. Tsuru, K. Koyama, H. Tsunemi et al., Publ. Astron. Soc. Jpn. **60**, 1 (2008)
R. Nakamura, A. Bamba, T. Dotani, M. Ishida, R. Yamazaki, K. Kohri, Astrophys. J. **746**, 134 (2012)
T. Onishi, A. Mizuno, Y. Fukui, Publ. Astron. Soc. Jpn. **51**, 257 (1999)
M.V. Penston, Mon. Not. R. Astron. Soc. **145**, 457 (1969)
E. Pfeffermann, B. Aschenbach, in, *Proceedings of Roentgenstrahlung from the Universe*, ed. H.U. Zimmermann, J.H. Trümper, H. Yorke, vol. 267 (1996)
J.L. Pineda, N. Mizuno, J. Stutzki, M. Cubick, M. Aravena, F. Bensch et al., Astron. Astrophys. **482**, 197 (2008)
A.P. Reynolds, A.N. Parmar, P.J. Hakala, A.M.T. Pollock, O.R. Williams, A. Peacock et al., Astron. Astrophys. Suppl. **134**, 287 (1999)
G.B. Rybicki, A.P. Lightman, *Radiative Processes in Astrophysics* (Wiley-Interscience, New York, 1979)
N. Schneider, J. Stutzki, G. Winnewisser, D. Block, Astron. Astrophys. **335**, 1049 (1998)
N.Z. Scoville, P.M. Solomon, Astrophys. J. Lett. **187**, L67 (1974)
P.J. Serlemitsos, Y. Soong, K.-W. Chan, T. Okajima, J.P. Lehan, Y. Maeda et al., Publ. Astron. Soc. Jpn. **59**, 9 (2007)
P. Slane, B.M. Gaensler, T.M. Dame, J.P. Hughes, P.P. Plucinsky, A. Green, Astrophys. J. **525**, 357 (1999)
P. Slane, J.P. Hughes, R.J. Edgar, P.P. Plucinsky, E. Miyata, H. Tsunemi et al., Astrophys. J. **548**, 814 (2001)
T. Takahashi, K. Abe, M. Endo, Y. Endo, Y. Ezoe, Y. Fukazawa et al., Publ. Astron. Soc. Jpn. **59**, 35 (2007)
T. Takahashi, T. Tanaka, Y. Uchiyama, J.S. Hiraga, K. Nakazawa, S. Watanabe et al., Publ. Astron. Soc. Jpn. **60**, 131 (2008)
T. Tanaka, Y. Uchiyama, F.A. Aharonian, T. Takahashi, A. Bamba, J.S. Hiraga et al., Astrophys. J. **685**, 988 (2008)
W.W. Tian, Z. Li, D.A. Leahy, J. Yang, X.J. Yang, R. Yamazaki et al., Astrophys. J. **712**, 790 (2010)

Y. Uchiyama, T. Takahashi, F.A. Aharonian, Publ. Astron. Soc. Jpn. **54**, L73 (2002)
Y. Uchiyama, F.A. Aharonian, T. Tanaka, T. Takahashi, Y. Maeda, Nature **449**, 576 (2007)
H. Uchiyama, M. Ozawa, H. Matsumoto, T.G. Tsuru, K. Koyama, M. Kimura et al., Publ. Astron. Soc. Jpn. **61**, 9 (2009)
M. van den Berg, K. Penner, J. Hong, J.E. Grindlay, P. Zhao, S. Laycock et al., Astrophys. J. **748**, 31 (2012)
K.A. van der Hucht, New A Rev. **45**, 135 (2001)
W. Voges, B. Aschenbach, T. Boller, H. Bräuninger, U. Briel, W. Burkert et al., Astron. Astrophys. **349**, 389 (1999)
Z.R. Wang, Q.-Y. Qu, Y. Chen, Astron. Astrophys. **318**, L59 (1997)
R. Weaver, R. McCray, J. Castor, P. Shapiro, R. Moore, Astrophys. J. **218**, 377 (1977)
H.A. Wootten, Astrophys. J. **216**, 440 (1977)
A. Wootten, Astrophys. J. **245**, 105 (1981)
V.N. Zirakashvili, F. Aharonian, Astron. Astrophys. **465**, 695 (2007)
V.N. Zirakashvili, F.A. Aharonian, Astrophys. J. **708**, 965 (2010)

Chapter 3
Evidence for the Acceleration of Cosmic Ray Protons

The explanation of how cosmic ray protons, the major constituent of cosmic rays, are accelerated in interstellar space has been a longstanding problem. Supernova (SN) remnants (SNRs) are the most likely candidates for acceleration below the *knee* energy ($\sim 10^{15.5}$ eV) because their high-speed shock waves offer an ideal site for diffusive shock acceleration (DSA; see Sect. 1.3.2 for details). The principal site of cosmic ray proton acceleration, however, has not yet been identified observationally despite a number of efforts to address this issue. In particular, it is not clear whether cosmic ray protons have been accelerated to near *knee* energy.

The young ($\sim$1600 yr) SNR RX J1713.7−3946 is one of the most promising candidates for establishing the origin of the γ-rays. γ-rays higher than 10 TeV are detected here, suggesting that the responsible cosmic ray protons have energies close to the *knee* energy if the γ-rays are produced by π^0-decay Aharonian et al. (2007) (hadronic process; also see Sect. 1.4.3). Furthermore, the SNR is interacting with dense molecular clumps (Fukui et al. 2003; Moriguchi et al. 2005, see also Chap. 2). Importantly, the molecular gas associated with the SNR presents a possibility to identify target protons where the hadronic process is working. **If the cosmic ray density is nearly uniform, we expect the hadronic γ-ray distribution to mimic that of the interstellar target protons** (see Eq. 1.51). Some nearby molecular clouds show good spatial correlation with relatively high resolution γ-ray images, clearly verifying that the hadronic process is working to produce γ-rays in the cosmic ray sea (e.g., Ackermann et al. 2012). A detailed comparison between the interstellar medium (ISM) protons and the recent high-resolution γ-ray images from H.E.S.S. sources is useful to test the correlation, although such a test was not possible until recently in preceding low resolution γ-ray observations at degree-scale resolution. Aharonian et al. (2006a) compared the NANTEN CO distribution with the H.E.S.S. very high energy (VHE) γ-ray image and examined both leptonic and hadronic scenarios as origins of the γ-rays. By adopting annular averaging of VHE γ-rays and CO in the shell (see Fig. 1.10 in Sect. 1.5.2), these authors found that VHE γ-rays are fairly well correlated with CO, although this correlation is not complete in the

H. Sano, *Shock-Cloud Interaction in RX J1713.7–3946*,
Springer Theses, DOI 10.1007/978-4-431-55636-7_3

sense that the southeastern rim of the VHE γ-ray shell has no counterpart in CO. The complete identification of target ISM protons has thus remained unsettled in the hadronic scenario.

The γ-and X-rays are significantly enhanced toward the clumpy molecular gas at a pc scale, as first shown by Fukui et al. (2003). A strong connection among the molecular gas, γ-rays, X-rays, and perhaps cosmic rays is therefore suggested (Fukui et al. 2003; Fukui 2008; Zirakashvili and Aharonian 2010, and Chap. 2). Most of the previous models of γ-and X-rays cited earlier assume more or less uniform density distribution of the ISM in the SNR, whereas the observations of the ISM indicate that the actual distribution is highly inhomogeneous, with density varying by a factor 100 or more around the SNR. In addition, Galactic-scale studies of γ-rays suggest that there is "dark gas" that is not detectable in CO or in HI but still contributes to the γ-rays and visual extinction (Grenier et al. 2005; Planck Collaboration et al. 2011). Such gas may either be cold HI or H_2 with no detectable CO. It is therefore important to consider HI carefully in order to have a comprehensive understanding of the ISM protons. In the present study, we shall use the term "dark HI" for observed HI with significantly lower brightness than the surroundings. As such, "dark HI" does not mean the same as "dark gas" above.

We here present a combined analysis of both ^{12}CO($J = 1$–0) and HI data sets to clarify the distribution of the ISM protons and compare it with the VHE γ-ray distribution in RX J1713.7−3946. The present work will reveal the VHE γ-ray origin in the SNR and propose a new approach to understanding the origin of galactic cosmic rays.

3.1 Datasets of CO, HI, and VHE γ-rays

3.1.1 CO

The ^{12}CO($J = 1$–0) data at 2.6 mm wavelength were taken using the NANTEN 4-m telescope in 2003 April and are identical with those published by Moriguchi et al. (2005). The system temperature of the SIS receiver was ∼250 K in the single side band including the atmosphere toward the zenith. The beam size of the telescope was 2′.6 at 115 GHz, and we adopted a grid spacing of 2′.0 in the observations. The velocity resolution and rms noise fluctuations are 0.65 km s^{-1} and 0.3 K, respectively. The ^{12}CO($J = 2$–1) data at 1.3 mm wavelength were taken with the NANTEN2 4-m telescope in the period from August to November in 2008, and part of the data set is shown in Chap. 2. The front end was a 4 K cooled Nb SIS mixer receiver and the single-side-band (SSB) system temperature was ∼250 K, including the atmosphere toward the zenith. The telescope had a beam size of 90″ at 230 GHz. We used an acoustic optical spectrometer (AOS) with 2,048 channels with a bandwidth of 390 km s^{-1} and a resolution per channel of 0.38 km s^{-1}. Observations in ^{12}CO($J =$ 2–1) were recorded in the on-the-fly (OTF) mode, scanning with an integration time

of 1.0–2.0 s per point. The chopper wheel method was employed for the intensity calibration and the derived $T_{\rm rms}$ was better than 0.66 and 0.51 K per channel with 1.0 and 2.0 s integrations, respectively. An area of 2.25 deg^2 in a region of $346.^\circ7 \leq l \leq 348.^\circ2$ and $-1.^\circ3 \leq b \leq 0.^\circ4$ was observed.

Moriguchi et al. (2005) showed an analysis of the ^{12}CO($J = 1$–0) distribution over 100 km s^{-1} with a coarse velocity window of 10 km s^{-1} to test its association with the SNR. These authors showed that the velocity range $V_{\rm LSR} = -20$ to 0 km s^{-1} has convincing signs of association with the SNR. In the present work, we adopt the velocity interval -20 to 0 km s^{-1} for the associated ISM and present detailed ^{12}CO ($J = 1$–0, 2–1) and HI data for every 1 km s^{-1} (see Figure Appendix A.2).

3.1.2 *HI*

The HI data at 21 cm wavelength are from the Southern Galactic Plane Survey (SGPS; McClure-Griffiths et al. 2005) as well as from the Australia Telescope Compact Array (ATCA) and the Parkes Radio Telescope. The beam size of the data set is $2.'2$ and we adopted a grid spacing of $40''$ toward RX J1713.7−3946 in the current analysis. The velocity resolution and typical rms noise fluctuations are 0.82 km s^{-1} and 1.9 K, respectively.

3.1.3 *VHE γ-rays*

For the H.E.S.S. γ-ray data, we used the combined H.E.S.S. image shown in Fig. 2 of Aharonian et al. (2007). Data from 2004 and 2005 are used for this smoothed, acceptance-corrected γ-ray excess image. The VHE image utilizes a minimum of three H.E.S.S. telescopes in event reconstruction to obtain a Gaussian standard deviation of $0.^\circ06$ or full width at half maximum (FWHM) of $0.^\circ14$ ($8.'3$).

3.2 Combined Analysis of the CO and HI Data

3.2.1 *Distribution of CO and HI*

Figure 3.1a shows the VHE γ-ray distribution toward RX J1713.7−3946 obtained by H.E.S.S. and Fig. 3.1b shows a velocity-averaged distribution of ^{12}CO($J = 1$–0) overlaid onto the VHE γ-ray distribution. The ^{12}CO($J = 1$–0) intensity is larger in the north of the Galactic plane than that in the south, and the most prominent features above 0.7 K are located in the northwest. The general ^{12}CO($J = 1$–0) distribution is shell-like and associated with the γ-ray shell, showing weaker or no CO emission in parts of the south. There are two regions where ^{12}CO($J = 1$–0) delineates particularly well the outer boundary of the shell in the southwest and east.

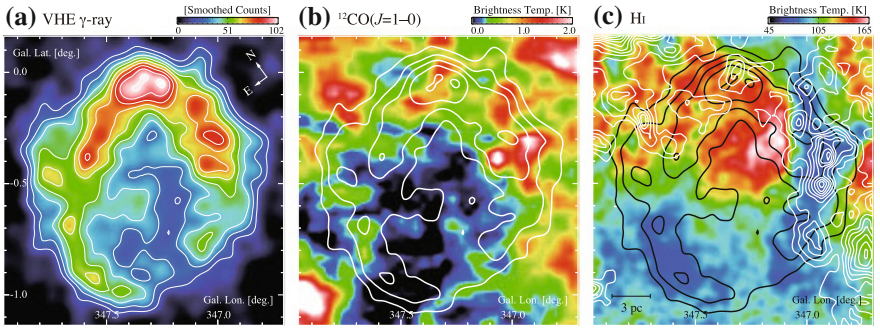

Fig. 3.1 **a** The H.E.S.S. VHE γ-ray distribution of RX J1713.7−3946 in smoothed excess counts see Fig. 2 of Aharonian et al. 2007. Note the use of Galactic coordinates to accentuate the position relative to the Galactic plane. Contours are plotted every 10 smoothed counts from 20 smoothed counts. **b** Averaged brightness temperature distribution of ^{12}CO($J = 1$–0) emission in a velocity range of $V_{\rm LSR} = -20$ to $0\,{\rm km\,s^{-1}}$ is shown in *color* (Fukui et al. 2003; Moriguchi et al. 2005). White contours show the H.E.S.S. VHE γ-ray distribution and are plotted every 20 smoothed counts from 20 smoothed counts. **c** Averaged brightness temperature distribution of HI emission obtained by ATCA and Parkes in a velocity range from $V_{\rm LSR} = -8$ to $-6\,{\rm km\,s^{-1}}$ (McClure-Griffiths et al. 2005) is shown in *color*. *White* contours show the ^{12}CO($J = 1$–0) brightness temperature integrated in the same velocity range every $1.0\,{\rm K\,km\,s^{-1}}$ ($\sim 3\sigma$)

The ^{12}CO($J = 2$–1) distribution is qualitatively similar to the ^{12}CO($J = 1$–0) distribution (see Appendix Figure A2). A typical ratio of the $J = 2$–1/$J = 1$–0 line intensities is $\sim$0.6, consistent with what is derived in other molecular clouds without heat sources (e.g. Ohama et al. 2010; Torii et al. 2011). We tentatively chose from Figure A2 in Appendix A three major CO clouds, W, N, and SW, and three minor clouds, E, NE, and SE, for the sake of discussion, as shown schematically in Fig. 3.2a, where we use ^{12}CO($J = 2$–1) data by taking advantage of higher angular resolution.

Figure 3.1c shows an overlay of the HI distribution superposed on the ^{12}CO($J = 1$–0) intensity in a velocity range of -8.0 to $-6.0\,{\rm km\,s^{-1}}$. The average HI brightness temperature ranges from 60 to 150 K and increases toward the Galactic plane. The brightest HI of $\sim$150 K, the central cloud, is located toward the center of the SNR [$(l, b) = (347.^{\circ}25, -0.^{\circ}38)$] ^{12}CO($J = 1$–0) is seen. We find dark HI clouds of around 60 K in the west (W cloud) and in the southeast (SE cloud). These dark HI clouds are not caused by absorption of the radio continuum radiation, which is very weak toward the SNR (Lazendic et al. 2004). The dark HI W cloud well corresponds to the ^{12}CO($J = 1$–0) distribution, showing sharp edges toward both the east and west. The dark HI SE cloud has almost no counterpart in CO. The relatively bright HI emission is seen in the north of the SNR (N cloud). The N cloud tends to be located toward ^{12}CO($J = 1$–0) peaks, whereas the HI brightness shows a non-monotonic, more complicated behavior than that in the W cloud. In the northeast, we find a rim of relatively lower HI brightness of $\sim$100 K toward $(l, b) = (347.^{\circ}5, -0.^{\circ}25)$ that lies along the γ-ray shell. A schematic of the four main HI clouds is given in Fig. 3.2b. The good correspondence of the HI clouds with the CO and the γ-rays supports the fact that the HI is physically associated with the SNR.

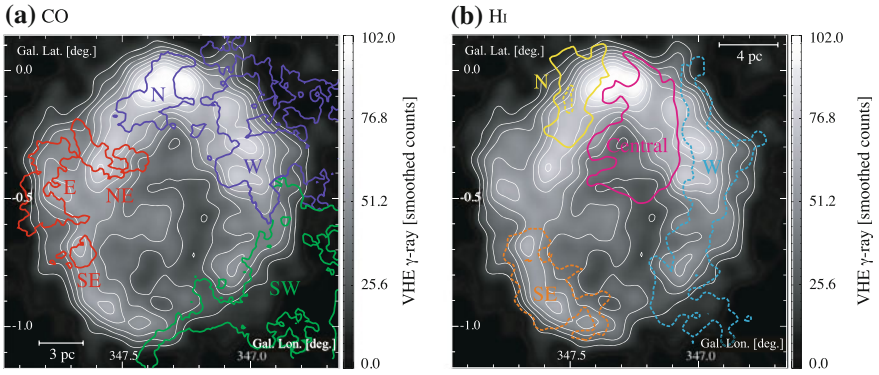

Fig. 3.2 **a** Schematic of the identified ^{12}CO($J = 2$–1) clouds is shown in *colored* contours. The image and *white* contours show the VHE γ-ray distribution (Fig. 3.1a). The integration velocity ranges are as follows: -8 to $-2\,\mathrm{km\,s^{-1}}$ (contour level: $2.3\,\mathrm{K\,km\,s^{-1}}$) for the SW cloud (CO), -17 to $-5\,\mathrm{km\,s^{-1}}$ (contour level: $4.9\,\mathrm{K\,km\,s^{-1}}$) for the W and N clouds (CO), and -6 to $0\,\mathrm{km\,s^{-1}}$ (contour level: $2.7\,\mathrm{K\,km\,s^{-1}}$) for the NE, E, and SE clouds (CO). **b** The locations of the identified HI clouds are shown in *colored* contours. The *gray* scale image and *white* contours show the VHE γ-ray distribution. The solid contours are for HI emission and the *dashed* contours are for dark HI. The integration velocity ranges are as follows: -8 to $-2\,\mathrm{km\,s^{-1}}$ (contour level: $214\,\mathrm{K\,km\,s^{-1}}$) for the W cloud (HI), -12 to $-4\,\mathrm{km\,s^{-1}}$ (contour level: $780\,\mathrm{K\,km\,s^{-1}}$) for the central and SE clouds (HI), and -14 to $-11\,\mathrm{km\,s^{-1}}$ (contour level: $399\,\mathrm{K\,km\,s^{-1}}$) for the N cloud (HI)

In Fig. 3.3, we show typical HI and CO profiles in the four main HI clouds. Figure 3.3 indicates that the HI emission generally peaks at $-10\,\mathrm{km\,s^{-1}}$ with small hints of saturation, confirming that the HI is associated with the SNR and is generally not optically thick. We find that narrow HI dips having depths of 20–30 K often correspond to ^{12}CO($J = 1$–0) emission features in the N and W clouds. The line widths of the narrow HI dips are as small as a few $\mathrm{km\,s^{-1}}$. It is likely that these HI dips represent residual HI in cold CO gas, which is seen as self-absorption. The broad HI dip in the SE cloud is also ascribed to self-absorption, as argued into detail in Sect. 3.2.3.3. We show HI expected profiles of the background HI emission with a straight-line approximation as dashed areas in Fig. 3.3 (e.g., Sato, Fukui 1978).

3.2.2 Molecular Protons

To convert the ^{12}CO($J = 1$–0) intensity into the total molecular column density, we use an X_{CO} factor defined as $X_{\mathrm{CO}}\ (\mathrm{cm^{-2}(K\,km\,s^{-1})^{-1}}) = N(\mathrm{H_2})\ (\mathrm{cm^{-2}})/W(^{12}\mathrm{CO})\ (\mathrm{K\,km\,s^{-1}})$. In order to derive an X_{CO} factor, the ^{12}CO($J = 1$–0) intensity is compared with the cloud dynamical mass (virial mass) or with the γ-rays produced via interaction of cosmic ray protons with molecular clouds. An X_{CO} factor therefore accounts for the total hadronic mass and is observationally uniform in the Galactic disk (e.g., Fukui and Kawamura 2010). We here adopt an X_{CO} factor of 2.0×10^{20}

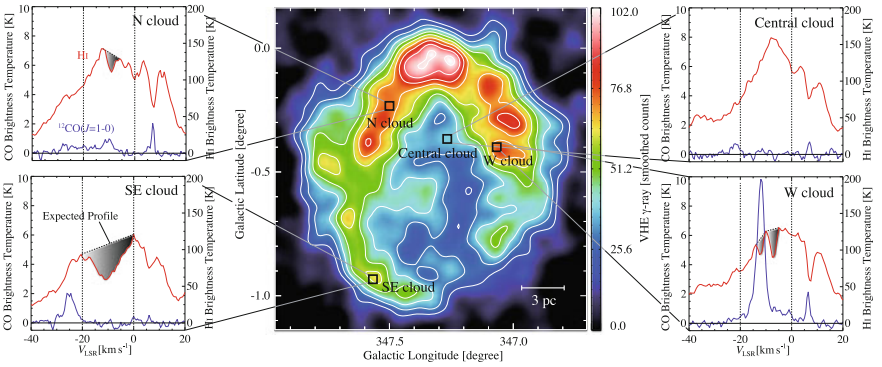

Fig. 3.3 ^{12}CO($J = 1$–0) and HI profiles at the four HI clouds; the N cloud $(l, b) = (347.^{\circ}50, -0.^{\circ}23)$, the SE cloud $(l, b) = (347.^{\circ}57, -0.^{\circ}93)$, the central cloud $(l, b) = (347.^{\circ}27, -0.^{\circ}37)$, and the W cloud $(l, b) = (347.^{\circ}07, -0.^{\circ}40)$. The positions are denoted in the VHE γ-ray distribution. The *shaded area* shows expected profiles behind the self-absorption

$W(^{12}\mathrm{CO})$ (cm^{-2} / $\mathrm{K\,km\,s}^{-1}$) derived from the γ-rays and ^{12}CO($J = 1$–0) intensity in the Galaxy (Bertsch et al. 1993). We double the H_2 column density to derive the ISM protons in molecular form. Compared with the ^{12}CO($J = 1$–0) line, the ^{12}CO ($J = 2$–1) line is not a common probe of the molecular mass. This is in part because the ^{12}CO($J = 2$–1) emission samples a smaller portion of a molecular cloud with a higher excitation condition than that traced by the ^{12}CO($J = 1$–0) emission. We estimate, for instance, that a typical fraction in area of the ^{12}CO($J = 2$–1) emission to the ^{12}CO($J = 1$–0) emission is about 70–80 % at the half-intensity level convolved to the same beam size in the present region from the CO data in Fig. A2.

3.2.3 Atomic Protons

3.2.3.1 Optically Thin Case

We use the 21 cm HI transition to estimate the atomic proton column density. A usual assumption is that the HI emission is optically thin and the following relationship is used to calculate the HI column density:

$$N_{\mathrm{p}}(\mathrm{HI}) = 1.823 \times 10^{18} \int T_L(V) dV \ \ (\mathrm{cm}^{-2}), \tag{3.1}$$

where $T_L(V)$ is the observed HI brightness temperature (K) (Dickey and Lockman 1990). We note that this simple assumption is usually valid and apply Eq. 3.1 to the regions where no HI dips are seen. It is certain from their exact coincidence with CO in terms of velocity that the narrow HI dips in the W and N clouds represent self-

absorption by cold residual HI in CO gas. The most prominent dark HI cloud, the SE cloud, shows large line-widths, which are not as common as self-absorption. We shall examine if the SE cloud represents self-absorption in the following discussion.

3.2.3.2 The Dark HI SE Cloud

We first show an integrated intensity image of the SE cloud in Fig. 3.4a. The HI contours are at each 3.9σ noise level and show significant details not apparent in Fig. 3.1c, where a coarser color code is used. We find that the HI brightness variation is generally well correlated with the shell of VHE γ-rays, shown in gray scale, in the sense that HI brightness decreases toward the enhanced γ-rays. This trend lends support for a physical connection between the SE cloud and the γ-ray shell and may be interpreted as being caused by a decrease in spin temperature with increasing density in the self-absorbing HI gas (see Sect. 3.2.3.3). No ^{12}CO($J = 1$–0) emission is seen toward the SE cloud, except for a possible small counterpart at (l, b) = (347.°64, −0.°72) and $V_{\rm LSR} = -6$ to 0 km s^{-1} (Figs. 3.2a and A2), suggesting that density of the SE cloud is lower than that of the CO clouds.

Figure 3.4b shows a typical HI profile in the SE cloud with a deep and broad dip. The large velocity span of 20 km s^{-1} is not as common as a self-absorption feature; in nearby dark clouds, HI self-absorption is generally narrow with line width of a few km s^{-1} (e.g., Krčo and Goldsmith 2010), whereas HI self-absorption as broad as 10 km s^{-1} is seen in giant molecular clouds (e.g., Sato, Fukui 1978). The SE cloud delineates the γ-ray shell (Fig. 3.4a) and is possibly composed of gas compressed by the wind of a high-mass star, the SN progenitor. We investigated the velocity distribution of the SE cloud, as given in Appendix A, finding that the SE cloud shows a strong velocity gradient, which matches the blue-shifted part of an expanding

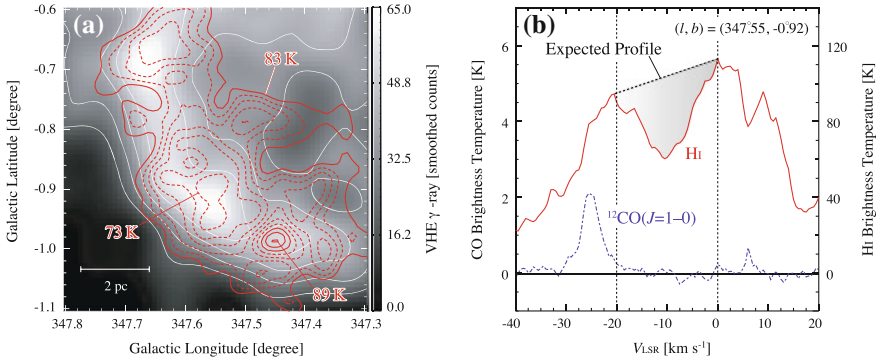

Fig. 3.4 **a** The H.E.S.S. VHE γ-ray distribution toward the SE cloud (Aharonian et al. 2007). *Red* contours show averaged HI brightness temperature distribution in a velocity range from −15 to −5 km s^{-1} (McClure-Griffiths et al. 2005). **b** The HI and ^{12}CO($J = 1$–0) spectra at (l, b) = (347.°55, −0.°92). The *shaded area* shows the expected HI profile

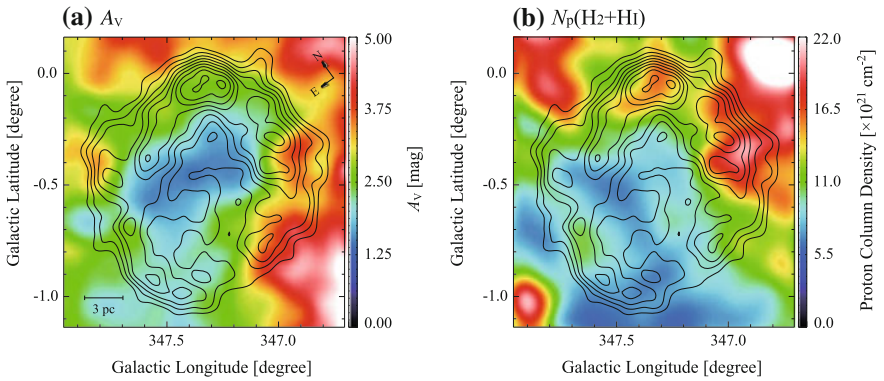

Fig. 3.5 **a** A_V distribution (Dobashi et al. 2005) is shown in *color*. Contours are the same as those in (**a**). **b** Distribution of the column density of the total ISM protons estimated from both CO and HI in a velocity range from $V_{LSR} = -20$ to 10 km s^{-1}. Here, the HI self-absorption is considered. Contours are the same as those in (**a**)

swept-up shell. Such a shell is a natural outcome of stellar-wind compression by the SN progenitor, supporting the hypothesis that the broad HI dip can be ascribed to the acceleration of HI gas by the wind. A HI stellar-wind shell in Pegasus driven by an early B-type star indeed shows a line width as large as 15 km s^{-1} (Yamamoto et al. 2006), similar to that of the SE cloud. The difference from the narrow HI dips in the W and N clouds may be density-related; the SE cloud has lower density and is subject to stronger acceleration than the CO clouds with narrow HI dips (see for further discussion Sect. 3.3.1). In contrast, the CO clouds with higher density are less accelerated by the wind, making a systematic velocity gradient less clear in CO than that in HI (see Fig. B2).

Figure 3.5a shows the distribution of the extinction A_V toward RX J1713.7−3946 (Dobashi et al. 2005) and indicates that the SE cloud, as well as the rest of the shell, is traced by the enhanced optical extinction. This lends further support to the self-absorption interpretation of the SE cloud. Figure 3.5b shows the total (molecular and atomic) ISM proton column density both in the SNR (derived later in Sect. 3.2.4) and in the foreground within 1 kpc, which is assumed to mainly correspond to optical extinction. The total proton column density N_p of $\sim 10^{22}$ cm^{-2} in Fig. 3.5b corresponds to an extinction of ∼4 mag if we adopt the relationship $N_p(\mathrm{cm}^{-2}) = 2.5 \times 10^{21} \cdot A_V$ (magnitude) (Jenkins and Savage 1974). The extinction toward the SE cloud is 2–3 mag in Fig. 3.5a and is consistent with the HI self-absorption considering the contamination by the foreground stars, which tends to reduce A_V toward the Galactic plane.

In summary, we find it a reasonable interpretation that the SE cloud represents HI self-absorption associated with the SNR shell.

3.2.3.3 Analysis of the HI Self-absorption Dips

We shall briefly review some basic properties of HI gas to understand the behavior of HI brightness (e.g., Sato, Fukui 1978). The spin temperature, T_s, of HI is $\sim$100 K or higher in a warm neutral medium at particle densities of less than 10 cm^{-3}. T_s decreases with density from 100 to 10 K in a density range of 100–1,000 cm^{-3} (e.g., Fig. 2 in Goldsmith et al. 2007). The temperature decrease is mainly a result of higher shielding of stellar radiation and increased line cooling.

It is well established that HI is converted into H_2 on dust surfaces with increasing gas column density and UV shielding and that H_2 is dissociated by cosmic rays and UV photons (e.g., Allen and Robinson 1977). The equilibrium HI abundance is determined by the balance between formation and destruction of H_2, and the residual density of HI is about 10^{-2} that of H_2 in typical interstellar molecular clouds (Allen and Robinson 1977; Sato, Fukui 1978). We also note that the H_2 abundance should be time-dependent as the formation of H_2 is a slow process, of the order of 10 Myr for densities around 100 cm^{-3} (e.g., Allen and Robinson 1977).

Based on the HI–H_2 transition, we interpret the dark HI in Fig. 3.2b as representing HI with lower T_s. The CO W cloud shows a good spatial coincidence with the dark HI W cloud, as is consistent with this interpretation. The other prominent dark HI region, the SE cloud, shows no CO, and we suggest that its density is lower and its T_s is higher than that in the CO W cloud. HI brightness $T_L(V)$ is expressed as follows (e.g., Sato, Fukui 1978):

$$T_L(V) = T_s[1 - e^{-\tau(V)}] + T_L^{FG}(V) + [T_L^{BG}(V) + T_C^{BG}]e^{-\tau(V)} - (T_C^{FG} + T_C^{BG}), \quad (3.2)$$

where $T_L(V)$, T_s, $\tau(V)$, $T_L^{FG}(V)$, and $T_L^{BG}(V)$ are the observed HI brightness temperature, the spin temperature, the optical depth of cold HI in the cloud, and the foreground and background HI brightness temperature, respectively, at velocity V. T_C^{FG} and T_C^{BG} are the continuum brightness temperature at 21 cm wavelength in the foreground and background of the cloud, respectively. The radio continuum emission is weak in RX J1713.7−3946 (Lazendic et al. 2004), and T_C^{FG} and T_C^{BG} are nearly zero as compared with $T_L(V)$.

We are then able to estimate the HI column density of dark HI clouds. Figure 3.4b shows the HI self-absorption dip with the background HI emission interpolated by a straight line connecting the two shoulders at 0 and 20 km s^{-1}. This gives a conservative estimate because the actual background HI shape perhaps has a more intense peak at -10 km s^{-1}, as seen in the northern area of the SNR. The spin temperature T_s of the dark HI gas is an unknown parameter. From the lowest HI brightness at the bottom of the dip in Fig. 3.4b, we estimate T_s to be less than $\sim$55 K and higher than $\sim$20 K, where the temperature of the CO clouds is $\sim$10 K (see Sect. 2.3.1). We estimate the absorbing dark HI column density to be $N_p(\mathrm{HI}) = 1.0 \times 10^{21}$ cm^{-2} (optical depth = 0.8), 1.8×10^{21} cm^{-2} (optical depth = 1.1), and 3.1×10^{21} cm^{-2} (optical depth = 1.5) for the three assumed cases of T_s = 30, 40, and 50 K, respectively, for the half-power line width $\Delta v = 10$ km s^{-1}, where the HI optical depth $\bar{\tau}$ is estimated from Eq. 3.2 and N_p(HI) by the following relationship:

$$N_{\rm p}({\rm H\,I})\ ({\rm cm}^{-2}) = 1.823 \times 10^{18}\ T_s\ ({\rm K})\ \Delta v\ ({\rm km\ s}^{-1})\ \bar{\tau}. \tag{3.3}$$

We shall here adopt $T_{\rm s} = 40\,{\rm K}$ and a corresponding dark HI optical depth of 1.1. A higher $T_{\rm s}$ affords a higher optical depth and vice versa. The relatively large optical depth of around 1 is consistent with the fairly flat HI dip in Fig. 3.4b, which suggests weak saturation. We also tested the effects of elevating the background HI by 15 K and found a small change of $5 \times 10^{20}\,{\rm cm}^{-2}$. The error is mainly introduced by the straight-line approximation and uncertainty in $T_{\rm s}$ of $\sim$10 K. We infer that the dark HI column density is accurate within a systematic error of $\sim 1 \times 10^{21}\,{\rm cm}^{-2}$.

The average HI density in the SE cloud is roughly estimated to be $150\,{\rm cm}^{-3}$ by dividing $1.8 \times 10^{21}\,{\rm cm}^{-2}$ by $\sim$4 pc, the line-of-sight length of the thick ISM shell, following the three-dimensional (3D) model described in Sect. 3.2.5. This density is significantly lower than the critical density for collisional excitation of the ^{12}CO (J = 1–0) transition, $\sim 1000\,{\rm cm}^{-3}$, which is consistent with no CO emission from the SE cloud and with low spin temperature around 40 K.

We also extend this analysis to the regions with narrow HI dips associated with CO emission, where we adopt $T_{\rm s} = 10\,{\rm K}$, the kinetic temperature of the CO gas. The small dips in these regions indicate that the HI optical depth is generally as low as $\sim$0.1, reflecting a small fraction of the residual HI in the CO gas. We show the distributions of the peak optical depth of the HI self-absorption in Fig. 3.6a, and the derived total HI column density distribution, the sum of the HI in emission, and self-absorption in Fig. 3.6b, where the SE cloud is significant. We shall hereafter refer to the dark HI of $T_{\rm s} = 40\,{\rm K}$ as "cool HI" and that of $T_{\rm s} = 10\,{\rm K}$ as "cold HI".

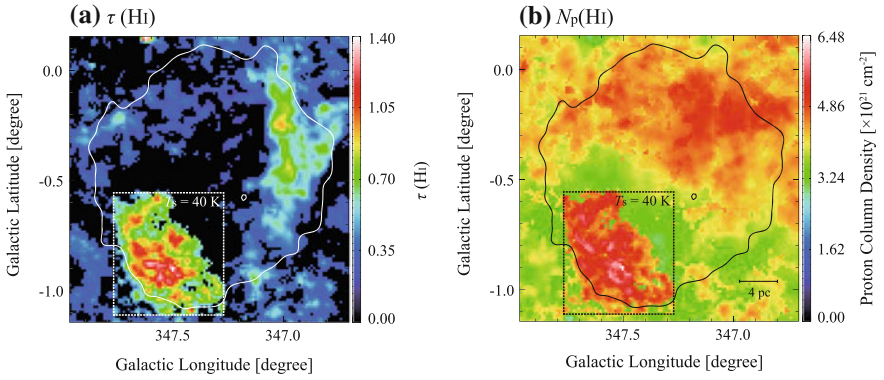

Fig. 3.6 **a** Distribution of peak optical depth of the HI self-absorption. **b** Distribution of atomic proton column density, $N_{\rm p}$(HI), estimated for the HI emission and self-absorption. The velocity both figures ranges from -20 to $0\,{\rm km\,s}^{-1}$. Contours show the H.E.S.S. VHE γ-ray distribution (Aharonian et al. 2007) and are plotted at 20 smoothed counts. We assume spin temperatures $T_{\rm s}$ of 40 and 10 K, inside and outside the *dotted box* toward the SE cloud, respectively

3.2.4 Total ISM Protons

The number of total ISM protons in the SNR is given by summing up the three components in the velocity range from -20 to $0\,\mathrm{km\,s^{-1}}$: H_2 derived from ^{12}CO(J = 1–0), dark HI (dips), and warm HI (emissions). The results are shown as spatial distributions in Fig. 3.7. Figure 3.7a, b, c and d show $N_\mathrm{p}(H_2)$, N_p(HI), $N_\mathrm{p}(H_2$+HI), and VHE γ-rays, respectively. We see that the total ISM protons $N_\mathrm{p}(H_2$+HI) show a shell-like shape similar to the VHE γ-rays, which significantly improves the correlation with the γ-rays as compared with the case of molecular gas only. We therefore conclude that the contribution of HI in addition to that of H_2 in counting the ISM protons is critical. We find that in the south, the total ISM protons are dominated by the atomic gas, whereas in the north, the molecular and atomic protons are both important. A more quantitative comparison will be given in Sect. 3.2.5.2. Diagrams

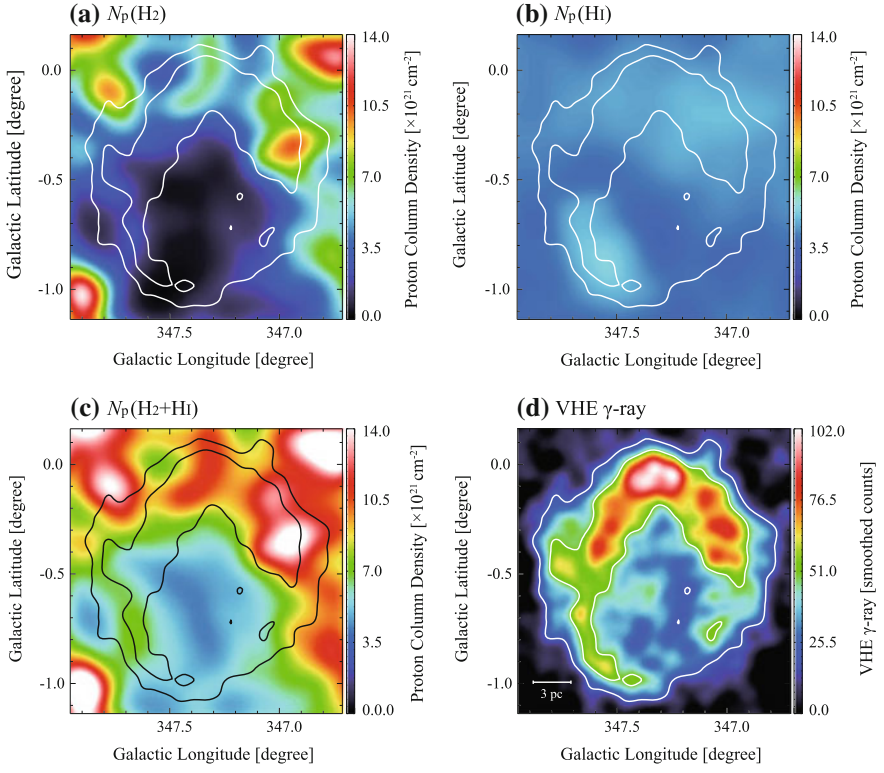

Fig. 3.7 **a** Distributions of the column density of ISM protons N_p estimated from ^{12}CO(J = 1–0) $N_\mathrm{p}(H_2)$, **b** HI emission with correction for the HI self-absorption N_p(HI), and **c** sum of $N_\mathrm{p}(H_2)$ and N_p(HI). All the data sets used here are smoothed to an HPBW of VHE γ-ray distribution with a Gaussian function. **d** VHE γ-ray distribution. Contours are plotted every 50 smoothed counts from 20 smoothed counts

of the total ISM protons similar to Fig. 3.7 are presented for the optically thin case for reference in Figure C1 in Appendix C, wherein the shell-like distribution toward the SE cloud is missing.

3.2.5 *γ-rays and the ISM Protons*

3.2.5.1 γ-ray Distribution

The VHE γ-ray distribution obtained by H.E.S.S. is a nearly circular-symmetric shell with some elliptical elongation in the north–south direction. To gain an insight into the distribution of the γ-ray emissivity, we undertake a simple analysis of the γ-ray distribution. We adopt an elliptical annular ring in the analysis, unlike (Aharonian et al. 2006a, b), who made a similar analysis using a circular annular ring in the correlation of γ-rays and NANTEN CO intensity (see their Fig. 17).

We estimated the radius of the γ-ray shell, as defined as the half-intensity level of the peak γ-ray smoothed count, every 15° for an assumed center. We averaged the radii in various angular directions and minimized the sum of the squares of the deviation from the average. This process gives a central position at $(l, b) = (347.^{\circ}34, -0.^{\circ}52)$. For this central position, we plotted the radius every 15° and found that a sinusoidal distribution is a reasonable approximation, as expected. Fitting this plot using a sinusoidal curve, we found that the shell is approximated by an elliptical shape with an aspect ratio of 1.1 whose major axis is almost in the north–south direction. This elliptical shape is adopted in Fig. 3.8a.

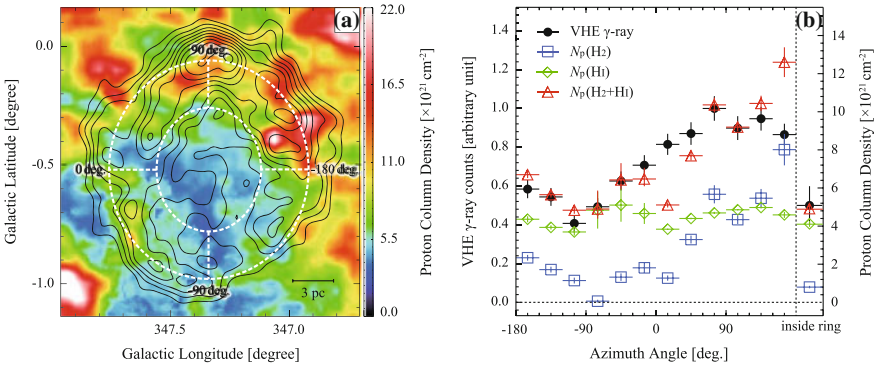

Fig. 3.8 **a** Distributions of the column density of the total ISM protons $N_{\rm p}({\rm H_2+HI})$ in a velocity range from −20 to 0 km s^{-1}. Contours are the same as those in Fig. 3.1a. **b** Azimuthal distributions of $N_{\rm p}({\rm H_2})$, $N_{\rm p}({\rm HI})$, $N_{\rm p}({\rm H_2+HI})$, and VHE γ-ray smoothed counts per beam between the *two elliptical rings* shown in (**a**). The proton column densities are averaged values between the rings (see the text). Semi-major and semi-minor radii of the *outer ring* are $0.^{\circ}46$ and $0.^{\circ}42$, respectively, and the radii of the *inner ring* are half of these. The same plots inside the *inner ring* are shown on the *right-hand side* of (**b**)

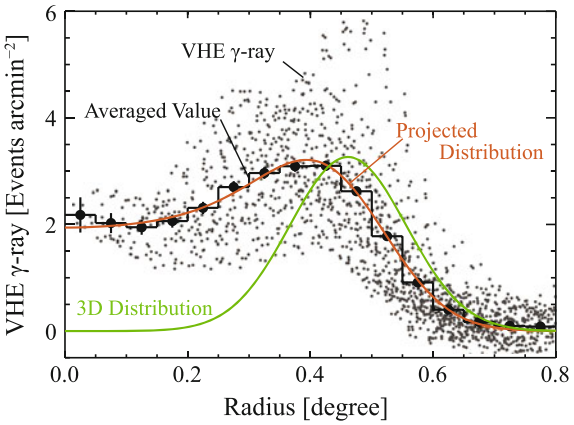

Fig. 3.9 Radial distribution of the VHE γ-ray radiation. *Small dots* show the distributions of all the H.E.S.S. data points and *large filled circles* with error bars show averaged values at each radius. We assume a 3D spherical shell with a Gaussian-like intensity distribution along its radius to approximate the VHE γ-ray distribution (see the text). The *green line* shows the estimated 3D Gaussian distribution, and the *red line* shows its projected distribution. The peak radius and the full width at half maximum of the *green line* are estimated to be $0.^{\circ}46$ ($\sim$ 8.0 pc) and $0.^{\circ}24$ ($\sim$ 4.2 pc), respectively

Figure 3.9 shows the radial scatter of γ-ray smoothed counts and an averaged value shown by a step function in radius r for every $0.^{\circ}05$. We also adopted an elliptical shape in this case and normalized its radius to that of the major axis using elliptical modification. After several trials of different functional forms, we found that a Gaussian radial distribution of the γ-ray emissivity per volume well reproduces the projected radial distribution in Fig. 3.9. In this fitting we have two free parameters of the Gaussian shape: the peak radius r_0 and the sigma σ, which are expressed as follows:

$$F(r) = A \times e^{-(r-r_0)^2/2\sigma^2}, \tag{3.4}$$

where A is a normalization coefficient. By requiring that the error in the fitting becomes minimum in the projected distribution shown by the step function, we found that $r_0 = 0.^{\circ}46$ and $\sigma = 0.^{\circ}10$ afford the best fit, as shown in Fig. 3.9. This distribution shows that the observed shell is consistent with a shell of a half-intensity thickness $\sim 0.^{\circ}24$ with nearly zero emissivity toward the center. This analysis indicates that the γ-rays are mainly emitted in a thick shell of 8.0 pc radius and 4.2 pc width at the half-intensity level with nearly zero emissions from the inner part. A similar thick-shell model was also obtained by (Aharonian et al. 2006a, b). Numerical modeling of the γ-ray emission has been undertaken by several authors, and these studies indicate that γ-ray emission has a rather steep gradient beyond the peak of the shell in either the leptonic or hadronic scenarios (e.g., Jun and Norman 1996; Zirakashvili and Aharonian 2010). The fitting to the H.E.S.S. data above shows that the gradient

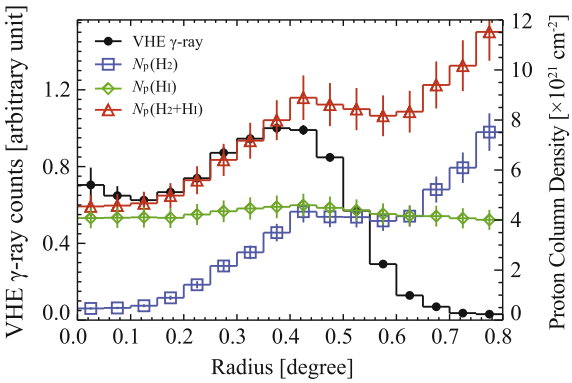

Fig. 3.10 Radial distributions of averaged values of VHE γ-ray radiation, $N_p(H_2)$, N_p(HI), and $N_p(H_2+HI)$. $N_p(H_2)$ and N_p(HI) show column densities estimated from $^{12}CO(J = 1–0)$ and HI, respectively, and $N_p(H_2+HI)$ shows the total ISM proton column density

in the γ-ray distribution is not so steep toward the outside, which may be due to smearing in space from averaging. We shall not try a further elaborated analysis here due to the limiting angular resolution of H.E.S.S. of $0.^{\circ}14$ (FWHM).

Figure 3.10 shows that the projected radial distribution of ISM protons follows a fairly similar distribution to the γ-rays inside the SNR. This is consistent with the ISM distribution also being shell-like with an inner cavity, which is consistent with the stellar wind shell discussed in Sect. 3.3.1; if the ISM has no cavity in its inner part, the projected distribution of the ISM should increase toward the center. We shall assume hereafter that the ISM distribution is also approximated by the same Gaussian shape as the γ-rays with a radius of 8.0 pc and a thickness of 4.2 pc at the half-intensity level.

3.2.5.2 Comparison Between the γ-rays and the ISM Protons

In the hadronic scenario, the target distribution should be correlated with the γ-ray distribution for a uniform cosmic ray distribution. This correlation should be seen inside the shell of the SN shock, which has a sharp gradient beyond its outer radius. We expect that the ISM protons are distributed beyond the outermost edge of the shell where cosmic ray protons cannot reach via diffusion. Beyond the SNR shock, the γ-ray emission profile may be influenced by components from the diffuse cosmic ray background and by the energy dependent transport of escaping cosmic rays from RX J1713.7−3946 into the clumpy ISM (e.g., Gabici et al. 2009; Casanova et al. 2010a, b). We are able to avoid possible effects of such a cutoff by taking a radius of correlation analysis well within the SNR shell, where the cosmic ray protons do not decrease in energy density.

The ISM proton distribution is shown in Fig. 3.8a with the two annular elliptical rings along the shell, where the size of the outer ring was chosen to meet the above requirements. Figure 3.8b shows a comparison between the ISM protons and γ-rays at the position angle shown in Fig. 3.8a, where the vertical scale is adjusted so that

the correspondence with the VHE γ-rays becomes optimum. Here, the error in the VHE γ-ray emission from the publicly available H.E.S.S. image is approximately (smoothed counts)$^{0.5}$. In Fig. 3.8b, the uncertainty in the dark HI in the SE cloud, 1×10^{21} cm^{-2}, is of the order of 10–20% of the total. The total ISM proton density shows good agreement with the VHE γ-ray angular distribution as well as with the central part of the inner ring. We recall that CO alone showed a marked deficiency toward the SE cloud as compared with the γ-rays (see Fig. 17 of Aharonian et al. 2006a, b). The present analysis indicates that this deficiency is recovered by including HI and shows that the total gas of both atomic and molecular components has a good correlation with the VHE γ-rays in the annular ring. The total mass of the ISM protons responsible for the γ-rays is 2.0×10^4 $M_\odot$ over the entire SNR (radius $0.^\circ65$); the mass of molecular protons is 0.9×10^4 $M_\odot$ and that of atomic protons is 1.1×10^4 $M_\odot$, where we assume that the ISM protons interacting with the cosmic ray protons are proportional to the VHE γ-rays (Sect. 3.2.5.1, Fig. 3.10).

There are two points in Fig. 3.8b for which additional remarks may be appropriate. One is the point at an azimuth angle of 115°, which may be estimated too low owing to the lack of correction for the self-absorption because of the large velocity shift in the expanding shell (see Figure B1). Another is the point at an azimuth angle of 165°, where the strong CO emission (peak A after Fukui et al. 2003) increases the proton column density, although the increased protons may not be interacting with the cosmic ray protons beyond the SNR shock, leading to fewer γ-rays.

An independent test is conducted by examining the radial distribution of the ISM protons shown in Fig. 3.10, where an average taken over the same binning as the γ-rays in Fig. 3.9 is shown by a step function and the total ISM protons and γ-rays are superposed with the same proportional factor as that adopted in Fig. 3.8. Here, the error in the VHE γ-ray emission is approximately (oversampling-corrected total smoothed count)$^{0.5}$ normalized to 1 arcmin^2. We see that the $N_{\rm p}$(H_2+HI) and γ-rays show good agreement inside the shell and that the γ-rays sharply decrease outside the shell. This offers another presentation of the good correlation between the γ-rays and the ISM protons.

We argue that the apparent anti-correlation between the HI brightness at the bottom of the dips and the γ-rays in the SE cloud (Fig. 3.4) is consistent with the HI dips being caused by cool and dense HI gas. The anti-correlation is interpreted as being caused by the spin temperature $T_{\rm s}$ of HI decreasing with density (Sect. 3.2.3.3) and the γ-rays increasing with the ISM proton density locally in the SE cloud, demonstrating a detailed correspondence between the γ-rays and the ISM protons that is mainly atomic. The small and narrow HI dips in the W and N clouds have the HI column density of less than 10^{20} cm^{-2}, which is significantly lower than the typical molecular column density by two orders of magnitude. Thus, in most of the regions aside from the SE cloud, the HI column density is dominated by emission but not by self-absorption. For the sake of reference, we show a set of similar diagrams of ISM proton distributions for the optically thin case in Figures C2 and C1 in Appendix C, corresponding to Figs. 3.8 and 3.10, respectively.

Before concluding this Chapter, we cautiously note that the cool/cold HI cannot be estimated accurately if it is optically thick, it lies behind an optically thick foreground

HI in the line of sight, or if the background HI profile has a different shape from that of its neighbors. Such effects, while posing intrinsic limits for probing cool/cold HI, are relatively unimportant for nearby objects at a distance of 1 kpc or less, where foreground HI is not important. The dark HI W and SE clouds are probably good examples of where the cool/cold HI is well traced by the low HI brightness, whereas the N cloud with higher HI brightness may be partially affected by the foreground HI in the line of sight.

3.3 Discussion

3.3.1 The Evacuated Cavity by the Stellar Wind

It is likely that the CO shell in Fig. 3.1b was formed over a timescale of Myr by the stellar wind of the progenitor, an OB star that exploded as an SN 1,600 yr ago. The total velocity span of the CO shell, $\sim$20 km s^{-1}, is much smaller than the SN shock speed and indicates that it requires $\sim$1 Myr to form the shell of the ISM, as is roughly estimated by dividing the radius of 9 pc by 10 km s^{-1}. Molecular gas expanding at 10 km s^{-1} can move only 0.01 pc in 1,000 yr. Therefore, the current CO distribution has been little affected by the SN explosion (SNe) and holds the initial conditions before the shock interaction.

While a stellar-wind shell with a known central star is not often observed elsewhere, such examples include the Pegasus loop found in ^{12}CO(J = 1–0), HI, and dust emission at (l, b) = (109°, −45°) centered on runaway star HD886 (B2 IV) (Yamamoto et al. 2006). The Pegasus loop is located at $\sim$100 pc in a relatively uncontaminated environment outside the Galactic plane. No SNe has yet occurred in this shell. A comparison between RX J1713.7−3946 and the Pegasus loop is given in Table 3.1. In the Pegasus loop, the swept-up shell of the ISM has a width of $\sim$5 pc for a radius of $\sim$18 pc and a total mass of $\sim$1500 $M_\odot$. The shell is mostly atomic and comprises 78 smaller ^{12}CO(J = 1–0) clumps (see Fig. 10 in Yamamoto et al. 2006). The clumped CO is a natural outcome of thermal/gravitational instability and seems common in such a shell. The shell is expanding at a total velocity span of 15 km s^{-1}. The HI density inside the shell is $\sim$1 cm^{-3} in the north, where the stellar wind evacuated the ISM over 1 Myr. The Pegasus loop is located in a somewhat lower-density environment than RX J1713.7−3946 and offers an insight into the initial condition of the ISM prior to the SNe in RX J1713.7−3946.

Inoue et al. (2009, 2012), performed numerical simulations of the hydrodynamical interaction between a shock wave and the highly inhomogeneous neutral gas to model the interaction in RX J1713.7−3946. The SN in RX J1713.7−3946 exploded in a cavity with average density less than 1 cm^{-3} (e.g., Zirakashvili and Aharonian 2010; Morlino et al. 2009; Berezhko and Völk 2008) and a dense shell with CO clumps remaining more or less as they were prior to the SNe. The SN shock front moves almost freely at $\geq$3000 km s^{-1} in the cavity in the early phase of $\sim$1000 yr and begins

Table 3.1 A comparison between RX J1713.7−3946 and the Pegasus Loop

	RX J1713.7−3946[a]	Pegasus Loop[b]
Distance (kpc)	1	0.1
Diameter (pc)	17.4	25
Total mass of the ISM ($M_\odot$)	∼20000[c]	∼1500
Thickness of the ISM shell (pc)	∼4.2	∼5
Peak brightness of HI (K)	∼170	∼40
Line width of HI ($\mathrm{km\,s^{-1}}$)	∼20	∼16
Expansion velocity of the gaseous shell ($\mathrm{km\,s^{-1}}$)	∼10	∼7–9
Spectral type of the progenitor	B1 V/B0 V[d]	B2 IV

Notes. The Pegasus loop may comprise two shells and the mass should be regarded as an upper limit (Yamamoto et al. 2006)
[a]Fukui et al. (2003), Moriguchi et al. (2005)
[b]Yamamoto et al. (2006)
[c]Present work
[d]Cassam-Chenaï et al. (2004)

to interact with the dense and thick clumpy ISM wall swept-up by the stellar wind only in the last few 100 yr. The γ-ray shell is not strongly deformed, although we see some deviations on a pc scale from a perfect circular shell, suggesting effects of recent dynamical interaction.

The interaction between the molecular clumps and the shock wave is observed as an X-ray enhancement around the dense molecular clumps at spatial resolutions higher than 0.5 pc (see Chap. 2). This showed that the molecular clump peak C is rim-brightened in X-rays, suggesting that it is a dense clump overtaken by the shock, and that peak A (Fukui et al. 2003) is X-ray-brightened only toward its inner edge, indicating the shock interaction at the inner boundary of peak A. Inoue et al. (2012) showed that the initial magnetic field B of 1 μG is amplified to 0.1–1 mG near the dense clumps by the enhanced turbulence driven by the shock. The stronger magnetic field explains the X-ray enhancement as being caused by either an enhanced synchrotron emission proportional to B^2 or by increased acceleration. Inoue et al. (2012) also showed that the shock speed v_s is significantly reduced locally with density n ($\mathrm{cm^{-3}}$) such that $v_s \sim 3000\,\mathrm{km\,s^{-1}}/\sqrt{n/n_0}$, where $n_0 = 1\,\mathrm{cm^{-3}}$. This dependence of v_s on density can explain the absence of thermal X-rays in the SNR because the molecular gas is too dense to be affected by the shock to emit thermal X-rays (Inoue et al. 2012). A uniform lower-density case with significant thermal X-rays arising from shock heating is presented by Ellison et al. (2010), but such a model is not applicable to the highly inhomogeneous ISM of RX J1713.7−3946 (Inoue et al. 2012 also see the discussion in Sect. 4 of Ellison et al. 2010). The above picture is consistent with peak C, having density greater than $10^4\,\mathrm{cm^{-3}}$ (see Sect. 2.3.2), and therefore surviving without erosion.

3.3.2 γ-ray Emission Mechanism

VHE γ-rays are emitted via two mechanisms: leptonic or hadronic process. The leptonic process explains γ-ray creation via the inverse Compton effect between cosmic ray electrons and low energy photons. In the hadronic scenario, γ-rays are emitted by the decay of neutral pions produced in the high energy reactions between cosmic ray protons and ISM protons. DSA is the most widely accepted scheme of particle acceleration (e.g., Bell 1978; Blandford and Ostriker 1978; Jones, Ellison 1991; Malkov and Drury 2001). The previous works on RX J1713.7−3946 show that the observed spectral energy distribution of γ- and X-rays is explained by either the leptonic and/or hadronic mechanisms if DSA works to accelerate the particles (Aharonian et al. 2006a, b; Porter et al. 2006; Katz and Waxman 2008; Berezhko and Völk 2008; Ellison and Vladimirov 2008; Tanaka et al. 2008; Morlino et al. 2009; Acero et al. 2009; Ellison et al. 2010; Patnaude et al. 2010; Zirakashvili and Aharonian 2010; Abdo et al. 2011; Fang et al. 2011).

In the hadronic scenario, wherein neutral pion decay determines the γ-rays via proton–proton reactions, the average density of the target protons is constrained by the total energy of cosmic ray protons. An average target density greater than $0.1\,\mathrm{cm}^{-3}$ is required to produce cosmic ray protons with a total energy of 10^{51} erg for the maximum energy of SNe, whereas higher target density is required to obtain lower cosmic ray proton energy. In the leptonic scenario, where the inverse Compton process produces γ-rays, the critical parameter is the magnetic field, which constrains the synchrotron loss timescale of cosmic ray electrons; a magnetic field of the order of 10 μG is usually required (e.g., Tanaka et al. 2008).

We here argue that the highly inhomogeneous distribution of the ISM, the cavity, and the dense and clumpy wall opens the possibility of accommodating the low-density site for DSA and the high-density target simultaneously, as discussed in detail by (Inoue et al. 2012). A similar argument on the hadronic interaction between cosmic ray protons and the ambient dense clouds has been presented by Zirakashvili and Aharonian (2010). In this picture, the cosmic rays are first accelerated via DSA in the low-density cavity, after which the cosmic ray protons reach and react with the target protons in the dense wall to produce γ-rays. The main energy range of the cosmic ray protons required for hadronic VHE γ-rays is 10–800 TeV (Zirakashvili and Aharonian 2010). The penetration depth, l_{pd}, of cosmic rays is expressed as follows (Inoue et al. 2012):

$$l_{\mathrm{pd}} \sim 0.1\eta^{1/2}\left(\frac{E}{10\ \mathrm{TeV}}\right)^{1/2}\left(\frac{B}{100\ \mu\mathrm{G}}\right)^{-1/2}\left(\frac{t_{\mathrm{age}}}{10^3\ \mathrm{yr}}\right)^{1/2}\ (\mathrm{pc}) \qquad (3.5)$$

where E, B, and t_{age} are the particle energy, magnetic field, and age of the SNR, respectively. The parameter η is the so-called "gyro-factor" and it has some ambiguity. In the SNR, it is reasonable to consider $\eta \sim 1$ at least around the cloud (Uchiyama et al. 2007). Thus, the penetration depth of the protons in the above energy range is 0.3–2.8 pc for the magnetic field of 10 μG and 0.1–0.9 pc for 100 μG in a typical

timescale of $\sim 10^3$ yr. The penetration depth of the cosmic ray electrons is determined by setting $t_{\rm age}$ equal to the synchrotron loss timescale (e.g., Tanaka et al. 2008) in Eq. 3.6 and it becomes energy-independent for the X-ray emitting electrons of 1–40 TeV as follows:

$$l = 0.026\,\eta^{1/2}\left(\frac{B}{100\ \mu\mathrm{G}}\right)^{-3/2}\ (\mathrm{pc}). \tag{3.6}$$

We estimate l to be from 0.8 pc for 10 μG to 0.026 pc for 100 μG if $\eta = 1$. Cosmic ray protons can therefore reach and penetrate into the dense gas within a pc scale of the acceleration site to produce VHE γ-rays, whereas the cosmic ray electrons stay relatively closer to the acceleration site, in particular, close to the dense gas with a strong magnetic field. This offers an explanation of the hadronic γ-ray production, and the correlation between the γ-rays and target protons in Figs. 3.4, 3.8, and 3.10 is a natural outcome of the scenario (Inoue et al. 2012). Gabici et al. (2007) discussed the importance of the energy-dependent interaction between cosmic ray protons and molecular clouds, and Zirakashvili and Aharonian (2010) discussed that the γ-ray spectrum may not distinguish the leptonic and hadronic scenarios in case of RX J1713.7−3946 due to such energy dependence. Recent *Fermi* Large Area Telescope (LAT) observations showed that the GeV spectrum of RX J1713.7−3946 is a hard spectrum, similar to what is expected in the leptonic scenario, and Abdo et al. (2011) discussed how the hard spectrum may favor the leptonic scenario. Inoue et al. (2012), however, argued that the hard *Fermi* LAT GeV spectrum is also well explained by the hadronic scenario as resulting from the energy-dependent penetration of cosmic ray protons into the dense clouds and that the leptonic scenario is not a unique explanation of this spectrum. Inoue et al. (2012) confirmed that the γ-ray spectrum becomes similar under both leptonic and hadronic scenarios and is not usable for distinguishing the two scenarios, as noted by Zirakashvili and Aharonian (2010), and concluded that the hadronic origin is testable only by comparing the γ-ray distribution with the ISM target distribution. The present results demonstrate that the ISM proton distribution indeed shows a good spatial correspondence with that of the γ-rays by considering the contribution of the HI and matching it with the predictions by Zirakashvili and Aharonian (2010) and Inoue et al. (2012).

The total energy of cosmic ray protons is estimated by the relationship between the total target protons and the observed γ-rays (2–400 TeV) after extrapolating the proton spectrum to 1 GeV as follows (Aharonian et al. 2006a, b):

$$W_{\rm tot} \sim (1 - -3) \times 10^{50}\left(\frac{d}{1\,\mathrm{kpc}}\right)^{2}\left(\frac{n}{1\,\mathrm{cm}^{-3}}\right)^{-1}\ (\mathrm{erg}), \tag{3.7}$$

where the distance to the source is $d \sim 1$ kpc and the density of the target protons is n. The average density of ISM protons is calculated to be $\sim 130\,\mathrm{cm}^{-3}$ for a total ISM protons mass of $2.0 \times 10^4\ M_\odot$ over the entire SNR (radius 0.°65), as modeled in Fig. 10, and the total cosmic ray proton energy is calculated to be $\sim (0.8–2.3) \times 10^{48}$ erg using Eq. 3.7. This corresponds to $\sim 0.1\%$ of the total energy release of SNe and

may appear low. Other SNRs like W44 or W28 that are a few to tens of thousands of years old have total cosmic ray proton energies of the order of 10^{49}–10^{50} erg (Abdo et al. 2010; Giuliani et al. 2010). We might speculate that the cosmic ray protons accumulate over a few tens of thousands of years to reach more than 10 % of the SNe energy. This issue is to be further tested by examining cosmic rays escaping from SNRs (e.g., Gabici et al. 2009; Casanova et al. 2010a, b).

To summarize the discussion, we have shown that a combined analysis of CO and HI provides a reasonable candidate for the target ISM protons and thereby lends new support for the hadronic scenario. We should note that the present analysis offers one of the necessary conditions for the hadronic scenario for uniform cosmic ray proton distribution, but it is not a full verification of the hadronic scenario and does not rule out leptonic components. We need to acquire additional observations before fully establishing the hadronic scenario, including better determination of the magnetic field and higher angular resolution images of γ-rays at least comparable to that of the ISM. The Cherenkov Telescope Array will provide such images in the future. We noted that the observed highly inhomogeneous distribution of the ISM plays an essential role in γ-ray production; DSA works in a highly evacuated cavity and the accelerated cosmic ray protons travel over a pc to interact with the surrounding dense ISM protons. It is important to develop a similar analysis of both HI and CO in the other similar objects such as RX J0852.0−4622 (Vela Jr.), RCW 86, and HESS J1731−347. Such works are in progress based on the NANTEN2 observations and high-resolution HI interferometry.

3.4 Conclusions

We summarize the main conclusions as follows:

1. A new analysis of CO and HI has revealed that the VHE γ-ray SNR RX J1713.7−3946 is associated with a significant amount of HI gas without H_2 derived from CO. This HI gas is relatively dense and cold and is detectable mainly as HI emission. We have also identified regions where HI is observed as dark HI in self-absorption dips and derived the total ISM proton column density over the SNR. HI plus H_2, or total ISM protons, provides one of the necessary conditions (target protons) for hadronic origin of the γ-rays. Such target ISM protons have not been identified in the previous study that considered only H_2, although the present findings alone do not exclude a leptonic origin.
2. For an annular pattern around the VHE γ-ray shell, we compared the total ISM proton distribution with the VHE γ-ray distribution and found that they show reasonably good correspondence and vary by similar factors. The inclusion of the atomic protons observed as the HI self-absorption dips is essential particularly in the southeast of the γ-ray shell. The interpretation of HI self-absorption dips is also supported by the enhanced optical extinction toward the southeastern rim.

3. The cavity surrounding the SNR was created by the stellar wind of the SN progenitor. The inside of the cavity is of low density with $<1\,\mathrm{cm}^{-3}$, whereas the cavity wall comprises the dense and clumpy atomic or molecular target protons of $\geq$100–1000 cm^{-3}. The DSA in the highly inhomogeneous ISM offers a reasonable mechanism of particle acceleration in the low-density cavity and the dense wall acts as the target for γ-ray production by the cosmic ray protons. Hydrodynamical numerical simulations of the interaction have shown detailed physical processes involved (Inoue et al. 2012).
4. Considering the other pieces of observational and theoretical works accumulated thus far, the present results make the hadronic interpretation much more comfortable in RX J1713.7−3946. The current total energy of cosmic ray protons is estimated to be $\sim 10^{48}$ erg, 0.1% of the total energy of SNe, if we assume that the γ-rays are all produced by the hadronic process.

References

A.A. Abdo, M. Ackermann, M. Ajello et al., Science **327**, 1103 (2010)
A.A. Abdo, M. Ackermann, M. Ajello, A. Allafort, L. Baldini, J. Ballet et al., Astrophys. J. **734**, 28 (2011)
F. Acero, J. Ballet, A. Decourchelle, M. Lemoine-Goumard, M. Ortega, E. Giacani et al., Astrophys. J. **505**, 157 (2009)
M. Ackermann, M. Ajello, A. Allafort, E. Antolini, L. Baldini, J. Ballet et al., Astrophys. J. **756**, 4 (2012)
F. Aharonian, A.G. Akhperjanian, A.R. Bazer-Bachi, M. Beilicke, W. Benbow, D. Berge et al., Astrophys. J. **636**, 777 (2006a)
F. Aharonian, A.G. Akhperjanian, A.R. Bazer-Bachi, M. Beilicke, W. Benbow, D. Berge et al., Astronom. Astrophys. **449**, 223 (2006b)
F. Aharonian, A.G. Akhperjanian, A.R. Bazer-Bachi, M. Beilicke, W. Benbow, D. Berge et al., Astronom. Astrophys. **464**, 235 (2007)
M. Allen, G.W. Robinson, Astrophys. J. **212**, 396 (1977)
A.R. Bell, Mon. Notice. R. Astronom. Soc. **182**, 147 (1978)
E.G. Berezhko, H.J. Völk, Astronom. Astrophys. **492**, 695 (2008)
D.L. Bertsch, T.M. Dame, C.E. Fichtel, S.D. Hunter, P. Sreekumar, J.G. Stacy et al., Astrophys. J. **416**, 587 (1993)
R.D. Blandford, J.P. Ostriker, Astrophys. J. **221**, L2 (1978)
S. Casanova, F.A. Aharonian, Y. Fukui, S. Gabici, D.I. Jones, A. Kawamura et al., Publicat. Astronom. Soc. Jpn. **62**, 769 (2010a)
S. Casanova, D.I. Jones, F.A. Aharonian, Y. Fukui, S. Gabici, A. Kawamura et al., Publicat. Astronom. Soc. Jpn. **62**, 1127 (2010b)
G. Cassam-Chenaï, A. Decourchelle, J. Ballet, J.-L. Sauvageot, G. Dubner, E. Giacani et al., Astronom. Astrophys. **427**, 199 (2004)
J.M. Dickey, F.J. Lockman, Annu. Rev. Astronom. Astrophys. **28**, 215 (1990)
K. Dobashi, H. Uehara, R. Kandori, T. Sakurai, M. Kaiden, T. Umemoto et al., Publicat. Astronom. Soc. Jpn. **57**, 1 (2005)
D.C. Ellison, A. Vladimirov, Astrophys. J. **673**, L47 (2008)
D.C. Ellison, D.J. Patnaude, P. Slane, J. Raymond, Astrophys. J. **712**, 287 (2010)
J. Fang, Y. Tang, L. Zhang, Astrophys. J. **731**, 32 (2011)

Y. Fukui, Y. Moriguchi, K. Tamura, H. Yamamoto, Y. Tawara, N. Mizuno et al., Publicat. Astronom. Soc. Jpn. **55**, L61 (2003)
Y. Fukui, ed. by F.A. Aharonian, W. Hofmann, F. Rieger in *AIP Proceedings of 4th International Meeting on High-Energy Gamma-Ray Astronomy*, vol. 1085, p. 104 (Melville, NY: AIP, 2008)
Y. Fukui, A. Kawamura, Annu. Rev. Astronom. Astrophys. **48**, 547 (2010)
S. Gabici, F.A. Aharonian, P. Blasi, Astronom. Astrophys. Suppl. **309**, 365 (2007)
S. Gabici, F.A. Aharonian, S. Casanova, MNRAS **396**, 1629 (2009)
A. Giuliani, M. Tavani, A. Bulgarelli, E. Striani, S. Sabatini, M. Cardillo et al., Astronom. Astrophys. **516**, L11 (2010)
P.F. Goldsmith, D. Li, M. Krčo, Astrophys. J. **654**, 273 (2007)
I.A. Grenier, J.-M. Casandjian, R. Terrier, Science **307**, 1292 (2005)
T. Inoue, R. Yamazaki, S.-I. Inutsuka, Astrophys. J. **695**, 825 (2009)
T. Inoue, R. Yamazaki, S.-I. Inutsuka, Y. Fukui, Astrophys. J. **744**, 71 (2012)
E.B. Jenkins, B.D. Savage, Astrophys. J. **187**, 243 (1974)
F.C. Jones, D.C. Ellison, SSRv. **58**, 259 (1991)
B.-I. Jun, M.L. Norman, Astrophys. J. **465**, 800 (1996)
B. Katz, E. Waxman, JCAP. **01**, 018 (2008)
M. Krčo, P.F. Goldsmith, Astrophys. J. **724**, 1402 (2010)
J.S. Lazendic, P.O. Slane, B.M. Gaensler, S.P. Reynolds, P.P. Plucinsky, J.P. Hughes, Astrophys. J. **602**, 271 (2004)
M.A. Malkov, L. O'C Drury, RPPh. **64**, 429 (2001)
N.M. McClure-Griffiths, J.M. Dickey, B.M. Gaensler, A.J. Green, M. Haverkorn, S. Strasser, Astrophys. J. **158**, 178 (2005)
Y. Moriguchi, K. Tamura, Y. Tawara, H. Sasago, K. Yamaoka, T. Onishi et al., Astrophys. J. **631**, 947 (2005)
G. Morlino, E. Amato, P. Blasi, Mon. Notice. R. Astronom. Soc. **392**, 240 (2009)
A. Ohama, J.R. Dawson, N. Furukawa, A. Kawamura, N. Moribe, H. Yamamoto et al., Astrophys. J. **709**, 975 (2010)
D.J. Patnaude, P. Slane, J.C. Raymond, D.C. Ellison, Astrophys. J. **725**, 1476 (2010)
Planck Collaboration, P.A.R. Ade, N. Aghanim, N. Aghanim, M. Arnaud, M. Ashdown et al., Astronom. Astrophys. **536**, A19 (2011)
T.A. Porter, I.V. Moskalenko, A.W. Strong, Astrophys. J. **648**, L29 (2006)
F. Sato, Y. Fukui, Astrophys. J. **83**, 1607 (1978)
T. Tanaka, Y. Uchiyama, F.A. Aharonian, T. Takahashi, A. Bamba, J.S. Hiraga et al., Astrophys. J. **685**, 988 (2008)
K. Torii, R. Enokiya, H. Sano, S. Yoshiike, N. Hanaoka, A. Ohama et al., Astrophys. J. **738**, 46 (2011)
Y. Uchiyama, F.A. Aharonian, T. Tanaka, T. Takahashi, Y. Maeda, Nature **449**, 576 (2007)
H. Yamamoto, A. Kawamura, K. Tachihara, N. Mizuno, T. Onishi, Y. Fukui, Astrophys. J. **642**, 307 (2006)
V.N. Zirakashvili, F.A. Aharonian, Astrophys. J. **708**, 965 (2010)

Chapter 4
Evidence for Efficient Acceleration of Cosmic Rays

As described above, supernova remnant (SNR) RX J1713.7−3946 is one of the best targets from which both non-thermal X-rays and very high energy (VHE) γ-rays are detected. In particular, it is noteworthy that the X-rays are purely non-thermal synchrotron emissions, indicating that the cosmic ray electrons are accelerated in the SNR up to the 10 TeV range. The X-ray spectra are well fitted by an absorbed power-law function of photon index $\Gamma = 2.2 - 2.4$ and an interstellar absorbing column density $N_{\rm H}$(X-ray) = 0.6-0.8$\times 10^{22}$ cm^{-2} (e.g., Cassam-Chenaï et al. 2004; Tanaka et al. 2008; Acero et al. 2009). These variations of Γ and $N_{\rm H}$(X-ray) become a key component to understanding the efficient acceleration of cosmic ray electrons. However, it is not known how the variation is formed.

We have discovered the strong connection between the interstellar medium (ISM) clumps and non-thermal X-ray distributions (see Chap. 2). In this chapter, we focus on the spectral distribution of X-rays. Specifically, we reveal the spatial distribution of photon index Γ, absorbing column density $N_{\rm H}$(X-ray), and X-ray flux in the same scale as the ISM distribution. This work aims to better understand the efficient acceleration around dense gas materials.

4.1 Observations and Data Reductions

4.1.1 X-Rays

4.1.1.1 Details of the Datasets

We analyzed the X-ray dataset archive obtained by *Suzaku* (Data Archives and Transmission System; DARTS at ISAS/JAXA). This dataset comprises 17 pointings taken in September 2005 (SWG; 3 pointings), September and October 2006

H. Sano, *Shock-Cloud Interaction in RX J1713.7–3946*,
Springer Theses, DOI 10.1007/978-4-431-55636-7_4

(AO1; 10 pointings), and February 2010 (AO4: 4 pointings), from which we primarily used 15 pointings of ON sources (see also Fig. 2.1). These data were already analyzed and published elsewhere (Takahashi et al. 2008; Tanaka et al. 2008, and Chap. 2) as summarized in Table 2.1 and Fig. 2.1.

There are two active detectors on board *Suzaku*: X-ray Imaging Spectrometer (XIS; Koyama et al. 2007) for imaging soft X-rays (0.2–12 keV) and Hard X-ray Detector (HXD; Takahashi et al. 2007) for hard X-rays (10–600 keV). In the present work, we deal with only the data taken with XIS. XIS comprises four CCDs located at the focus of the X-ray Telescopes (XRTs; Serlemitsos et al. 2007); three of these are "Front-illuminated CCDs" (FI CCD; XIS 0, 2, and 3) devices, and the other is a "back-illuminated CCD" (BI CCD; XIS 1). Spaced-row charge injection technique (SCI; Nakajima et al. 2008; Uchiyama et al. 2009) was applied only to the four pointings in February 2010. Unfortunately, XIS 2 was damaged by a micrometeorite hit on November 9, 2006 and the 2010 data in February comprise only XIS 0, 1, and 3 readings. Subsequently, Segment A of XIS 0 was found to have an anomaly on June 23, 2009 and Segment B was found to show partial charge leakage. We therefore used only the data from Segments C and D. For data processing, we used HEASoft Software version 6.11 with pipeline processing version 2.0 or 2.4 and with standard event selection criteria (cleaned event files).

4.1.1.2 Imaging

The X-ray images are those used in Fig. 2.1. Figure 4.1 shows XIS mosaic image (1–5 keV) in RX J1713.7−3946. The color scheme is in a square-root scale in 10^{-4} counts s^{-1} $pixel^{-1}$ (pixel size is $\sim 16\farcs7$) smoothed with a Gaussian kernel with full width at half maximum $\sim 45''$. This image is subtracted for the non X-ray background (NXB) and corrected for the vignetting effect produced by XRT (see Chap. 2.1.3 for further details).

4.1.1.3 Spectroscopy

The X-ray spectra of RX J1713.7−3946 is represented by the absorbed power-law model (e.g., Koyama et al. 1997). This model is used for synchrotron X-rays with photoelectric absorption and the model fitting gives three parameters: the absorbing column density $N_{\rm H}$(X-ray), the photon index Γ, and the absorption-corrected X-ray flux. We show typical X-ray spectra in Fig. 4.2. We shall explain the method used to derive the three parameters above. First, the SNR was divided into $\sim$600 regions of $2' \times 2'$ grids, wherein X-rays are significantly detected. For the $\sim$600 regions, only the data taken with FI CCD (XIS 0, 2, and 3) were used to derive X-ray spectra. In order to compare these with the data of the ISM, CO, and HI, the angular resolution was set

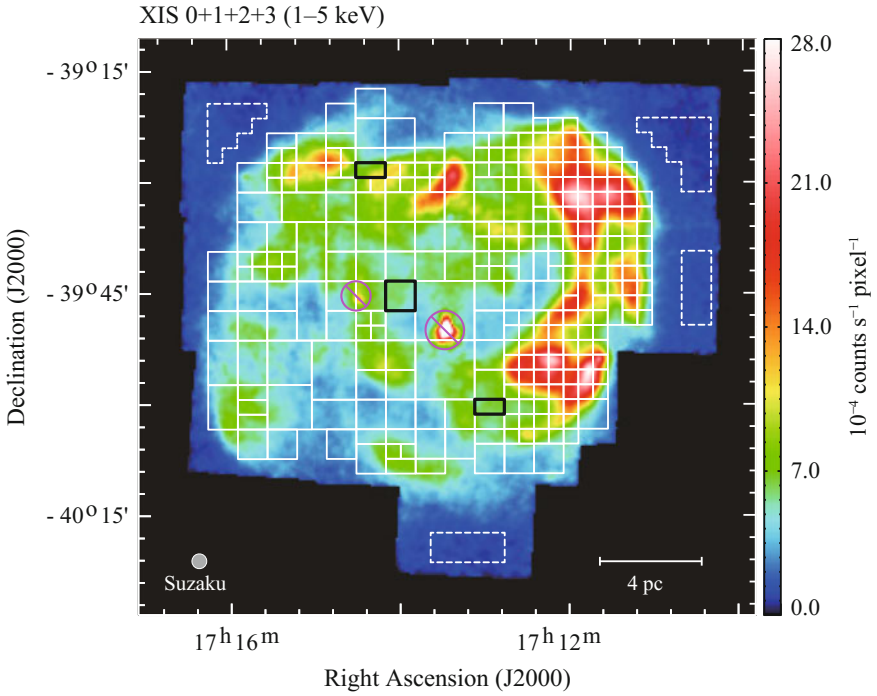

Fig. 4.1 *Suzaku* XIS mosaic image of RX J1713.7−3946 in the 1–5 keV energy band (Chap. 2.2.1). The *color scale* indicates count rate on a square-root scale and is in units of 10^{-4} counts s^{-1} $pixel^{-1}$. The *solid boxes* are those used for spectral analysis. We also show the spectra enclosed by the *black solid lines* (see also Fig. 4.2). The *dashed boxes* correspond to the regions used to extract the background spectrum. The two point sources, 1WGA J1714.4−3945 and 1WGA J1713.4−3949, are *circled* in *magenta* and those regions were removed from spectral analysis

to the highest value (*Suzaku* HPD $\sim 2'$). In addition, the background spectrum was estimated in the four regions shown in Fig. 4.1 and the western background spectrum ($\alpha_{J2000} = 17^h10^m31^s$, $\delta_{J2000} = -39°44'22.7''$) was used for every region. The two prominent point sources (1WGA J1714.4−3945 and 1WGA J1713.4−3949) in the field are excluded in the analysis. Subsequently, the spectra of each region taken with XIS 0, 2, and 3 were summed up and fit using the absorbed power-law model to generate a redistribution matrix file (RMF) by xisrmfgen and an ancillary response file (ARF) by xissimarfgen (Ishisaki et al. 2007).

Next, to reduce the statistical relative errors in absorbing column density N_H(X-ray) to less than 30%, some regions neighboring the source were summed up and their spectra were again fit by the absorbed power-law model. Figure 4.1 shows the final spectra for 305 regions, as indicated by solid boxes. About one third of the entire SNR is a square grid with a $2'$ edge (4 $arcmin^2$) and 80% of that is better than the grid with a $4'$ edge (16 $arcmin^2$). These values are much better than those in previous studies: [70% of (e.g., Cassam-Chenaï et al. 2004) is worse than the grid

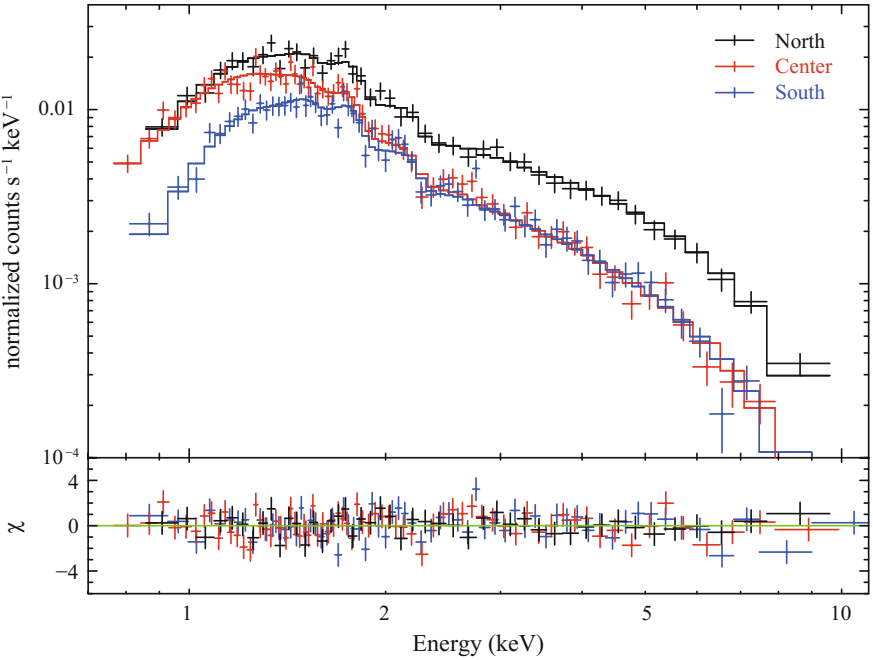

Fig. 4.2 Typical X-ray spectra of north (*black*), center (*red*), and south (*blue*) regions (for the regions definition see Fig. 4.1). The *solid lines* represent the best-fit absorbed power-law model. The lower part shows the residuals from the best-fit models. The north and center spectra can be fitted by the same absorbing column density ($N_{\rm H}$(X-ray) $\sim 0.5 \times 10^{22}$ cm^{-2}) but have a different photon index (north: $\Gamma = 2.1 \pm 0.1$, center: $\Gamma = 2.7 \pm 0.1$). The center and south spectra have the same photon index ($\Gamma = \sim$2.7) but different absorbing column densities (center: $N_{\rm H}$(X-ray) $= 0.45^{+0.06}_{-0.05} \times 10^{22}$ cm^{-2}, south: $N_{\rm H}$(X-ray) $= 0.89^{+0.09}_{-0.08} \times 10^{22}$ cm^{-2})

with a 6′ edge (36 arcmin^2)]. Each spectrum is binned to include at least 100 counts. After binning, the energy ranges below 0.4 keV and above 12 keV bins are excluded in the fitting. The best fit parameters in the fitting were used to derive absorbing column density $N_{\rm H}$(X-ray), photon index Γ, and absorption-corrected flux in 3–10 keV, $F_{3-10{\rm keV}}$, as shown in Fig. 4.3. If the background spectrum is changed to that for four to three regions, we see systematic errors of up to 10–20% in $N_{\rm H}$(X-ray). This however does not significantly affect the results in Fig. 4.3.

4.1.2 CO and HI

^{12}CO($J = 1$–0) and HI datasets are from the NANTEN Galactic Plane Survey (NGPS) and Southern Galactic Plane Survey (SGPS) taken with NANTEN and ATCA & Parkes telescopes (Moriguchi et al. 2005; McClure-Griffiths et al. 2005), respectively.

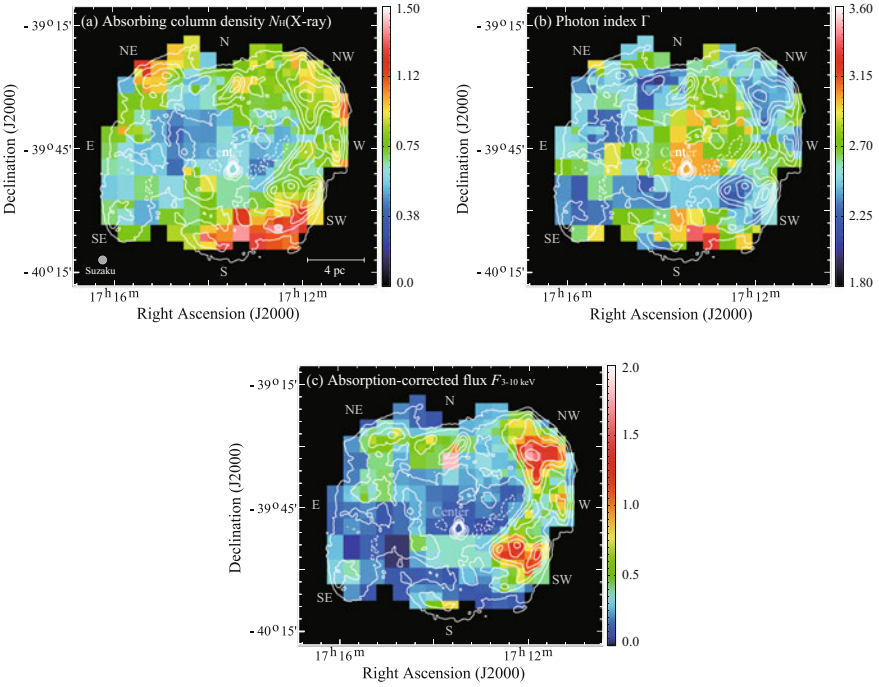

Fig. 4.3 Maps of the best-fit parameters, **a** absorbing column density N_H(X-ray), **b** photon index Γ, and **c** absorption-corrected X-ray flux $F_{3-10keV}$, for the absorbed power-law model. All maps are overlaid with smoothed contours of the *Suzaku* XIS mosaic images. The contour levels are from 3.9×10^{-4} counts s^{-1} $pixel^{-1}$ and are square-root-spaced up to 23.9×10^{-4} counts s^{-1} $pixel^{-1}$ with a pixel size of ∼16.″7. The color schemes in **a–b** and **c** are linear and square-root scale, respectively. The units are 10^{22} cm^{-2} for N_H(X-ray) and 10^{-12} erg cm^{-2} s^{-1} for $F_{3-10keV}$

The angular resolutions are HPBW ∼2.′6 for CO and ∼2.′2 for HI, similar to *Suzaku* XIS HPD ∼2′. The velocity resolutions and typical rms noise fluctuations for CO are 0.65 km s^{-1} and 0.3 k ch^{-1} and for HI are 0.82 km s^{-1} and 1.9 k ch^{-1}, respectively.

The velocity integrated intensities of CO and HI, W(CO) and W(HI), respectively, were converted into molecular column density $N(H_2)$ and atomic column density N_H(HI), and the total proton column density was obtained as $N_H(H_2+HI) = 2 \times N(H_2)$ + N_H(HI). A relationship $N(H_2)$ (cm^{-2}) = X_{CO} (cm^{-2} (K km $s^{-1})^{-1}$) × W(CO) (K km s^{-1}) was used, where $X_{CO} = 2.0 \times 10^{20}$ (cm^{-2} (K km $s^{-1})^{-1}$) (Bertsch et al. 1993). The HI line was generally assumed to be optically thin and a relationship N_H(HI) = 1.823×10^{18} × W(HI) was used (Dickey and Lockman 1990). For the regions where the HI is optically active, we had to apply a correction for self-absorption. Details of the method are given by Sect. 3.2.3.3.

4.2 Results

4.2.1 Typical X-Ray Spectra

Figure 4.2 shows *Suzaku* XIS 0+2+3 spectra in the three typical regions, the north (α_{J2000}, δ_{J2000}) = ($17^h14^m19.95^s$, $-39°28'31.11''$), the center (α_{J2000}, δ_{J2000}) = ($17^h13^m59.33^s$, $-39°45'31.49''$), and the south (α_{J2000}, δ_{J2000}) = ($17^h12^m56.75^s$, $-40°00'31.28''$), and the results of the model fitting. The lower parts show residuals in the fitting indicating that the fitting is reasonably good. We see no sign of thermal X-rays in Fig. 4.2. The absorbing column density N_H(X-ray) is $\sim 0.5 \times 10^{22}$ cm^{-2} both in the north and the center, but the photon indices differ, as $\Gamma = 2.1 \pm 0.1$ and $\Gamma = 2.7 \pm 0.1$ for the north and center, respectively. On the other hand, the south has large absorbing column density $N_H(\text{X-ray}) = 0.89^{+0.09}_{-0.08} \times 10^{22}$ cm^{-2} and photon index Γ is $\sim$2.7. These differences are seen as significantly different spectral shapes in Fig. 4.2. This confirms the fact that the X-ray spectrum changes significantly from place to place, as shown in the previous studies (e.g., Cassam-Chenaï et al. 2004; Tanaka et al. 2008)

4.2.2 Spatial and Spectral Characterization of the X-Rays

4.2.2.1 Absorbing Column Density

Figure 4.3a shows the absorbing column density N_H(X-ray) in the individual regions, where the *Suzaku* XIS 1–5 keV intensity is overlayed as contours. We aimed at achieving a relative error of 30% at maximum at the 90% confidence level by tuning the pixel size. Consequently, the average relative error and its maximum value are confined to 14 and 30 %, respectively, at the 90 % confidence level. This accuracy is high enough to assess the spatial variation of the absorbing column density and photon index.

We find that the global distribution of N_H(X-ray) shows a shell-like structure in Fig. 4.3a. On the east side of center ($\alpha_{J2000} \sim 17^h14.5^m$, $\delta_{J2000} \sim -39°40'$) and the west side of center ($\alpha_{J2000} \sim 17^h13^m$, $\delta_{J2000} \sim -39°49'$), N_H(X-ray) is as small as 0.4–0.5 $\times$ 10^{22} cm^{-2} (region in blue). On the other hand, two regions in the northeast ($\alpha_{J2000} \sim 17^h15^m$, $\delta_{J2000} \sim -39°25'$) and the northwest ($\alpha_{J2000} \sim 17^h12^m$, $\delta_{J2000} \sim -39°30'$) show medium values of N_H(X-ray) = 0.7–1.0 $\times$ 10^{22} cm^{-2} (region in green), and part of the southwest ($\alpha_{J2000} \sim 17^h12.5^m$, $\delta_{J2000} \sim -40°5'$) shows the largest N_H(X-ray) with 1.1–1.4 $\times$ 10^{22} cm^{-2} (region in red). Therefore, the absorbing column density varies from 0.4 $\times$ 10^{22} cm^{-2} to 1.4$\times 10^{22}$ cm^{-2} within the SNR. These values are mostly consistent with the previous studies with *XMM-Newton* (Cassam-Chenaï et al. 2004 typical angular resolution $\sim 8'$), whereas the angular resolution and the source coverage are better in the present study.

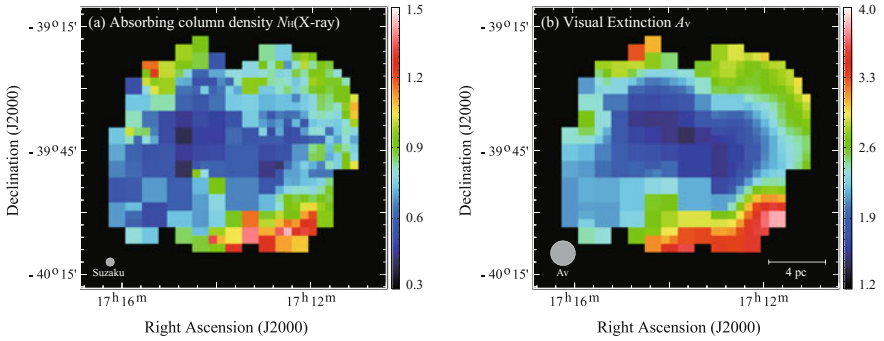

Fig. 4.4 **a** Distribution of the absorbing column density N_H(X-ray), same as that in Fig. 4.3 (b), but the color scale is changed. **b** Distribution of the visual extinction A_V (Dobashi et al. 2005). The grid separations are the same those as **(a)**

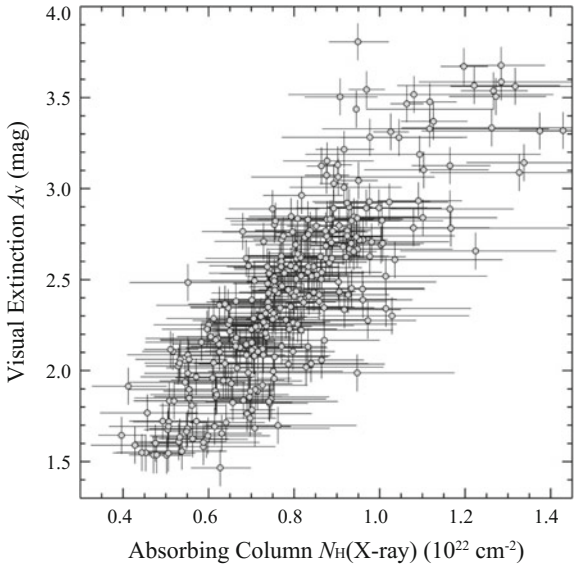

Fig. 4.5 Correlation plot between the absorbing column density N_H(X-ray) (in units of 10^{22} cm^{-2}) and the visual extinction A_V (in units of mag). The error bars are given at a 90% confidence level in N_H(X-ray)

Figure 4.4 shows absorbing column density N_H(X-ray) and visual extinction (A_V in units of mag) derived from the Digitized Sky Survey I (DSS; 2005). The visual extinction is smoothed to the same binning as with the X-rays. The values of A_V in Fig. 4.4b are roughly classified into the three levels: low values ($A_V < 2$ mag in blue) in the center of the SNR, medium values (2 mag $< A_V < 3$ mag in green) in the northeast and northwest regions, and high values ($A_V > 3$ mag in red) in the southwest. The general trend of A_V is similar to that of N_H(X-ray). Figure 4.5 shows a correlation plot between absorbing column density N_H(X-ray) and visual extinction, showing a good correlation with a correlation coefficient of ~0.83.

4.2.2.2 Photon Index and Flux

Figure 4.3b and c shows the distributions of photon index Γ and absorption-corrected flux $F_{3-10\mathrm{keV}}$, respectively. Their relative and maximum errors are ∼6% and 13% in Fig. 4.3b and ∼7% and 23% in Fig. 4.3c at the 90% confidence level, respectively. Like the absorbing column density, these quantities show significant spatial variation. In particular, the photon index is the largest with $\Gamma \sim 3$ (in orange color) toward the center ($\alpha_{\mathrm{J2000}} \sim 17^{\mathrm{h}}13.5^{\mathrm{m}}$, $\delta_{\mathrm{J2000}} \sim -39°48'$) and the central south ($\alpha_{\mathrm{J2000}} \sim 17^{\mathrm{h}}13.5^{\mathrm{m}}$, $\delta_{\mathrm{J2000}} \sim -40°3'$). On the other hand, six regions with small photon indices ($\Gamma < 2.4$) are distributed as islands inside the SNR: the northwest ($\alpha_{\mathrm{J2000}} \sim 17^{\mathrm{h}}11^{\mathrm{m}}50^{\mathrm{s}}$, $\delta_{\mathrm{J2000}} \sim -39°32'30''$), the southwest ($\alpha_{\mathrm{J2000}} \sim 17^{\mathrm{h}}12^{\mathrm{m}}30^{\mathrm{s}}$, $\delta_{\mathrm{J2000}} \sim -39°56'30''$), the north ($\alpha_{\mathrm{J2000}} \sim 17^{\mathrm{h}}14^{\mathrm{m}}$, $\delta_{\mathrm{J2000}} \sim -39°30'$), the east ($\alpha_{\mathrm{J2000}} \sim 17^{\mathrm{h}}15^{\mathrm{m}}$, $\delta_{\mathrm{J2000}} \sim -39°40'$), and two regions in the southeast ($\alpha_{\mathrm{J2000}} \sim 17^{\mathrm{h}}14^{\mathrm{m}}30^{\mathrm{s}}$, $\delta_{\mathrm{J2000}} \sim -39°55'$) and ($\alpha_{\mathrm{J2000}} \sim 17^{\mathrm{h}}15^{\mathrm{m}}$, $\delta_{\mathrm{J2000}} \sim -40°00'$). We do not discuss some regions with small photon index in the peripheral of the SNR where the statistics is worse than that inside. The absorption-corrected flux $F_{3-10\mathrm{keV}}$ is similar to the 1–5 keV X-rays contours, especially at the brightest peaks in the northwest, west, and southwest. We also find another strong peak in the north ($\alpha_{\mathrm{J2000}} \sim 17^{\mathrm{h}}13^{\mathrm{m}}36^{\mathrm{s}}$, $\delta_{\mathrm{J2000}} \sim -39°37'31.7''$). These flux excesses are not due to a systematic error and are possibly connected with the ISM distribution, as discussed in Sect. 4.3.

4.2.3 *Comparison with the ISM: The X-Ray Flux, Photon Index, and ISM*

Overlays of the interstellar gas at $V_{\mathrm{LSR}} = -20$ to 2 km s^{-1} with absorption-corrected flux $F_{3-10\mathrm{keV}}$ and photon index Γ are shown in Fig. 4.6a and b, respectively, where

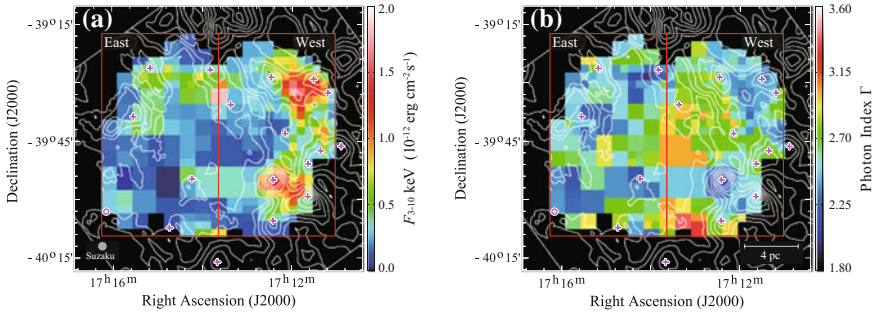

Fig. 4.6 Distribution of **a** the absorption-corrected flux $F_{3-10\mathrm{keV}}$ and **b** photon index Γ as Fig. 4.3. The *contours* indicate the proton column density $N_{\mathrm{H}}(\mathrm{H_2+HI})$ in a velocity range from −20 to 2 km s^{-1}. The contour levels are 0.6, 0.75, 0.90, 1.1, 1.3, 1.5, 1.7, 1.9, and 2.1×10^{22} cm^{-2}. The *magenta* crosses and *circle* correspond to the positions of CO and HI clumps (Sect. 2.2.1)

the ISM has a total proton column density of $N_{\rm H}(H_2{+}HI)$, including that derived from the CO and HI. The velocity range of the associated ISM is derived by Moriguchi et al. (2005) based on a good correlation between the ISM and X-rays enhanced by the interaction with the SNR. We have also annotated the positions (center of gravity) of the molecular clumps (crosses) and the HI clump (circle) defined by Sect. 2.2.1. We will hereafter refer to the regions between the clumps as "inter-clump." Fig. 4.6a shows a trend that the X-rays are enhanced toward the regions with enhanced ISM in a pc scale. This trend is most significant in the west of the SNR, where the ISM is rich. On the other hand, in a sub-pc scale, we find that each bright spot of X-rays is lying around the CO and HI clumps except for the molecular clump in the southwest ($\alpha_{\rm J2000} = 17^{\rm h}12^{\rm m}25.3^{\rm s}$, $\delta_{\rm J2000} = -39°55'7.4''$; named as, "clump C''). These results are consistent with those of Chap. 2, and the present work has made it possible to evaluate the trend more quantitatively. Figure 4.7 shows a correlation plot between $F_{3--10{\rm keV}}$ and the ISM density; the linear correlation coefficients (hereafter LCC) are ∼0.55 (for the whole), ∼0.19 (the east, on the left side of $\alpha_{\rm J2000}$ $\sim 17^{\rm h}13^{\rm m}38^{\rm s}$), and ∼0.54 (west, on the right side of $\alpha_{\rm J2000}$ $\sim 17^{\rm h}13^{\rm m}38^{\rm s}$). The LCC ∼0.55 does not show strong correlation, but the number of samples in the plot ∼300 indicates a positive correlation at a 5% confidence level according to a T-test (e.g., Taylor 1982).

In Fig. 4.6b, we note that the regions having a hard spectrum are seen toward the enhanced ISM in the west, whereas regions of hard spectrum are also found toward the diffuse ISM in the east. Most outstanding are the ISM peaks toward/around the two X-ray peaks in the northwest ($\alpha_{\rm J2000}$ $\sim 17^{\rm h}11^{\rm m}50^{\rm s}$, $\delta_{\rm J2000}$ $\sim -39°32'30''$) and in the southwest ($\alpha_{\rm J2000}$ $\sim 17^{\rm h}12^{\rm m}30^{\rm s}$, $\delta_{\rm J2000}$ $\sim -39°56'30''$. In addition, we find four regions of the hard spectrum in the east where the ISM is diffuse ($\alpha_{\rm J2000}$ $\sim 17^{\rm h}15^{\rm m}40^{\rm s}$, $\delta_{\rm J2000}$ $\sim -39°58'00''$). Figure 4.8 is a correlation plot showing that the relationships between the ISM and photon index in the west and east are different. In the west, the spectrum is hard when the ISM is dense and the spectrum is soft when the ISM is diffuse (LCC ~ -0.41). In the east, the ISM is diffuse and the photon

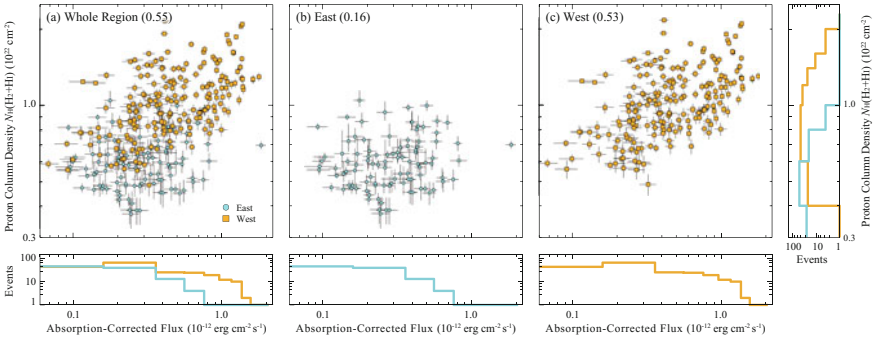

Fig. 4.7 Correlation plot between the absorption-corrected flux $F_{3-10{\rm keV}}$ and the proton column density $N_{\rm H}(H_2{+}HI)$ in the **a** whole region, **b** East, and **c** West. The regions are defined as follows Fig. 4.6:*circle* for East, *square* for West. The histograms are also shown at lower or right side of each plot. For all plots, the scale is square-root

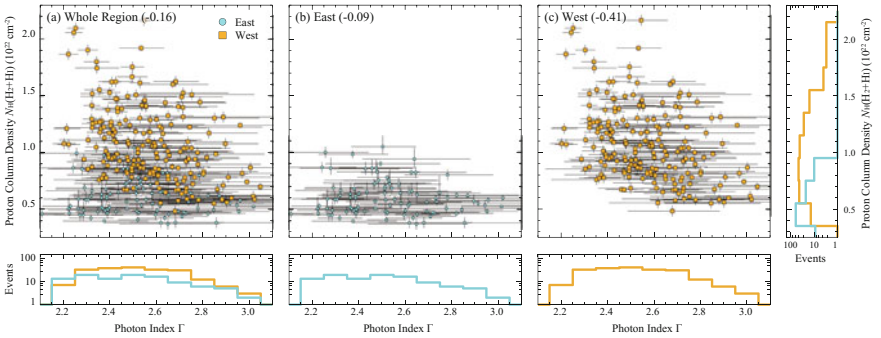

Fig. 4.8 Correlation plot between the photon index Γ and the proton column density $N_{\rm H}$(H$_2$+HI) in the **a** whole region, **b** East, and **c** West. For all plots, the scale is linear

index shows variation (LCC ~ -0.08) and the ISM density is not apparently related to the variation of the photon index for the entire region. LCC is estimated to be ~ -0.16. Additionally, we show correlation plots between the photon index Γ and the absorption-corrected flux $F_{3-10{\rm keV}}$ in Fig. 4.9. LCCs are ~ -0.62 (the whole), ~ -0.53 (the east), and ~ -0.81 (the west). The histograms toward the western and eastern regions show a similar trend to the photon index distribution with respect to the ISM density, whereas the western region has much higher X-ray fluxes than the eastern region. We shall discuss these results later in Sect. 4.3.2.2.

We summarize the main aspects of the present analysis as follows (Figs. 4.6, 4.7, 4.8, and 4.9):

1. It is notable that the most intense X-rays are seen in the two regions toward or around the CO peaks (Fig. 4.6a). In the western half of the SNR, the ISM density is high with significant H$_2$ and the X-rays are enhanced. In the eastern half of the

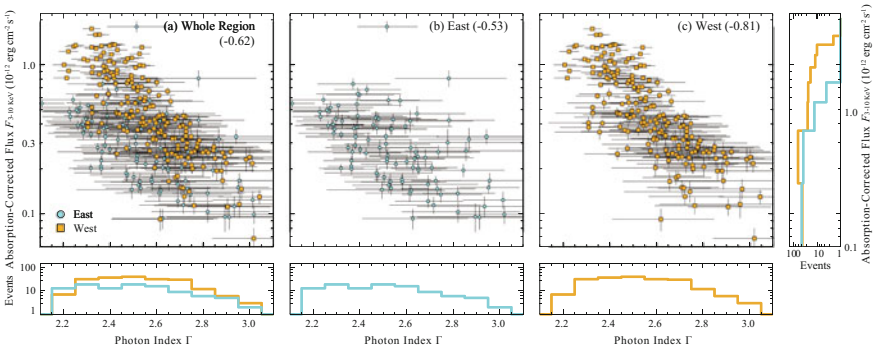

Fig. 4.9 Correlation plot between the photon index Γ and the absorption-corrected flux $F_{3-10{\rm keV}}$ in the **a** whole region, **b** East, and **c** West. The scale is linear in the photon index Γ and is square-root in the absorption-corrected flux $F_{3-10{\rm keV}}$

SNR, the ISM density is low, being dominated by HI, and the X-rays are weak. The overall correlation between the ISM density and the X-rays is however not significantly high with a correlation coefficient of ∼0.55 (Fig. 4.7).
2. The smallest X-ray photon index (around 2.3) is seen toward the following six regions: around/toward the two CO peaks in the west and toward the four regions of low ISM density in the east (Fig. 4.6b). The largest X-ray photon index (around 3) is found toward the central region of the SNR as well as in the southern edge (Fig. 4.6b).
3. The photon index shows a good correlation with the X-rays, and a low photon index is seen toward regions of intense X-rays and vice versa (Fig. 4.9). There is an offset of 0.3 in this correlation between the eastern and western halves of the SNR, i.e., the X-rays are more intense in the west, where the ISM is denser, than in the east. The overall correlation between the photon index and the ISM density is not high (Fig. 4.8).

4.3 Discussion

4.3.1 Spatial Variation of the Absorbing Column Density

The observations with *Suzaku* XIS have enabled us to estimate detailed distributions of the absorbing column density $N_{\rm H}$(X-ray) and photon index Γ in RX J1713.7−3946 at a low background level and high photon statistics. Here, we first discuss the absorbing column density $N_{\rm H}$(X-ray).

The spatial distribution of $N_{\rm H}$(X-ray) delineates the SNR shell, as shown in Fig. 4.4. This distribution shows a good correspondence with visual extinction. The regression in a straight line calculated from a least-squares fitting affords $N_{\rm H}$(X-ray) $({\rm cm}^{-2}) = (3 \pm 1) \times 10^{21} \cdot A_{\rm V}$ (magnitude) for the scatter plot in Fig. 4.5. The numerical factor is slightly larger than that of the conventional relation $N_{\rm H}$ $({\rm cm}^{-2}) = 2.5 \times 10^{21} \cdot A_{\rm V}$ (magnitude) (Jenkins and Savage 1974). This is understandable if we consider that the distance of RX J1713.7−3946 is 1 kpc, since visual extinction tends to be under-estimated at distances larger than a few 100 pc owing to the presence of foreground stars. It is not necessarily true that all $N_{\rm H}$(X-ray) are physically associated with the SNR. Here, we need to consider the contribution of the local gas between the SNR and the sun (Fig. 4.10a). Moriguchi et al. (2005) already estimated the foreground component $N_{\rm H,local}$(H_2+HI) (Fig. 4.10b). Figure 4.10c shows the distribution of absorbing column density [$N_{\rm H}$(X-ray)−$N_{\rm H,local}$(H_2+HI in the SNR, which gives a shell-like distribution of $N_{\rm H}$(X-ray) more clearly than Fig. 4.3a. The absorption toward the center of the SNR is $\sim 0.2 \times 10^{22}$ ${\rm cm}^{-2}$, whereas that toward the outer boundary is shell-like with absorbing column density of ~ 0.5–0.8×10^{22} ${\rm cm}^{-2}$. This shell represents a cavity wall of the ISM created by the stellar wind of the SNR progenitor. The inside of the cavity is highly evacuated, with a density lower than

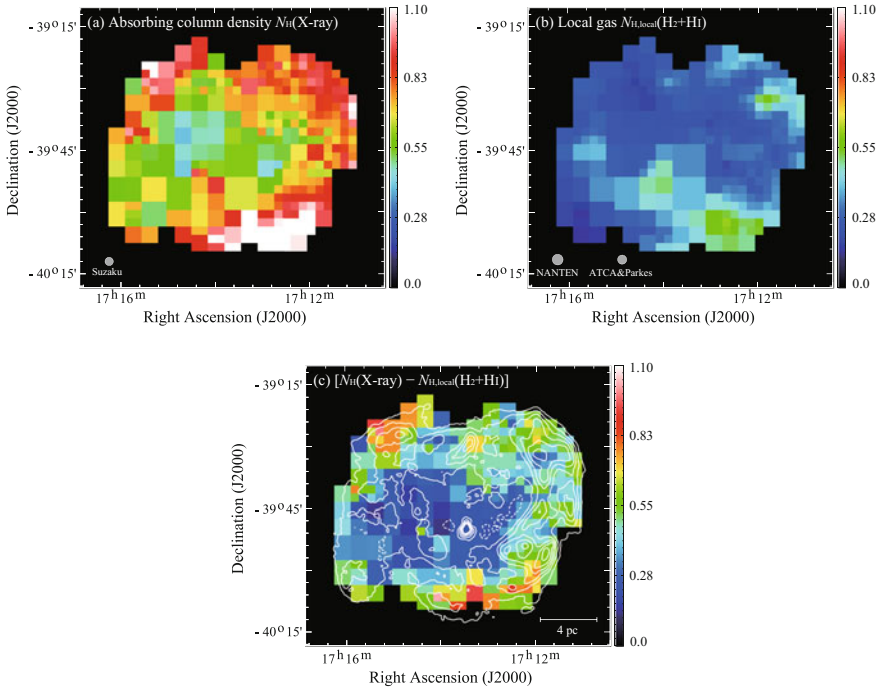

Fig. 4.10 **a** Distribution of the absorbing column density N_H(X-ray), same as that in Fig. 4.3a, but the color scale is changed to stress the region of the low absorbing column density. **b** Distribution of the proton column density in local gas $N_{H,local}$(H_2+HI) estimated using the CO and HI datasets. **c** Distribution of the absorbing column density [N_H(X-ray)−$N_{H,local}$(H_2+HI)] overlaid with smoothed contours of the *Suzaku* XIS mosaic images, as shown in Fig. 4.3. All images have the same color scale

$\sim$ 1 cm^{-3}, and the dense clumps in the cavity wall have higher densities of the order of $\sim 10^2$–10^4 cm^{-3} (e.g., Inoue et al. 2012).

We next discuss the absorption toward the southeastern rim. In this region, we identified cold HI gas that corresponds to the VHE γ-ray shell (see Fig. 3.4). The cold HI with low spin temperature of $\sim$40 K has a density of around 100 cm^{-3}, less than the $\sim$1000 cm^{-3} threshold density for the collisional excitation of CO emission. The proton column density of the cold HI without CO emission is estimated to be $\sim 0.5 \times 10^{22}$ cm^{-2} from the HI self-absorption in the southeastern rim of RX J1713.7−3946. The present absorption in the SNR calculated from X-rays also has a column density of 0.4–0.5 $\times$ 10^{22} cm^{-2} (Fig. 4.10c), which is consistent with the cold HI.

We compare the absorbing column density [N_H(X-ray) − N_{H_local}(H_2+HI)] (Fig. 4.10c) with N_H(H_2+HI), the proton column density physically associated with the X-ray emitting shell, in two velocity ranges of the interacting gas in Figs. 4.11 and 4.12. Figure 4.11a and b show [N_H(X-ray) − N_{H_local}(H_2+HI)] overlayed on the

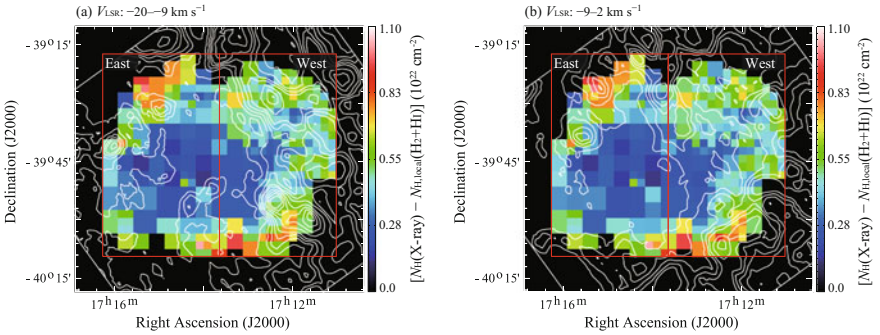

Fig. 4.11 Distribution of the absorbing column density [N_H(X-ray)−$N_{H,local}$(H$_2$+HI)], same as that of Fig. 4.6 (c), superposed on the proton column density N_H(H$_2$+HI) in the velocity range from **a** −20 to −9 km s^{-1} and from **b** −9 to 2 km s^{-1}, respectively. The contour levels are 0.4, 0.5, 0.6, 0.7, 0.9, 1.1, 1.3, and 1.5 × 10^{22} cm^{-2}. The whole regions, East, and West were used for the correlation plots (see Fig. 4.12)

ISM proton column density N_H(H$_2$+HI) at $V_{LSR} \sim -20$ to −9 km s^{-1} and ~ -9 to 2 Km s^{-1}. This comparison shows that the ISM distribution has a generally good correspondence with the X-ray absorbing column density. However, note that the blue-shifted ISM shows a poorer correlation than the red-shifted ISM with the X-ray absorbing column density, as shown in Fig. 4.12 in the scatter plots between the ISM and the X-ray absorption column density. In Fig. 4.12, we divide the plots into the red- and blue-shifted ISM. The blue-shifted ISM in the west shows a poor correlation with the X-ray absorbing column density of LCC∼0.25, while the red-shifted ISM in the west has a higher correlation of LCC∼0.39 than the blue-shifted ISM. This indicates that the red-shifted ISM is located on the far side of the SNR, which represents behavior opposite to what would be expected in the expanding motion of the shell-like ISM. The relative position of the ISM is explicable if the pre-existent cloud motion is dominant for the dense CO gas instead of expansion, as has already been suggested to explain the velocity distribution of the HI self-absorption.

4.3.2 Relationship Among the X-Ray Flux, Photon Index, and X-Ray Absorption/ ISM

4.3.2.1 Shock–Cloud Interaction

Inoue et al. (2012) showed using magnetohydrodynamics numerical simulations that the X-ray intensity is closely correlated with the ISM via the enhanced magnetic field around dense clumps caused by turbulence in the shock–cloud interaction. This interaction creates a correlation between the ISM and X-rays at a pc scale via the magnetic field. Chapter 2 showed that pc scale correlation is seen between the X-ray

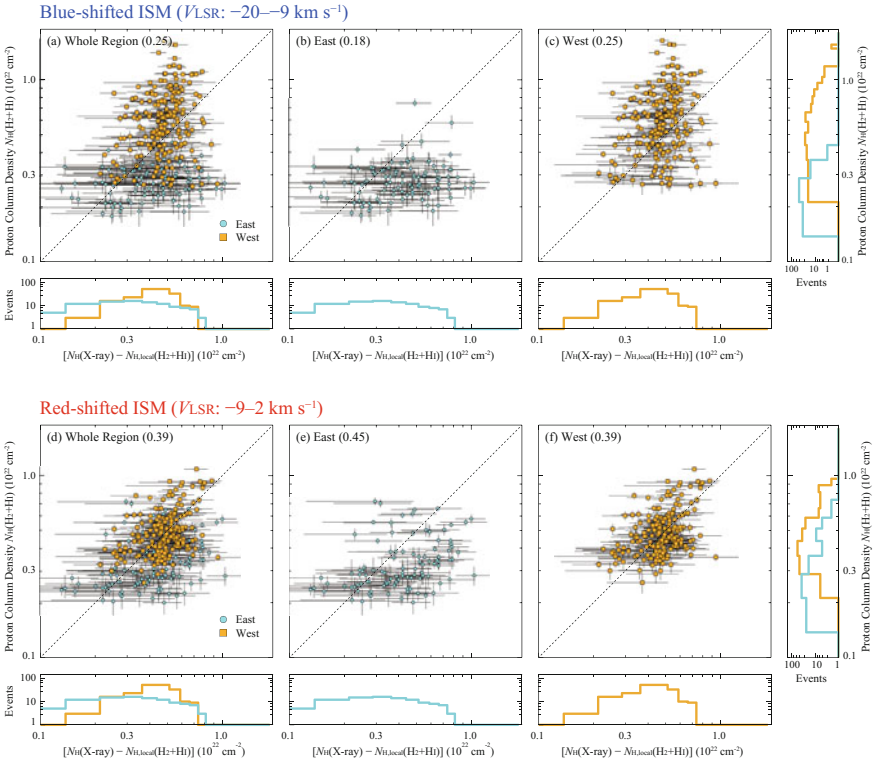

Fig. 4.12 Correlation plot between the absorbing column density [N_H(X-ray)−$N_{H,local}$(H$_2$+HI)] and the proton column density N_H(H$_2$+HI) in the velocity range from **a–c** −20 to −9 km s^{-1} and from **d–f** −9 to 2 Km s^{-1}, respectively. The regions indicate **a**, **d** whole region, **b**, **e** East, and **c**, **f** West. The *dashed lines* are the bisector for each panel. The histograms are also shown at lower or right side of each plot. For all plots, the scale is square-root

intensity and the clump mass interacting with the SNR blast waves as well as anti-correlation between them in a sub-pc scale due to exclusion of the CR electrons in the dense clumps. The distributions of the X-ray intensity in Fig. 4.6a at grid sizes of 2–8′ (0.6–2.4 pc) show their interrelation at a pc scale; we see a trend that the X-rays are enhanced in the west where the ISM is rich and that the X-rays are depressed in the east where the ISM is poor. This is consistent with what is expected in the shock–cloud interaction scheme. The higher dispersion in Fig. 4.7 may be partly ascribed to anti-correlation at a sub-pc scale, which is consistent with the suggestion in Chap. 2.

4.3.2.2 Efficient Cosmic Ray Acceleration

Based on the present results for photon index (Fig. 4.3b), we discuss the efficient cosmic ray acceleration in RX J1713.7−3946. As shown in a previous study, (Takahashi

et al. 2008; Tanaka et al. 2008), the photon index in the 1–10 keV range reflects the rolloff energy ε_0 of the synchrotron X-rays: a small (large) photon index corresponds to large (small) rolloff energy. According to the standard DSA scheme, the rolloff energy of synchrotron photons ε_0 is given as follows when the synchrotron cooling is effective (Zirakashvili and Aharonian 2007),

$$\varepsilon_0 = 0.55 \times (v_{\rm sh} \,/\, 3000 \text{ km s}^{-1})^2 \, \eta^{-1} \text{ (keV)}, \tag{4.1}$$

where $v_{\rm sh}$ is the shock speed and $\eta = B^2/\delta B^2$ (>1) a gyro-factor, the degree of magnetic field fluctuation. In particular, the limit of $\eta = 1$ is called the Bohm limit corresponding to highly turbulent conditions, and accordingly, the rolloff energy is likely determined by the shock speed and turbulence.

The present results suggest that in the west of the SNR, where the ISM is rich, the shock–cloud interaction is effective and turbulence is enhanced around dense ISM clumps. On the other hand, in the east of the SNR where the ISM is poor, the DSA alone is mainly working without shock–cloud interaction. We show a schematic summarizing the relevant features in Fig. 4.13. The shaded regions in blue, white, and orange correspond to the photon index $\Gamma < 2.4$ (small), $2.4 < \Gamma < 2.8$ (medium),

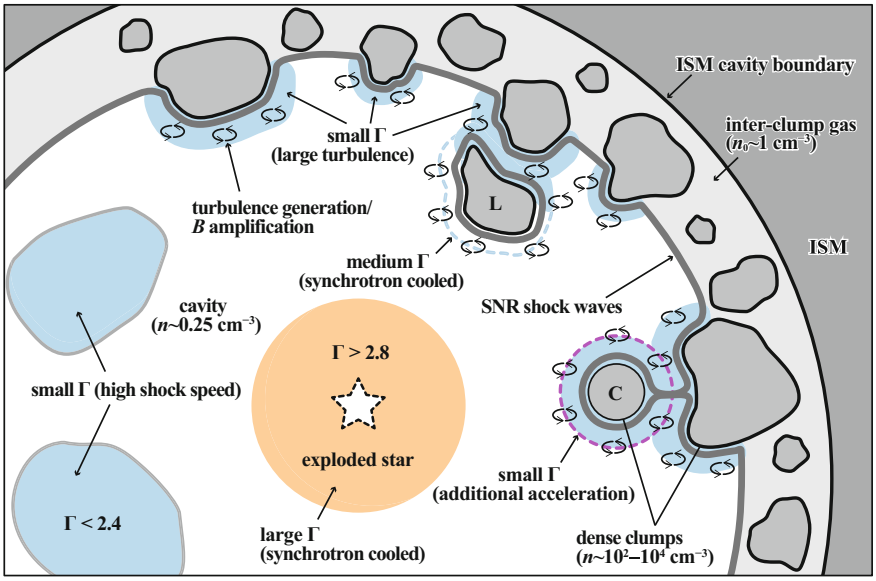

Fig. 4.13 Schematic of the efficient cosmic ray acceleration toward RX J1713.7−3946. The SNR shock waves travel through the cavity (gas density $n \sim 0.25$ cm^{-3}), where cosmic ray acceleration is at work through the DSA scheme and the shock speed is not much decelerated in lower density. Propagated shock waves are stalled toward the dense clumps and are traveling in the inter-clump space. Shock–cloud interaction generates turbulence ($\eta \sim 1$) and enhances the magnetic field around the dense clumps. The accelerated particles in the innermost cavity and some of clumps are already cooled down due to synchrotron cooling. The additional acceleration is induced by high turbulence and strong magnetic fields around some of the dense clumps (see the text for more details)

and $\Gamma > 2.8$ (large), respectively. In Chap. 2, we noted that the innermost cavity of 3–4 pc radius is surrounded by the ISM shell comprising the dense clumps and the inter-clump gas. The inter-clump gas is shown by the shaded gray region around the clumps in Fig. 4.13. The dense clumps have a density of 10^2 to 10^4 cm^{-3} (see also Sect. 2.2.1) and are mainly distributed in the west toward the Galactic plane. The inter-clump gas has a density of $<2\,\mathrm{cm}^{-3}$, as given by the upper limit from thermal X-rays (Takahashi et al. 2008), and we shall adopt a density of inter-clump gas of $1\,\mathrm{cm}^{-3}$ for discussion. We assume that the density in the cavity is $\sim 0.25\,\mathrm{cm}^{-3}$, the same as that estimated toward the Gum nebula, where the gas is swept up by the strong stellar winds from ζ Pup (Wallerstein and Silk 1971; Gorenstein et al. 1974). In this scheme, DSA is efficiently taking place in the cavity and the accelerated CRs are injected into the ISM shell. Figure 4.13 show that the shock waves are now interacting with the five dense clumps and has passed through two clumps denoted as "C'' and "L''.

Table 4.1 gives two sets of possible parameters for discussion in the two cases with different ISM density, although they are crude at best (c.f., Tanaka et al. 2008). In the west, where the shock–cloud interaction is in effect, the magnetic field may be amplified up to $\sim$1 mG, as indicated by the short time variation of $\sim$1 year in the synchrotron X-rays by *Chandra*, where the Bohm limit ($\eta = 1$) is a good approximation (Uchiyama et al. 2007). On the other hand, the shock speed $v_{\rm sh}$ is proportional to $1/\sqrt{n}$ and is decreased in the dense ISM, where n is the average number density of the ISM. The observational result shows that vsh is decreased to 4,500 km s^{-1} or less, and we shall assume $\sim$3000 km s^{-1} (Uchiyama et al. 2007; Zirakashvili and Aharonian 2007). It is probable that in the west of the SNR, it is primarily shock–cloud interaction causing large rolloff energy and a small photon index. On the other hand, in the east, the shock speed is not much decelerated in lower density regions. A possible scenario is as follows: the average ISM density in the east is about 1/4 of that in the west, causing the shock speed $v_{\rm sh}$ to be larger by a factor of 2. In this case, η becomes larger than 1, but the term (the shock speed $v_{\rm sh})^2$ is more effective. If we assume the shock speed is $\sim$6000 km s^{-1} and $\eta \sim 4$, the rolloff energy becomes larger as $\sim$ 0.6 keV (Tanaka et al. 2008) and the photon index becomes smaller. The trend in the photon index, therefore, is largely explicable by the DSA scheme with modification due to the ISM gas.

The regions where the photon index is small in the east seem to be located toward the edge of medium density clumps along the outer part of the shell (Fig. 4.6b). It is

Table 4.1 An example of the physical parameters for the rolloff energy

Region	Gas density n (cm^{-3})	Gyro-factor η	Shock speed $v_{\rm sh}$ (km s^{-1})	Rolloff energy ε_0 (keV)
Inter-clump	1†	1‡	3000‡	0.6§
Inside of the cavity	0.25*	4	6000	0.6

Notes. †Inoue et al. (2012), *Wallerstein and Silk (1971); Gorenstein et al. (1974), ‡Uchiyama et al. (2007); Zirakashvili and Aharonian (2007), §Takahashi et al. (2008); Tanaka et al. (2008)

however not likely that this small photon index is caused by shock–cloud interaction because the spatial extent with $\Gamma < 2.4$ is four times larger than that in the west. It is predicted that the area where the rolloff energy (photon index) is above (below) a certain value becomes small with the increase of the magnetic field if the Sedov–Taylor evolution is assumed (Eq. (9) in Kishishita et al. 2013). This implies that the field is stronger in the east than in the west but is inconsistent with the shock–cloud interaction. It is therefore reasonable that the acceleration in the east is mainly caused by DSA and not by the shock–cloud interaction.

In Fig. 4.13, the innermost part of the SNR having a large photon index $\Gamma > 2.8$ is shown by orange color. We suggest that the electrons there have lower rolloff energy due to synchrotron cooling over the last 1,000 year; for magnetic fields of 10 μG, the CR electron cooling time at 10 keV is as small as $\sim$500 year, whereas that at 1 keV is as large as $\sim$1,500 year, leading to low rolloff energy in the central 3–4 pc. We also note that such spectral softening can be described as energy loss due to adiabatic expansion (e.g., Kishishita et al. 2013).

One would expect that the photon index would become even larger toward the denser regions if only $v_{\rm sh}$ determines the photon index. Interestingly, the photon index becomes small toward clump C and the region between the two dense clumps, D and L in Fig. 4.6b. It is also notable that X-rays are enhanced toward these regions, which have small photon indices. In the shock–cloud interaction scheme, the magnetic field is amplified in the interacting region, leading to higher synchrotron loss and smaller rolloff energy. This can lead to lower X-ray intensity and lower rolloff energy toward the dense clumps, although obviously we will need a more elaborate analysis to quantitatively affirm this. It is thus possible that the observed trend is not explained by only a DSA scheme. We suggest that some additional acceleration mechanism is working to accelerate CR particles in the west, where the ISM is rich. Such mechanisms might include the second-order Fermi acceleration (Fermi 1949) and/or magnetic reconnection in the turbulent medium (Hoshino 2012). In the latter case, compression in the shocked region creates multiple magnetic islands and causes magnetic reconnection that leads to outflow and acceleration of high-energy particles emitting enhanced synchrotron radiation. This scenario is consistent with the shock–cloud interaction picture presented for RX J1713.7−3946 (Inoue et al. 2012), and multiple magnetic islands may be formed around the dense ISM clumps.

To summarize, we suggest that the ISM and its distribution have a significant impact on the mechanics of particle acceleration via the shock–cloud interaction. This suggests a tight relationship between the SNR and ISM. The present work explored the CR electron behavior in significant detail, which was not achieved in previous studies, and demonstrated that the ISM density significantly affects the CR electron rolloff energy. In particular, dense molecular clumps excite turbulence in the shock waves, amplifying the magnetic field. The CR electron rolloff energy increases

despite the presence of such amplified fields, and we suggest that additional electron acceleration is observed in such turbulent regions around the dense clumps.

In the near future, the Cherenkov Telescope Array will provide information on the spectral distribution of γ-rays over the SNR at $1'$ resolution and will allow us to investigate the spectra and acceleration of both CR protons and electrons. In addition, the soft X-ray spectrometer of ASTRO-H will probe yet undetected thermal X-rays using sensitive high-energy resolution spectroscopy in RX J1713.7−3946. We can then determine what fraction of the energy of the SNR blast waves is used for cosmic ray acceleration. Furthermore, the hard X-ray imager (HXI) of ASTRO-H will resolve photon index distribution at 10 keV or higher, possibly allowing us to constrain electron energy spectrum models by comparing those below 10 keV (e.g., Yamazaki et al. 2014). These future instruments will enable more accurate measurements of efficient cosmic ray acceleration.

4.4 Conclusions

We summarize the present work as follows:

1. We have estimated the spatial distribution of absorbing column density, photon index, and absorption-corrected flux (3–10 keV) comparable to the scale of the ISM distribution (a few arcmin) using *Suzaku* archival data with low background.
2. The X-ray flux shows enhancement toward the dense ISM, which is consistent with the shock–cloud interaction model by Inoue et al. (2012) wherein X-rays become bright around the dense cloud cores due to turbulent amplification of the magnetic field.
3. The photon index shows a high degree of variation within the SNR from $\Gamma = 2.1$–2.9. The photon index shows smallest values around the dense regions of cloud cores as well as toward diffuse regions with no molecular gas. This trend can be described as a rolloff energy variation of CR electrons (Zirakashvili and Aharonian 2007). We present possible parameters to explain the variation of the rolloff energy under the DSA scheme. The enhanced intensity and harder spectra of the X-rays toward the dense clumps may require additional electron acceleration toward the dense clumps, possibly via magnetic reconnection or other mechanism incorporating magnetic turbulence.
4. The absorbing column density shows a good correlation with visual extinction. We found that the southeastern rim identified by HI self-absorption, which shows enhanced VHE γ-rays, has a clear counterpart in X-ray absorption, lending new support to the HI self-absorption interpretation.

References

F. Acero, J. Ballet, A. Decourchelle, M. Lemoine-Goumard, M. Ortega, E. Giacani et al., Astrophys. J. **505**, 157 (2009)
D.L. Bertsch, T.M. Dame, C.E. Fichtel, S.D. Hunter, P. Sreekumar, J.G. Stacy et al., Astrophys. J. **416**, 587 (1993)
G. Cassam-Chenaï, A. Decourchelle, J. Ballet, J.-L. Sauvageot, G. Dubner, E. Giacani et al., Astron. Astrophys. **427**, 199 (2004)
K.M. Desai, Y.-H. Chu, R.A. Gruendl, W. Dluger, M. Katz, T. Wong et al., Astron. J. **140**, 584 (2010)
J.M. Dickey, F.J. Lockman, Annu. Rev. Astron. Astrophys. **28**, 215 (1990)
K. Dobashi, H. Uehara, R. Kandori, T. Sakurai, M. Kaiden, T. Umemoto et al., Publicat. Astronom. Soc. Jpn. **57**, 1 (2005)
E. Fermi, Physica. Rev. **75**, 1169 (1949)
P. Gorenstein, F.R. Harnden Jr., W.H. Tucker, Astrophys. J. **192**, 661 (1974)
M. Hoshino, Phys. Rev. Lett. **108**, 135003 (2012)
T. Inoue, R. Yamazaki, S.-I. Inutsuka, Y. Fukui, Astrophys. J. **744**, 71 (2012)
Y. Ishisaki, Y. Maeda, R. Fujimoto, M. Ozaki, K. Ebisawa, T. Takahashi et al., Publ. Astron. Soc. Jpn. **59**, 113 (2007)
E.B. Jenkins, B.D. Savage, Astrophys. J. **187**, 243 (1974)
T. Kishishita, J. Hiraga, Y. Uchiyama, Astron. Astrophys. **551**, A132 (2013)
K. Koyama, K. Kinugasa, K. Matsuzaki, M. Nishiuchi, M. Sugizaki, K. Torii et al., Publ. Astron. Soc. Jpn. **49**, L7 (1997)
K. Koyama, H. Tsunemi, T. Dotani, M.W. Bautz, K. Hayashida, T.G. Tsuru et al., Publ. Astron. Soc. Jpn. **59**, 23 (2007)
N.M. McClure-Griffiths, J.M. Dickey, B.M. Gaensler, A.J. Green, M. Haverkorn, S. Strasser, Astrophys. J. **158**, 178 (2005)
Y. Moriguchi, K. Tamura, Y. Tawara, H. Sasago, K. Yamaoka, T. Onishi et al., Astrophys. J. **631**, 947 (2005)
H. Nakajima, H. Yamaguchi, H. Matsumoto, T.G. Tsuru, K. Koyama, H. Tsunemi et al., Publ. Astron. Soc. Jpn. **60**, 1 (2008)
P.J. Serlemitsos, Y. Soong, K.-W. Chan, T. Okajima, J.P. Lehan, Y. Maeda et al., Publ. Astron. Soc. Jpn **59**, 9 (2007)
T. Takahashi, K. Abe, M. Endo, Y. Endo, Y. Ezoe, Y. Fukazawa et al., Publ. Astron. Soc. Jpn. **59**, 35 (2007)
T. Takahashi, T. Tanaka, Y. Uchiyama, J.S. Hiraga, K. Nakazawa, S. Watanabe et al., Publ. Astron. Soc. Jpn **60**, 131 (2008)
T. Tanaka, Y. Uchiyama, F.A. Aharonian, T. Takahashi, A. Bamba, J.S. Hiraga et al., Astrophys. J. **685**, 988 (2008)
J.R. Taylor, *An introduction to error analysis*, 2nd edn. (California, USB, 1982)
Y. Uchiyama, F.A. Aharonian, T. Tanaka, T. Takahashi, Y. Maeda, Nat. **449**, 576 (2007)
H. Uchiyama, M. Ozawa, H. Matsumoto, T.G. Tsuru, K. Koyama, M. Kimura et al., Publ. Astron. Soc. Jpn. **61**, 9 (2009)
G. Wallerstein, J. Silk, Astrophys. J. **170**, 289 (1971)
R. Yamazaki, Y. Ohira, M. Sawada, A. Bamba, Res. Astron. Astrophys. **14**, 165 (2014)
V.N. Zirakashvili, F. Aharonian, Astron. Astrophys. **465**, 695 (2007)

Chapter 5
Summary and Future Prospects

5.1 Summary of the Thesis

In this work, I summarize my Ph.D. study on shock–cloud interaction in the neighborhood of the young γ-ray supernova remnant (SNR) RX J1713.7−3946 on the basis of a multi-wavelength study. The datasets of NANTEN/NANTEN2 CO and ATCA & Parkes HI reveal the distribution and physical condition of the overall interstellar gas, which comprises both molecular and atomic components. I succeeded in obtaining the first evidence that efficient cosmic ray acceleration is strongly connected to the interaction between shock waves and interstellar gas and that cosmic ray protons are accelerated to close to the *knee* energy in the SNR. This investigation was conducted by comparing interstellar gas, H.E.S.S. very high energy (VHE) γ-ray, and *Suzaku* synchrotron X-ray data, as summarized below.

In Chap. 2, I presented a detailed study of SNR RX J1713.7−3946 based on NANTEN/NANTEN2 ^{12}CO(J = 1–0, 2–1, 4–3), ^{13}CO(J = 2–1), ASTE ^{12}CO(J = 3–2), ATCA & Parkes HI, and *Suzaku* X-ray data. RX J1713.7−3946 is located at (l, b) = (347.°3, −0.°5) and has a large apparent diameter of $\sim$ 1° ($\sim$20 pc at 1 kpc), lies at a short distance from Earth ($\sim$1 kpc), and is quite young ($\sim$1,600 yr). The SNR emits strong VHE γ-rays and synchrotron X-rays, making it a primary candidate for cosmic ray acceleration up to the *knee* energy. I determined the spatial distribution of the CO by primarily using the ^{12}CO(J = 2–1) and HI lines as well as synchrotron X-rays in the 1–5 and 5–10 keV energy bands toward the SNR. I newly identified nine CO clumps and a HI clump, all associated with the SNR, and derived their physical parameters (peak position, intensity, velocity, mass, etc.). I also estimated the details of some physical parameters in the prominent CO peaks of clumps A and C using ^{12}CO(J = 2–1, 3–2, 4–3) and ^{13}CO(J = 2–1) and revealed that clumps A and C have densities of 0.5–0.8 $\times$ 10^4 cm^{-3} and 0.8–1.7 $\times$ 10^4 cm^{-3} and temperatures of 9–11 and 11–16 K, respectively. Surprisingly, clump C shows a strong density gradient, consistent with an average density distribution of $r^{-2.2\pm0.4}$ (where r is the radius of clump C), and a clear bipolar outflow structure. Based on

H. Sano, *Shock-Cloud Interaction in RX J1713.7–3946*,
Springer Theses, DOI 10.1007/978-4-431-55636-7_5

this, I have concluded that clump C contains protostellar core(s) and has survived SNR shock erosion, since shock propagation has stalled in the dense clump.

In a morphological study between the CO/HI clumps and X-ray distribution, I found that X-rays are enhanced within ∼1 pc of the CO and HI peaks, whereas at smaller scales down to 0.1 pc, the CO peaks tend to be anti-correlated with the X-ray intensity, which decreases toward the CO and HI clumps. More detailed analysis showed that all clumps have a radius of $0°.04 \pm 0°.01$ and that the X-rays are distributed with a separation of $0°.07 \pm 0°.03$ from the center of each clump, indicating that the X-rays are rim-brightened on the CO/HI clumps. I also investigated the azimuthal distribution of X-rays around each CO clump and revealed that all the X-ray emissions surrounded by CO are enhanced toward the center of the SNR. Some of the clumps also emit X-rays at all azimuth angles, indicating that these clumps survived the SNR blast waves and are now embedded within the SNR. I also found a strong correlation (with a correlation coefficient of ~ 0.85) between the X-ray intensity and the clump mass interacting with the SNR shock waves.

I concluded that the interstellar gas clumps (including interstellar core clump C) were formed by a strong stellar wind from the progenitor of the SNR some Myr ago and are now interacting with the SNR shock waves. Although these CO/HI clumps are not destroyed by the SNR blast waves, the resulting X-ray intensities are greatly influenced by shock–cloud interaction with magnetic field amplification. The above findings were compared with the numerical simulations of magnetohydrodynamics interactions assuming a realistic highly inhomogeneous density distribution by Inoue et al. (2009, 2012), with the results indicating that the magnetic field is amplified around dense CO/HI clumps as a result of enhanced turbulence induced by the shock–cloud interaction. I interpret this as an enhancement of X-ray intensity caused by amplified magnetic fields that is proportional to the 1.5-th power of the magnetic field strength. Such enhanced magnetic fields may also lead to efficient acceleration in addition to the diffusive shock acceleration.

In Chap. 3, I conducted a detailed comparison between the overall interstellar gas and VHE γ-rays. I first attempted to reveal the distribution of interstellar protons using the NANTEN ^{12}CO(J = 1–0) and ATCA & Parkes HI datasets. To our surprise, I found an atomic gas (HI) component corresponding to the VHE γ-ray distribution toward the southeastern rim of the SNR, where previous studies had revealed no CO counterpart (e.g., Aharonian et al. 2006). Even more interestingly, the HI component was discovered as cold HI in a self-absorption dip and not as a line emission. This self-absorbed structure is considered to represent the high density region of HI, but it is not dense enough to allow significant detection (from either creation or excitation) of CO molecules (Goldsmith et al. 2007). Therefore, I assumed the background level of HI and estimated the total interstellar proton column density $N_{\rm p}$(H_2+HI) contained using absorption-corrected HI. As a result, I revealed that the total mass of the interstellar protons is $2.0 \times 10^4\ M_\odot$; this breaks down to a molecular component mass of $0.9 \times 10^4\ M_\odot$ and an atomic component mass of $1.1 \times 10^4\ M_\odot$. Most of the neutral gas was likely swept up by the stellar wind of an OB star prior to the supernova explosion to form a low-density cavity and a dense wall. Thus, the distribution of the interstellar gas was highly inhomogeneous; the inner region of

the SNR had very low density ($N_{\rm H} \sim 0.01$ cm^{-3}), and the outer region formed with the molecular wall ($N_{\rm H} \sim 100$–10000 cm^{-3}). Finally, I obtained an extremely high spatial correspondence between the total interstellar proton column density $N_{\rm p}$(H$_2$+HI) and VHE γ-ray emission by comparing in both azimuthal and radial plots and concluded that the VHE γ-rays are of hadronic origin. I also estimated the total energy of cosmic ray protons, $W_{\rm tot} = (0.8$–$2.3) \times 10^{48}$ erg, which is 0.1% of the total energy of a typical supernova explosion, using an averaged interstellar gas density of $\sim$130 cm^{-3}.

In addition, I investigated the penetration depth, $l_{\rm pd}$, of cosmic ray protons into the dense interstellar clumps. According to numerical simulation, $l_{\rm pd}$ is proportional to the square root of the cosmic ray proton energy and SNR age but is inversely proportional to the square root of magnetic field strength (Inoue et al. 2012). Therefore, high-energy cosmic ray protons such as VHE γ-ray emitters penetrate into the dense clumps but lower-energy cosmic ray protons such as GeV γ-ray emitters do not. Correspondingly, the γ-ray spectrum is (a) highly energy dependent when (b) the magnetic field is strong enough ($\sim 100\mu$ G). Condition (a) is consistent with the *Fermi* Large Area Telescope (LAT) GeV spectrum, which has a very hard photon index $\Gamma = 1.5$, and (b) is as shown in Chap. 2. Consequently, I concluded that the GeV–VHE γ-rays are of both hadronic origin and our observational results are evidence for cosmic ray acceleration close to the *knee* energy.

In Chap. 4, I estimated the detailed physical parameters of synchrotron X-rays (absorbing column $N_{\rm H}$(X-ray), photon index Γ, and absorption-corrected flux $F_{3-10{\rm keV}}$) using *Suzaku* archival datasets. Thanks to the low background level of the *Suzaku* XIS, I were able to determine the spatial distribution of the physical parameters at angular resolutions of $2'$–$8'$, which is comparable to the scale of the ISM distribution. The X-ray spectrum is dominated by a non-thermal component and can be fitted by a simple absorbed power-law model.

I determined that absorbing column density $N_{\rm H}$(X-ray) varies from 0.4×10^{22} cm^{-2} to 1.4×10^{22} cm^{-2} within the SNR and exhibits the cavity-like structure of the interstellar material. The distributions of $N_{\rm H}$(X-ray) and visual extinction $A_{\rm V}$ show an excellent positive correlation (correlation coefficient $\sim$0.83). Intriguingly, the $N_{\rm H}$(X-ray) value in the southeastern rim also is consistent with the cold HI estimated in Sect. 3.2.3.3. I have also shown that the flux distribution is very similar to the *Suzaku* XIS count maps. To understand the relationship between the X-ray flux and interstellar gas density, I investigated their correlation, obtaining a correlation coefficient of $\sim$0.55, which is not a strong correlation but is significant as it represents a large number of samples ($\sim$300). The results quantitatively support a strong connection between the X-rays and interstellar gas.

Next, I produced a photon index Γ map, which also varies from 2.1 to 2.9 within the SNR and has six prominent dips (low Γ value positions) located not only in gas rich regions in the west but also in gas poor regions in the east. To understand the spatial variation of the X-ray photon index (=acceleration efficiency of cosmic ray electrons), I compared it with the interstellar gas distribution and concluded that the photon index varies for two reasons. First, it is probable that the gas rich part of the SNR in the west of the shock–cloud interaction is dominated by turbulent excitation

($\eta \sim 1$), leading to a large rolloff energy and a small photon index. On the other hand, in the gas poor region in the east, the shock speed $v_{\rm sh}$ is not significantly decreased due to lower density. The photon index is inversely proportional to the rolloff energy of the X-rays and directly proportional to the shock speed $v_{\rm sh}$ and η^{-1}. Therefore, regardless of whether the gas is rich or poor, cosmic ray electrons can be accelerated efficiently through different mechanisms. Interestingly, the photon index becomes small toward some of the dense clumps. In the shock–cloud interaction scheme, the magnetic field is amplified in the interacting region, leading to higher synchrotron loss and a smaller rolloff energy. This can lead to lower X-ray intensity and rolloff energy toward the dense clumps, although I will obviously need to conduct more elaborate research to quantitatively confirm this. I therefore propose an additional acceleration mechanism such as the second-order Fermi acceleration (Fermi 1949) and/or magnetic reconnection (Hoshino 2012).

The results in this dissertation are summarized concisely as follows:

- For the first time, I obtained evidence for the acceleration of cosmic ray protons close to the *knee* energy in the young SNR RX J1713.7−3946.
- I quantitatively demonstrated a strong connection between the SNR shock waves, interstellar gas, and efficient acceleration of cosmic rays in the SNR.

Finally, I conclude that *the interstellar gas plays an essential role in producing γ- and X-rays and in efficiently accelerating cosmic rays in SNR RX J1713.7 -3946 and likely in other young γ-ray SNRs.*

5.2 Future Prospects

This study demonstrated the importance of shock–cloud interaction in understanding efficient cosmic ray acceleration in the young SNR RX J1713.7−3946. Our methods represent a revolutionary approach that has opened new possibilities in the field of astrophysics. However, our evidence is not sufficient to determine the universality of these mechanisms in Galactic and/or extra-Galactic SNRs. Additionally, I need to further reinforce and deepen our studies in order to achieve a better understanding of the phenomena of the universe. In this section, I present some of the future work or ongoing studies.

5.2.1 Further Expansion Our Studies into Analysis of Other SNRs

The target of the present study was limited to SNR RX J1713.7−3946 alone. It would be advantageous to expand our study to other SNRs using the methods described here in order to investigate the universality of our hypotheses. It would be useful to investigate whether the cosmic ray acceleration and the γ-ray production mechanisms

discussed here are applicable to other SNRs having a large range of physical parameters (e.g., SNR age, radius, interacting interstellar gas, and photon index of X-rays) to develop a better understanding of the evolution of SNRs and a unified view of the origin of VHE cosmic rays.

The goals outlined above can be divided into three categories:

[Category I.] Young SNRs

(e.g., Vela Jr., RCW 86, HESS J1731−347, SN1006, Cas A, and Tycho)

[Category II.] Middle-aged SNRs

(e.g., Puppis A, W28,W44, W51C, IC443, and W41)

[Category III.] Magellanic SNRs

(e.g., N132D, N23,N49, N157B, and N186D)

Young SNRs are the most important targets for this research because they emit high-energy X-rays and γ-rays and hence are actively accelerating cosmic rays to close to the *knee* energy. In particular, Vela Jr. (RX J0852.0−4622) is the best target of study because this SNR has the same characteristics (bright in VHE γ-rays and synchrotron X-rays) as RX J1713.7−3946. I have already begun comparative studies between high-energy radiation and interstellar gas, demonstrating that Vela Jr. has conditions similar to RX J1713.7−3946, namely, VHE γ-rays correspond well with the interstellar gas in terms of distribution and a hadronic origin is suggested (Fukui 2013). In addition, I are now observing Vela Jr. using *Suzaku* (AO8: PI H. SANO) and will demonstrate efficient acceleration of cosmic ray electrons through a detailed spectral analysis of the X-ray data. Our NANTEN team is currently studying other SNRs (e.g., HESS J1731−347, Fukuda et al. 2014; Cas A, CO observations with Nobeyama 45-m telescope (PI: H. SANO); SN1006, HI observations with ATCA (PI: T. FUKUDA); RCW 86, CO observation with Mopra (PI: Y. FUKUI)).

Middle-aged SNRs are also essential targets for understanding the advanced stage of shock interaction. In this case, non-thermal X-rays have already disappeared owing to cooling by means of high energy radiation (see Sect. 1.4).[1] On the other hand, GeV–VHE γ-rays are still bright in the neighborhood of such SNRs owing to the long cooling time scale (see Eq. 1.45) and are predicted to be converted to lower energy photons over time owing to the escape of cosmic rays (e.g., Gabici et al. 2009; Ohira et al. 2010). Moreover, shock waves will eventually slow down and heat up the surrounding interstellar gas, causing the emission of strong thermal X-rays.

[1] Most recently, however, non-thermal X-rays have been detected in middle-aged SNR W44 (Uchida et al. 2012). The authors also found that hard X-rays are enhanced around CO clumps in a manner similar to that discussed in this work. As such, relativistic cosmic ray electrons are probably being accelerated in middle-aged SNRs.

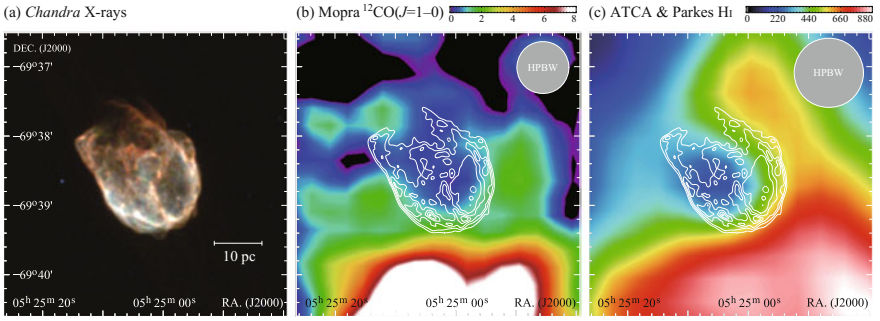

Fig. 5.1 (a) The *Chandra* three color image of SNR N132D. *Red*, *green*, and *blue* correspond to 0.5–1.2, 1.2–2.0, and 2.0–7.0 keV intensity distributions, respectively. (b) Integrated intensity map of the Mopra ^{12}CO(J = 1–0) data in a velocity range of $V_{\rm LSR}$ = 257.0–269.7 km s^{-1} is shown in color. The color scale indicates integrated intensity on a square-root scale in unit of K km s^{-1}. The *white* contours indicate the X-ray intensity in (**a**). The lowest contour level and intervals are 6.50 $\times$ 10^{-7} and 2.89 $\times$ 10^{-7} counts s^{-1} pixel^{-1}, respectively. (**c**) Integrated intensity map of ATCA & Parkes HI. The velocity range and contours are same as those in (**b**). The color scale also indicates integrated intensity on a liner scale and its unit is same as that in (**a**).

By analyzing these processes, I will be able to understand the physical conditions of shocked/ionized gas and escaped cosmic rays over a longer slice of time after the primary interaction. I have already started a comparison between GeV γ-rays and the interstellar gas distribution in middle-aged SNRs (see Sect. 1.5.1 and Yoshiike et al. 2013).

It is not easy to identify exactly where the interstellar gas interacts with SNRs because the resulting CO/HI clumps overlap in the line of sight, particularly toward the Galactic plane. On the other hand, the positions of SNR–interstellar-gas interaction in an external galaxy with a face-on orientation can be easily separated and are free from visual contamination. In this case, SNRs located in the Magellanic clouds, i.e., the "Large Magellanic Cloud" and the "Small Magellanic Cloud," are most suitable for such studies. Recently, I discovered a molecular cloud associated with SNR N132D in the Large Magellanic Cloud (see Fig. 5.1 in Sano et al. 2015). The detailed physical properties of this region will be revealed by observations using the Atacama Large Millimeter/submillimeter Array (ALMA).

The planned Cherenkov Telescope Array (CTA) will image $\sim$1000 VHE γ-ray SNRs with a ten-fold sensitivity relative to current Cherenkov telescopes (e.g., H.E.S.S., MAGIC, and VERITAS). Based on CTA observations, it will be possible to compare the spectral indexes of γ-rays will be able to compared with the interstellar gas and that of X-rays directory with the same spatial resolution, which will doubtlessly provide decisive evidence for the acceleration of cosmic ray protons.

5.2.2 *Resolving the Small-Scale Structure of SNR RX J1713.7−3946*

According to our numerical simulations, the molecular clumps that enhance the turbulence and amplify the magnetic fields through the shock–cloud interaction have smaller sizes than the currently identified CO clumps ($\sim$ 1 pc) in RX J1713.7−3946 by a factor of $\sim$3 (Inoue et al. 2009, 2012). The authors have pointed out the existence of small-scale structures in interstellar gas ($\sim$ 0.3 pc) that create $\sim$ 1 mG spots at a $\sim$0.05 pc scale. This is supported by X-ray observations (e.g., Uchiyama et al. 2007) that have shown an annual-scale flux variation of X-ray filaments ($\sim$ 0.05 pc) owing to strong synchrotron cooling, and it is consistent with magnetic field amplification around the small ($\sim$0.1 pc) gas clumps. Correspondingly, I are now observing the small scale structure of CO in SNR RX J1713.7−3946 using the Mopra radio telescope. These observations will detect CO clumps at a $\sim$0.2 pc angular resolution and will allow direct comparison between the results of numerical simulations and the actual CO structure parameters.

5.2.3 *More Detailed Analyses from a Viewpoint of Numerical Simulations*

In addition to the future prospect identified in (1), I should reanalyze the results of numerical simulations (Inoue et al. 2009, 2012). Specifically, it is necessary to derive physical parameters through numerical simulation that are directly comparable to CO observables (e.g., line width, intensity, and velocity fields) in order to investigate the detailed physics of shocked regions. Furthermore, I need to develop advanced simulations with more realistic initial conditions.

5.2.4 *Shock Speed Measurement Toward Southeastern Rim of RX J1713.7−3946*

In the discussion of Chap. 4, I noted that the shock speed in the eastern region of SNR RX J1713.7−3946 is faster than that in the western region. The measurement of shock speed is an important parameter in our model, as described Sect. 4.3.2.2. The western shock speed $v_{\mathrm{sh,west}}$ was estimated by a previous study (e.g., Uchiyama et al. 2007, and by private communications with Prof. Yasunobu Uchiyama), $v_{\mathrm{sh,west}}$ $\sim$3,000–4, 000 km s^{-1}. In addition, the southeastern rim of the SNR has two clear filaments that had been observed in 2005 by *Chandra*. Therefore, the shock speed of the southeastern rim $v_{\mathrm{sh,southeast}}$ can be obtained by additional *Chandra* observation, and the proper motion of the filament can be measured. For example, if $v_{\mathrm{sh,southeast}}$ $\sim$6,000 km s^{-1},

the filaments would have moved to the southeast by $\sim 10''$ ($\sim$0.05 pc) by 2014, which is detectable using *Chandra*'s high spatial resolution.

5.2.5 Search for Thermal X-Rays in Synchrotron Dominant SNRs

The thermal X-ray emission pattern provides much physical information, including electron temperature, ionization parameters, and ion temperature. These parameters are the essential physical quantities needed to understand the thermal balance between shock heating and cosmic ray acceleration.[2] In sites of efficient cosmic ray acceleration, such as RX J1713.7−3946, shock heating will suppress thermal emission caused by the huge dynamical pressure of accelerated cosmic ray particles (e.g., Helder et al. 2009). RX J1713.7−3946, a candidate for the above case, is now accelerating cosmic rays efficiently but has not been examined in the thermal X-ray spectrum. There have been only two SNRs to date besides RX J1713.7−3946 that have been shown to produce such pure non-thermal X-ray emissions: Vela Jr. and HESS J1731−347. I will perform deep observations using *Suzaku* XIS of SNRs in order to detect thermal X-rays. Our proposal to examine RX J1713.7−3946 has been accepted and I will observe it soon using the *Suzaku* XIS with 100 ks exposure (AO8, PI: H. SANO). These observations will reveal the electron temperature and ionization parameters in RX J1713.7−3946 for the first time.

References

F. Aharonian, A.G. Akhperjanian, A.R. Bazer-Bachi, M. Beilicke, W. Benbow, D. Berge et al., Astron. Astrophys. **449**, 223 (2006)
E. Fermi, Physica. Rev. **75**, 1169 (1949)
Fukui, Y., *In Astrophysics and Space Science Proceedings*, ed. Diego F. Torres, O. Reimer. 2nd Session of the Sant Cugat Forum on astrophysics, vol 34 (Springer, Berlin, 2013), p. 249
T. Fukuda, S. Yoshiike, H. Sano, K. Torii, H. Yamamoto, F. Acero et al., Astrophys. J. **788**, 94 (2014)
S. Gabici, F.A. Aharonian, S. Casanova, Month. Notice. R. Astronom. Societ. **396**, 1629 (2009)
P.F. Goldsmith, D. Li, M. Krčo, Astrophys. J. **654**, 273 (2007)
E.A. Helder, J. Vink, C.G. Bassa, A. Bamba, J.A.M. Bleeker, S. Funk et al., Scienc. **325**, 719 (2009)
M. Hoshino, Physica. Rev. Lett. **108**, 135003 (2012)
T. Inoue, R. Yamazaki, S.-I. Inutsuka, Astrophys. J. **695**, 825 (2009)
T. Inoue, R. Yamazaki, S.-I. Inutsuka, Y. Fukui, Astrophys. J. **744**, 71 (2012)
Y. Ohira, K. Murase, R. Yamazaki, Astron. Astrophys. **513**, A17 (2010)

[2] I can derive the total energy of shock waves $E_{\rm shcok} = kT_{\rm e} = m_{\rm e} v_{\rm shcok}^2$, where $T_{\rm e}$ is the electron temperature, $m_{\rm e}$ is the electron mass, and $v_{\rm shcok}$ is the shock speed. Therefore, I can compare the shock heated energy $kT_{\rm e}$ with the total energy of shock waves $m_{\rm e} v_{\rm shcok}^2$ using two parameters: $v_{\rm shcok}$ and $T_{\rm e}$.

H. Sano, Y. Fukui, S. Yoshiike, T. Fukuda, K. Tachihara, S. Inutsuka et al., Revolut. Astron. ALMA Third Year **499**, 257 (2015)
H. Uchida, K. Koyama, H. Yamaguchi, M. Sawada, T. Ohnishi, T.G. Tsuru et al., Publ. Astrono. Soc. Jpn. **64**, 141 (2012)
Y. Uchiyama, F.A. Aharonian, T. Tanaka, T. Takahashi, Y. Maeda, Nat. **449**, 576 (2007)
S. Yoshiike, T. Fukuda, H. Sano, A. Ohama, N. Moribe, K. Torii et al., Astrophys. J. **768**, 179 (2013)

Appendix A
Velocity Channel Distributions in RX J1713.7−3946

A.1 CO and Non-thermal X-Rays (J2000 Coordinate)

To clarify the relationship between X-rays and CO clumps in Chap. 4, it is necessary to identify all the CO clumps interacting with the SNR blast waves. Previous studies (e.g., Fukui et al. 2003) identified most of the CO clumps but did not do so completely because the velocity range was limited (e.g., $V_{\rm LSR}$: −12–−3 km s^{-1} in Moriguchi et al. 2005). We therefore identified all the CO clumps interacting with the SNR blast waves over a wide velocity range, such as in Chap. 2 ($V_{\rm LSR}$: −20–+2 km s^{-1}). We used the velocity channel maps and appropriate criteria to identify other CO clumps. Figure A.1 shows the velocity channel distribution of ^{12}CO(J = 1–0, 2–1) every 2 km s^{-1} from −24 km s^{-1} to 8 Km s^{-1} superposed on the *Suzaku* X-ray distribution (1–5 keV). We also plotted the position of each CO clump interacting with the SNR. The clumps, C$_{\rm E}$, D$_{\rm W}$, G$_{\rm E}$, O$_{\rm b}$, O$_{\rm SW}$, Q$_{\rm W}$, Z, Z$_{\rm NW}$ and Z$_{\rm NE}$, are newly identified in the present work.

A.2 CO, HI and VHE γ-Rays (Galactic Coordinate)

We show velocity channel distributions of ^{12}CO(J = 1–0, 2–1) and HI data for every 1 Km s^{-1} from −20 to 0 Km s^{-1} superposed on the VHE γ-ray distribution in Fig. A.2.

H. Sano, *Shock-Cloud Interaction in RX J1713.7–3946*,
Springer Theses, DOI 10.1007/978-4-431-55636-7

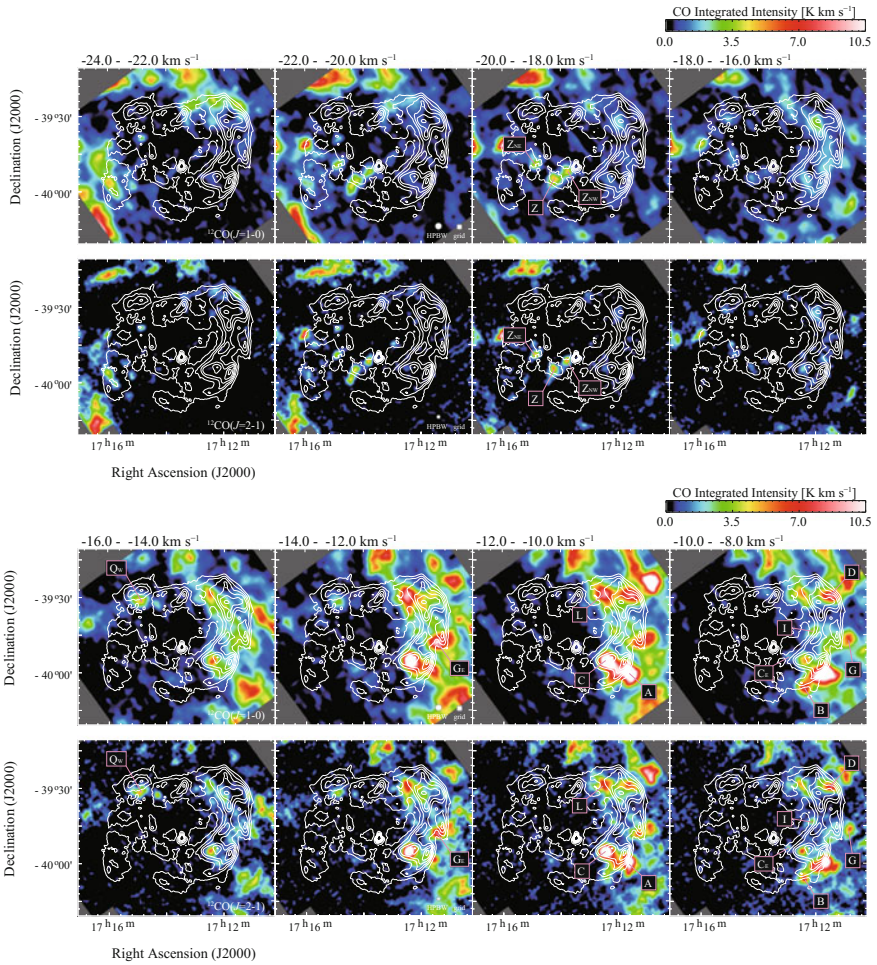

Fig. A.1 Velocity channel distributions of the ^{12}CO(J = 1–0) (*top panels* in false color) and ^{12}CO(J = 2–1) (*bottom panels* in false color) emissions overlaid on the *Suzaku* X-ray contours for the 1–5 keV energy band. Each panel of CO shows intensity distributions integrated every 2 Km s^{-1} in a velocity range from −24 to 8 Km s^{-1} following the color code shown on the *upper right*. In the X-ray distribution, the *lowest* contour level and the contour interval are 2.1 and 0.6 × 10^{-4} counts s^{-1} pixel^{-1}, respectively. CO clumps shown in Table 2.3 are also plotted

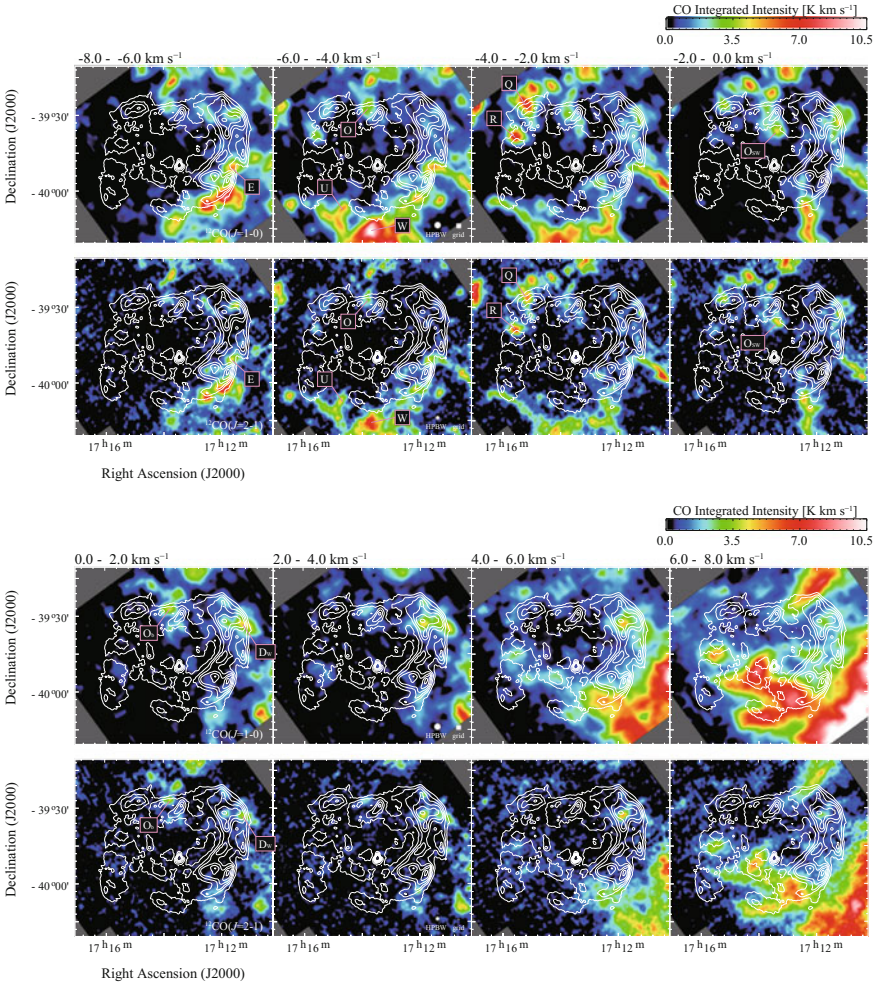

Fig. A.1 (continued)

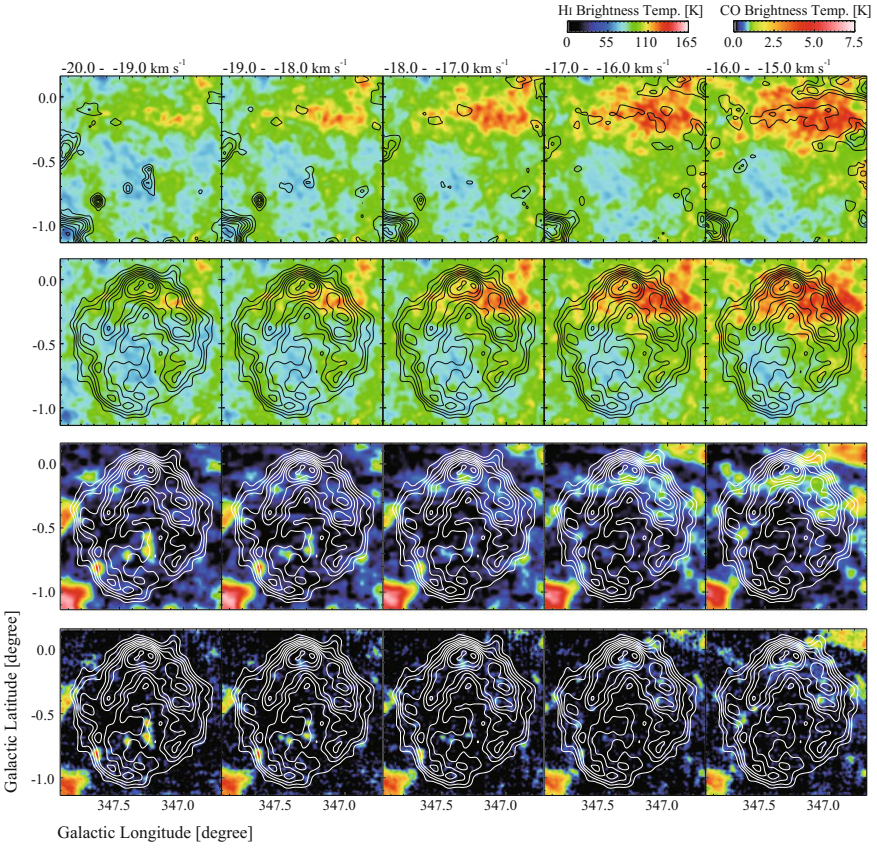

Fig. A.2 Velocity channel maps of ^{12}CO($J = 1$–0, 2–1) line emission and HI brightness temperature overlaid on the VHE γ-ray distribution. First-row panels (*top*): HI image and ^{12}CO($J = 1$–0) contours. Second-row panels: HI image superposed on the VHE γ-ray contours. Third-row panels: ^{12}CO($J = 1$–0) image superposed on the VHE γ-ray contours. Fourth-row panels: ^{12}CO($J = 2$–1) image superposed on the VHE γ-ray contours. Each panel shows CO and HI distributions every 1 Km s^{-1} in a velocity range from -20 to 0 Km s^{-1}. The lowest contour levels of CO and VHE γ-rays are 0.73 K ($\sim 3\sigma$) and 20 smoothed counts, and contour intervals of CO and VHE γ-rays are 0.73 K ($\sim 3\sigma$) and 10 smoothed counts, respectively

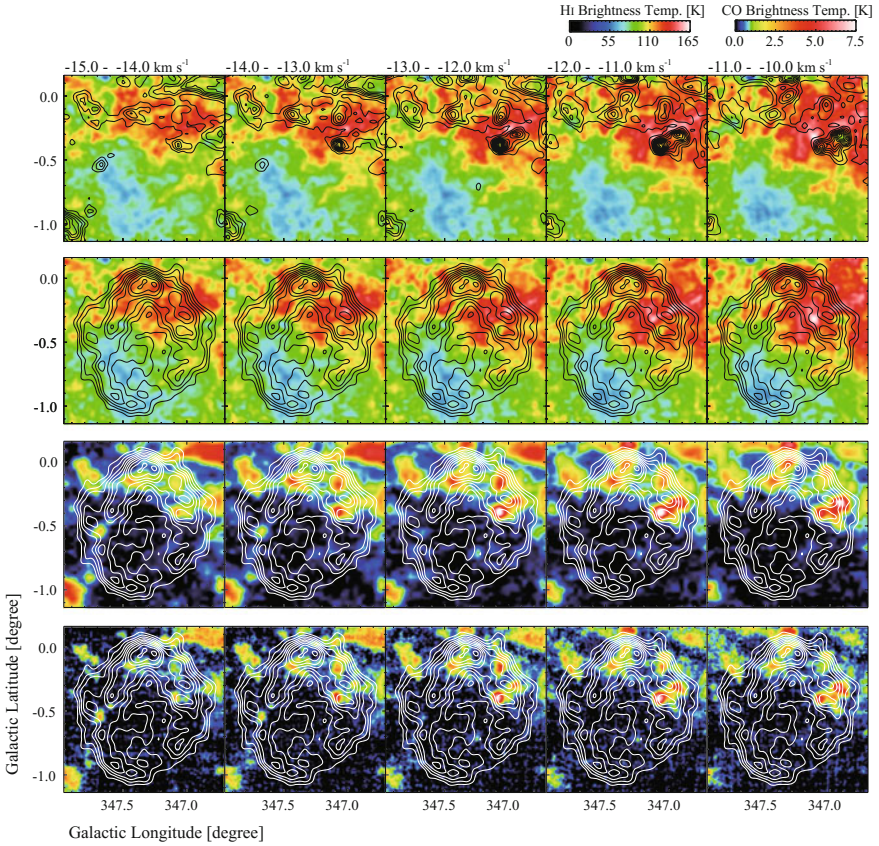

Fig. A.2 (continued)

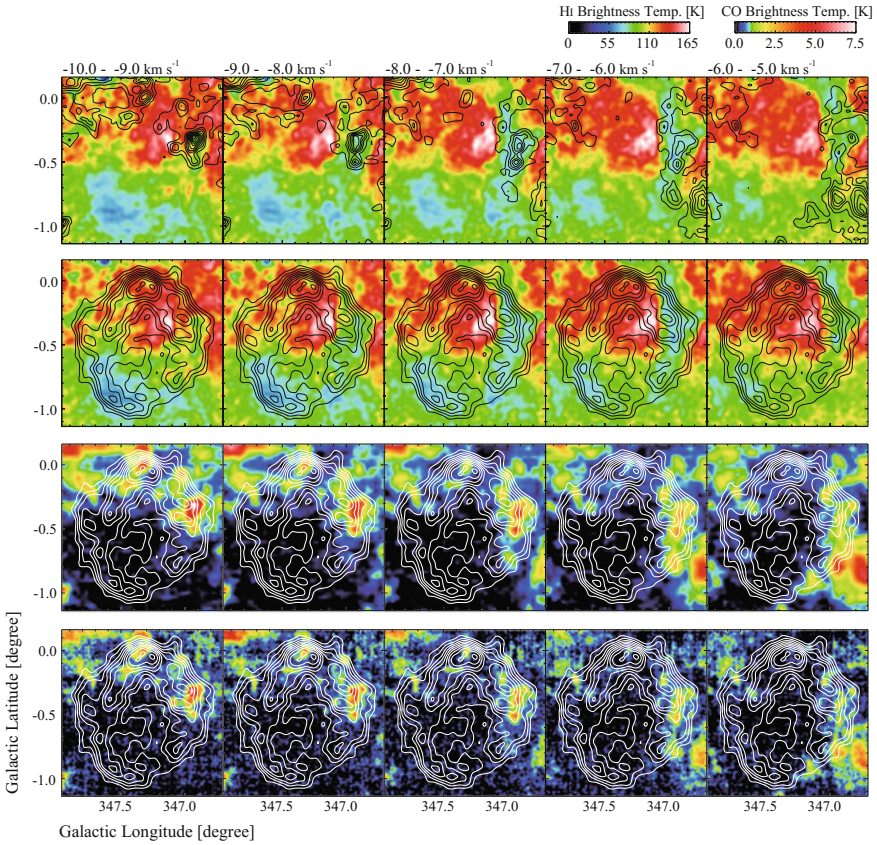

Fig. A.2 (continued)

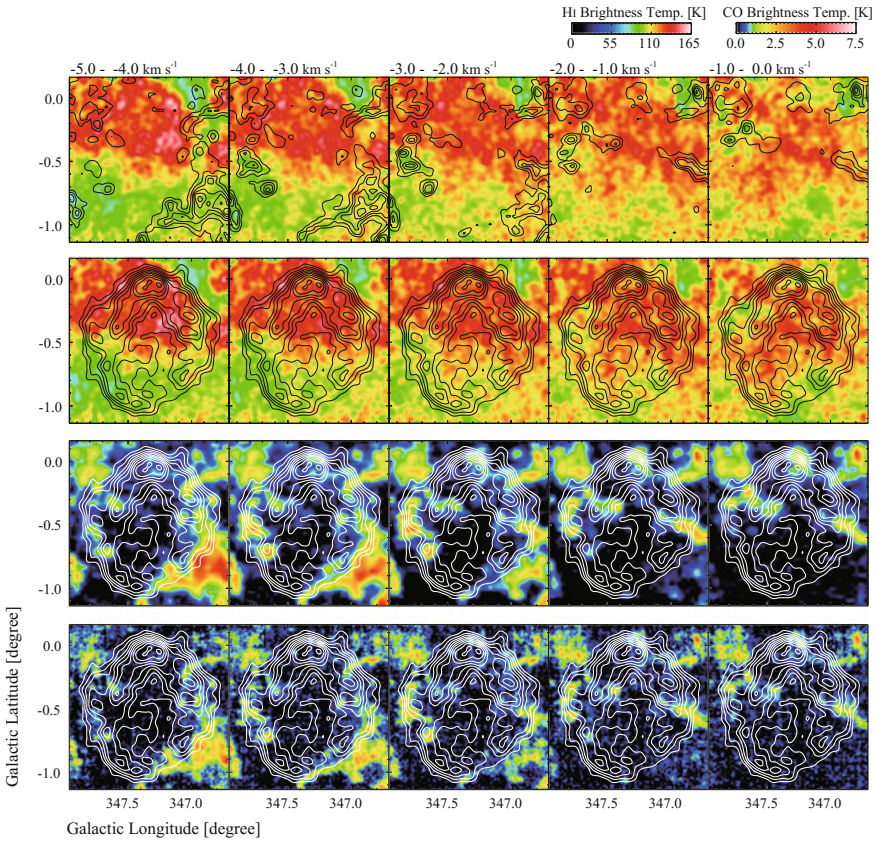

Fig. A.2 (continued)

References

Y. Fukui, Y. Moriguchi, K. Tamura, H. Yamamoto, Y. Tawara, N. Mizuno et al., Publ. Astron. Soc. Jpn. **55**, L61 (2003)

Y. Moriguchi, K. Tamura, Y. Tawara H. Sasago, K. Yamaoka, T. Onishi et al., Astrophys. J. **631**, 947 (2005)

Appendix B
Expanding Motion of the Dark HI SE Cloud

The left-hand side image of Fig. B.1 schematically shows an expanding spherical shell of radius $R_0 = 9$ pc and uniform expansion velocity $V_0 = 10\,\mathrm{km\ s^{-1}}$, and the right-hand side image of Fig. B.1 is a position–velocity diagram of the shell, where the ellipsoidal nature of the shell is not considered for simplicity.

Figure B.2 shows three representative velocity channel distributions of the dark HI SE cloud for a velocity range from -20 to -10 km s^{-1} and shows that the SE cloud is extended to the north. The extension shifts toward the northwest with velocity decrease from -10 to -20 km s^{-1}, as is consistent with the iso-velocity contours expected from the shell model in Fig. B.1.

Figure B.3 provides another presentation of the kinematical details of the SE cloud in the position–velocity diagrams. We choose a line AB passing through the center of the SNR and the SE cloud and another line CD passing through the SE cloud in the north–south direction (Fig. B.3a). We show a position-velocity distribution of HI along line AB (Fig. B.3b) and HI profiles along the two lines AB and CD (Fig. B.3c).

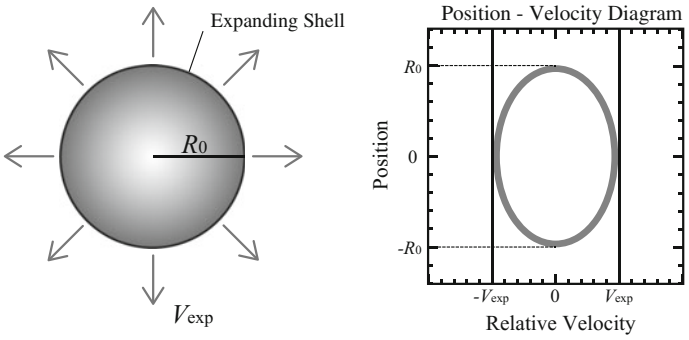

Fig. B.1 Schematic of a uniformly expanding shell and its velocity distribution in the position–velocity plane. Here, we assume a shell radius R_0 and an expansion velocity V_{exp} of 9 pc and 10 Km s^{-1}, respectively

H. Sano, *Shock-Cloud Interaction in RX J1713.7–3946*,
Springer Theses, DOI 10.1007/978-4-431-55636-7

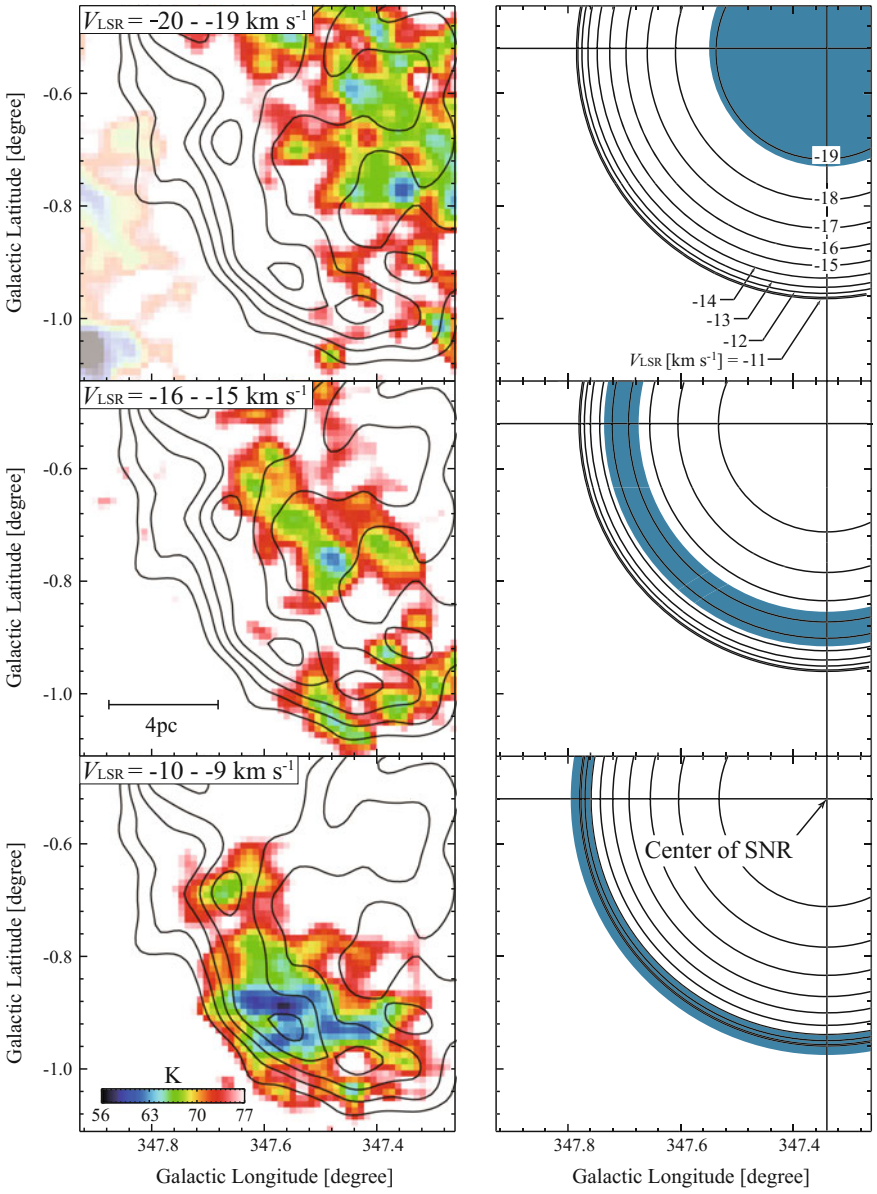

Fig. B.2 *Left* velocity channel distributions of HI integrated intensity toward the SE cloud superposed on the VHE γ-ray contours. VHE γ-ray contours are plotted every 10 smoothed counts from 20 smoothed counts. The faded area in the upper panel is a component unrelated to the SNR. *Right* model velocity distributions of the expanding shell shown in Fig. B.1. Iso-velocity lines are shown here, and blue areas show the corresponding velocity range shown in the left panels

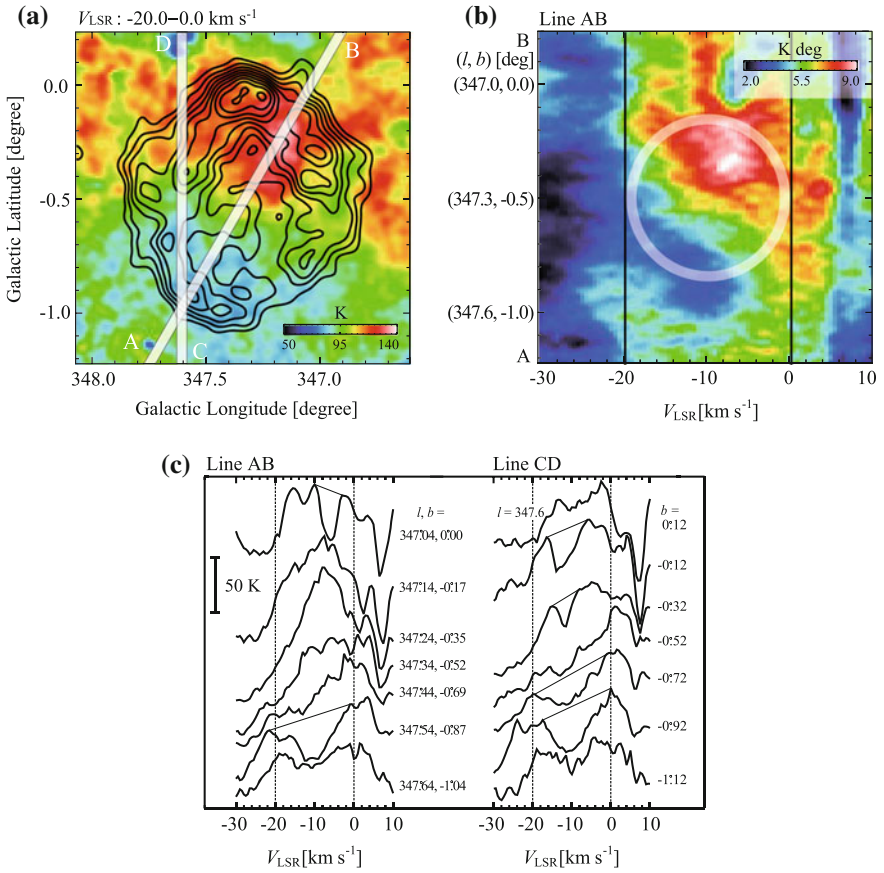

Fig. B.3 **a** Averaged brightness temperature distribution of HI in a velocity range from −20 km s^{-1} to 0 Km s^{-1}. Contours show the H.E.S.S. VHE γ-rays and are plotted every 10 smoothed counts from 10 smoothed counts. *Line* AB is inclined by 60° to the Galactic *plane* and *line* CD passes the center of the SNR. **b** Position–velocity distribution of HI along line AB in (**a**). The velocity resolution is smoothed to 1 Km s^{-1} and the integration interval is 200″. The white circle shows a schematic image of an expanding spherical shell (Fig. B.1). **c** HI spectra along the lines AB and CD in Figure (**a**). Expected profiles of HI self-absorption are shown by straight lines in the spectra with significant HI dips

We find that the SE cloud is extended to the northwest with a large velocity gradient of 10 Km s^{-1} per 0°.5, or ∼1.2 km s^{-1} pc^{-1}. The HI profiles in Fig. B.3c show that the dips are deep and clear at b less than −0°.5 but become shallower above $b = -0°.5$. The shallower dips make it nontrivial to quantify the dips at b higher than −0°.5; we note that even when the dips are not clearly seen, the HI probably suffers from self-absorption to some extent, as suggested by the weaker HI brightness at −12 km s^{-1} toward $b = -0°.52$ than toward $b = -0°.35$ (line AB).

We note that the strong velocity gradient in Figs. B.2 and B.3 is consistent with the blue-shifted part of an expanding shell. The strong velocity gradient is interpreted in terms of the expanding shell, as depicted by a white circle in the position–velocity diagram (Fig. B.3b). The blue shift by 10 km s^{-1} toward the center of the SNR indicates that this part of the shell is in the foreground. This is consistent with the dips being caused by self-absorption against the background HI emission. We also infer that the swept-up shell is highly non-uniform since the broad HI dips are seen in only a quarter of the shell.

Appendix C
Analysis of the HI Emission; The Optically Thin Case

The present analysis shows that the HI is self-absorbed in a part of the SNR, as indicated by the HI dips, and the HI column density is estimated considering this self-absorption (Fig. 3.7). To see the effects of self-absorption quantitatively, we here show for comparison the ISM proton distribution in the optically thin case, which does not consider self-absorption. Figure C.1, equivalent to the self-absorption case in Fig. 3.7, includes the HI column density distribution for the optically thin assumption smoothed to the H.E.S.S. resolution (Fig. C.1b, c), where the SE cloud is not seen. Figure C.1a–d are the same with those in Fig. 3.7. Figure C.2 is equivalent to Fig. 3.8. Figure C.2a is the total ISM proton column density for the optically thin HI at NANTEN resolution overlaid on the VHE γ-ray distribution. Figure C.2b is the corresponding azimuthal distribution of ISM protons and VHE γ-rays, where the ISM protons are deficient in the azimuthal angle from -90° to 0° as compared with those of Fig. 3.8b. Figure C.3 is equivalent to Fig. 3.10 and shows the radial distribution of ISM protons for the optically thin HI without correction for HI self-absorption. In the smoothed radial distribution, the effect of self-absorption is not as obvious.

H. Sano, *Shock-Cloud Interaction in RX J1713.7–3946*,
Springer Theses, DOI 10.1007/978-4-431-55636-7

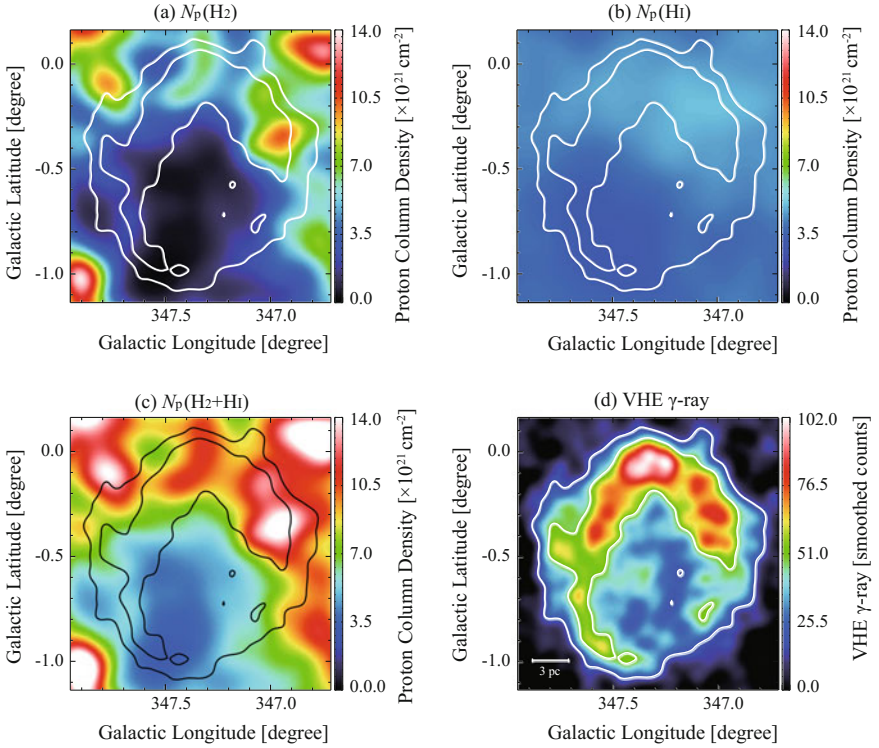

Fig. C.1 **a** Distributions of column density of the ISM protons N_p estimated from $^{12}CO(J = 1-0)$ $N_p(H_2)$, **b** HI emission without correction for the self-absorption $N_p(HI)$, and **c** sum of $N_p(H_2)$ and $N_p(HI)$. Here, we assume for reference that the HI emission is optically thin and the HI self-absorption is not considered. All datasets used here are smoothed to an HPBW of the VHE γ-ray distribution using a Gaussian function. **d** VHE γ-ray distribution. Contours are plotted every 50 smoothed counts from 20 smoothed counts

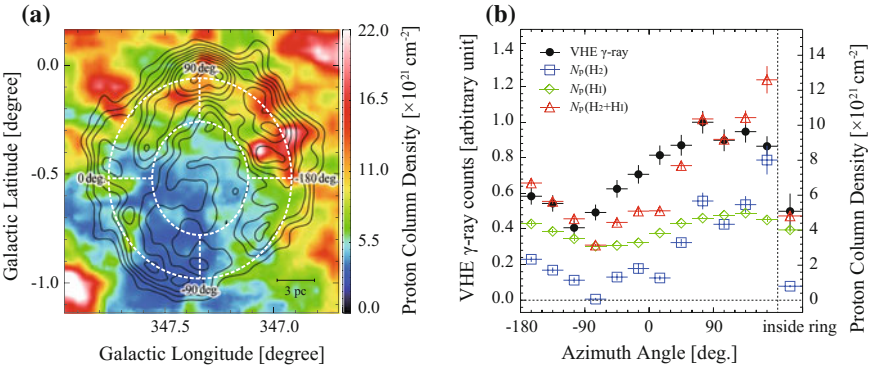

Fig. C.2 **a** Distribution of column density of ISM protons $N_p(H_2+HI)$ in a velocity range from -20 km s^{-1} to 0 Km s^{-1}, where the HI is assumed to be optically thin and without self-absorption. Contours and two elliptical rings are the same as those in Fig. 3.8a. **b** Azimuthal distributions of $N_p(H_2)$, $N_p(HI)$, $N_p(H_2+HI)$, and VHE γ-ray smoothed counts per beam in the two elliptical rings in (**a**). The same plots of the inside of the inner ring are shown on the *right side* in (**b**)

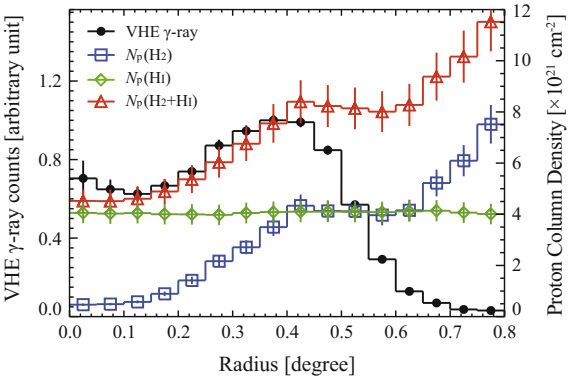

Fig. C.3 Radial distributions of averaged values of VHE γ-rays, $N_p(H_2)$, $N_p(HI)$, and $N_p(H_2+HI)$, where the HI is assumed to be optically thin, as in Fig. C.1. $N_p(H_2)$ and $N_p(HI)$ show column densities estimated from $^{12}CO(J = 1 - 0)$ and HI, respectively, and $N_p(H_2+HI)$ shows the total ISM column density, the sum of $N_p(H_2)$ and $N_p(HI)$

Appendix D
The Background Level of X-Rays

To estimate the azimuthal distribution of the X-rays in Fig. 2.8, we estimated the background level of the X-rays in the 1–5 keV energy band inside the SNR. Figure D.1 shows two histograms of the X-rays. One is extracted from the entire observed area, as shown in Fig. 2.1, and the other is extracted from a typical inner part of the SNR. The latter is extracted from nine circles of 6′ diameter that include no significant X-ray peaks. The central circle is at $(\alpha_{J2000}, \delta_{J2000}) = (17^h\ 13^m\ 52.8^s, -39°\ 49'\ 12.0'')$ and the other eight have offsets $\pm 11'$ from the center in $\alpha_{J2000}/\delta_{J2000}$, as shown in Fig. D.1b. We assume that the peak of the histogram for the whole region ($\sim 1.16 \times 10^{-4}$ counts s^{-1} pixel) is the typical background level outside the SNR and that the primary peak of the histogram for the inner part ($\sim 3.86 \times 10^{-4}$ counts s^{-1} pixel) indicates the background level of the SNR interior. We used the excess counts from the background level as those of the individual X-ray features in deriving the azimuthal distribution in Fig. 2.8.

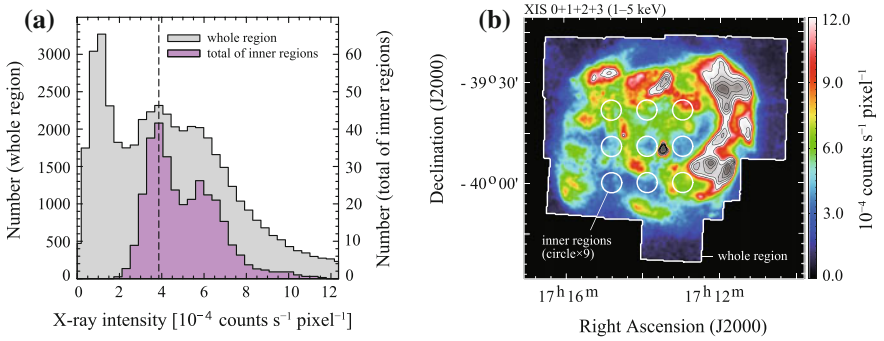

Fig. D.1 **a** Histograms of X-rays intensity in the 1–5 keV energy band. The gray and magenta histograms show the contributions of the whole observed region and of the typical inner region of the SNR, respectively. **b** Same XIS mosaic image (1–5 keV) as Fig. 2.2 (c). The region enclosed by the broken solid lines and that enclosed by the nine circles represent the whole and typical inner region used for (**a**), respectively

H. Sano, *Shock-Cloud Interaction in RX J1713.7–3946*,
Springer Theses, DOI 10.1007/978-4-431-55636-7

Appendix E
X-Ray Absorption by the ISM Affects the X-Ray Images

Here, we shall test whether the X-ray absorption by the ISM affects X-ray images. The X-ray counts in 1–5 keV are generally about 8 times higher than those in 5–10 keV, and the distributions in the two bands are fairly similar to each other (Figs. 2.5 and 2.7). The ratio of 8 is consistent with an X-ray photon index of ∼2.3 typical to the SNR (e.g., Tanaka et al. 2008). Only clump L shows the largest difference from 8 by a factor of more than two in the plot, indicating a softer spectrum. The similarity of the two bands suggests that X-ray absorption is not significant because the X-rays would show a much harder spectrum if it were. The optical depth owing to the ISM at X-rays is proportional to the (−8/3)-th power of the energy and is expressed as follows (Longair 1994);

$$\tau_{\rm x} = 2 \times 10^{-22} N_{\rm H}({\rm cm}^{-2}) \cdot \varepsilon^{-8/3}({\rm keV}), \tag{E.1}$$

where $N_{\rm H}$ (cm^{-2}) is the ISM column density and ε (keV) is the X-ray photon energy. The maximum ISM column density in the SNR is estimated to be 1×10^{22} cm^{-2} toward the brightest CO peak, clump C. Even for this column density absorption optical depths are 2, 0.3, 0.03, and 0.004 at 1, 2, 5, and 10 keV, respectively, as calculated by Eq. (E.1), and absorption is not likely to significantly affect the X-ray distribution. We tested the X-ray absorption toward clump C, where the X-rays show a depression that may possibly be caused by absorption. The X-ray intensity ratio toward clump C is ∼8.6 between the 1–5 and 5–10 keV bands, as observed by *Suzaku* (see Sect. 4.2.2). Using Xspec, we calculated the X-ray intensity integrated over the two energy bands for three different values of absorbing column density, i.e., 0.3, 1, and 3×10^{22} cm^{-2}, for an X-ray photon index of 2.3 and found that the intensity ratios between the two bands are ∼11.1, 7.0, and 3.5, respectively. A column density slightly less than 1×10^{22} cm^{-2} fits the X-ray observations reasonably well, as is consistent with the CO observations.

H. Sano, *Shock-Cloud Interaction in RX J1713.7–3946*,
Springer Theses, DOI 10.1007/978-4-431-55636-7

References

M.S. Longair, High Energy Astrophysics, vol. 2, 2nd edn. (Cambridge University Press, Cambridge, 1994)
T. Tanaka, Y. Uchiyama, F.A. Aharonian, T. Takahashi, A. Bamba, J.S. Hiraga et al., Astrophys. J. **685**, 988 (2008)